Applications of Theranostic Nanoparticles as Contrast Agents in Magnetic Resonance Imaging

Richard Aaron Revia

A dissertation
submitted in partial fulfillment of the
requirements for the degree of

Doctor of Philosophy

University of Washington

2020

Reading Committee:

Miqin Zhang, Chair

Fumio Ohuchi

Payman Arabshahi

Program Authorized to Offer Degree:
Materials Science and Engineering

University of Washington

Abstract

Applications of Theranostic Nanoparticles as Contrast Agents in Magnetic Resonance Imaging

Richard Aaron Revia

Chair of the Supervisory Committee:
Professor Miqin Zhang
Materials Science and Engineering

Advances in materials science that have allowed for the engineering of nanoscale structures represent a revolutionary paradigm shift for the detection and remediation of diseases such as cancer. Worldwide research efforts are currently leveraging the tools of nanotechnology to aid the fight against cancer by developing novel material architectures that are designed to provide quicker diagnoses of disease at earlier time points than are currently available and improved therapeutic responses by efficiently killing cancer tissue while minimizing off-target side effects. One nanotechnology in particular, iron oxide nanoparticles (NPs), has received intense interest due to its many beneficial attributes: biodegradability, chemical surface properties, and superparamagnetism. Unlike other metal-core NPs, iron oxide NPs are nontoxic when decomposed and prepared for excretion by the body as the iron in their cores may be used by the body in iron-containing proteins (e.g., hemoglobin and ferritin). Additionally, the chemical composition of iron oxide lends itself for use in chemical passivation techniques that seek to coat the iron oxide cores in polymers that confer advantageous qualities of biocompatibility and ligation of functional moieties. Finally, the magnetic properties of iron oxide particles of nanoscale proportions allow the NPs to serve as contrast enhancing agents in magnetic resonance imaging (MRI), a tool that is widely used to image the soft tissue of the body for cancer detection. This dissertation details the use of iron oxide NPs as contrast agents for MRI and as therapeutic agents targeting an insidiously aggressive brain cancer: glioblastoma. First, noninvasive MRI is used to determine the biodistribution of iron oxide

NPs in both mice and nonhuman primates in a first-of-its-kind, cross-species comparison of iron oxide NP pharmacokinetics. It was found that the pharmacokinetics of iron oxide NPs between the two species were similar in some organs (i.e., blood, liver, spleen, and muscle) but distinct in others (i.e., kidneys, brain, and bone marrow). Next, iron oxide NPs are directly delivered to brain tumors in mice via convection-enhanced delivery (CED), and their distribution throughout the tumor volume is tracked in real-time using MRI. The distribution of iron oxide NPs ligated with a glioblastoma-targeting peptide, chlorotoxin, is compared to the distribution of bare NPs; results show that NPs attached to chlorotoxin are better able to suffuse throughout the tumor volume than NPs lacking the tumor-targeting moiety. Following these research efforts that display the ability of iron oxide NPs to serve as contrast agents in MRI, a therapeutic example of iron oxide NPs in oncology is provided as these NPs are used to enhance the radiation dose delivered to mice-bearing orthotopic glioblastoma tumors. Mice treated with NPs prior to receiving radiotherapy exhibited a 2-fold increase in median survival compared to mice receiving only radiotherapy. Finally, a novel nanotechnology platform, boron-doped graphene quantum dots, is explored for use as a nontoxic MRI contrast agents.

TABLE OF CONTENTS

LIST OF FIGURES

LIST OF TABLES

ACKNOWLEDGMENTS

I have been extremely fortunate to have been able to study and perform research at the University of Washington. During my doctoral education, I have developed as a researcher and as a person, and that growth has been catalyzed by many outstanding individuals I have been blessed to know. First and foremost of those individuals is my advisor Professor Miqin Zhang, whose guidance, direction, and leadership have helped me to learn what it means to be an independent investigator.

The work presented in thesis (and even more research I have accomplished that is unable to fit inside this dissertation) would not have been possible without the help of many colleagues and collaborators. I would like to express my sincere gratitude to the many members of the Zhang lab group who have assisted me with research, laughed with me in the lab, and made the long, hard days seem short: Dr. Zachary R. Stephen, Professor Peter A. Chiarelli, Dr. Kui Wang, Dr. Sheeny Lan Levengood, Professor Forrest M. Kievit, Olivia Chang, Dr. Ariane Erickson, Steve Chung, Dr. Mike Jeon, Guanyou Lin, Charles Yen, Professor Hui Wang, Dr. Qingxin Mu, Shawn Swanson, Brandon A. Wagner, Scott Mason, Chris Dayringer, Dr. Dennis Edmondson, and Dr. Dave Wood. I would also like to thank some of the many collaborators across the University that have helped me: Professor Richard G. Ellenbogen, Dr. Kenneth Marro, Professor Donghoon Lee, Dr. Eric Shankland, Professor Kevin E. Conley, Professor Eric Ford, Kevin Yagle, Professor John R. Silber, Dr. Scott Braswell, and Dan Shea. All of these people (and many more not listed) have made my time at the University of Washington precious.

Chapter 1

INTRODUCTION AND RATIONALE

Globally, cancer is a leading cause of death, second only to heart disease, and cancer is presently the leading cause of premature death in most countries.[1] Approximately 18.1 million cases of cancer were developed in 2018, and 9.6 million deaths worldwide were attributed to cancer in the same year; it is estimated that $\sim$12% of women and $\sim$10% of men will have cancer at some point in their lives.[2] The number of new worldwide cancer cases per year is predicted to grow from 18.1 million in 2018 to 27 million by the year 2040.[1] Given the prospect of continued growth in worldwide cancer diagnoses and deaths, coupled with the somewhat stagnant progress in developing novel cancer therapeutics, unconventional treatment techniques demand consideration in an effort to extend the lifespan and quality of life of patients battling oncological disease. The mainstays of cancer therapy currently consist of surgical resection, radiotherapy, and chemotherapy; these treatment methods suffer from limitations such as the unintentional removal or destruction of healthy tissue, use of potentially harmful and carcinogenic ionizing radiation or small molecule drugs, and deleterious side-effects caused by chemotherapeutics.

The emerging field of nanomedicine aims to address the many shortcomings of currently available clinical treatments for cancer. In an effort to improve therapeutic outcomes and diagnostic capabilities in the fight against cancer, nanoparticles (NPs) are being developed for tumor-targeted delivery of small molecule drugs to improve conventional chemotherapy, as carriers of nucleic acids in gene therapy, and as contrast enhancing agents for advanced diagnostic imaging procedures among many other potential avenues to improve the health outcomes of those suffering from cancer. One NP formulation in particular, iron oxide NPs, have distinct benefits afforded to them by their biocompatibility, biodegradability, ease of synthesis, and ability to be functionalized with

targeting epitopes, chemotherapeutics, and molecular imaging probes.

The research presented herein extends the development of iron oxide NPs and demonstrates their applications for use in magnetic resonance imaging and as potential enhancers of radiation therapy. Further, a novel use of graphene quantum dots as contrast agents in magnetic resonance imaging is also detailed. This dissertation is organized as follows:

Chapter 1 provides an introduction and rationale for this research.

Chapter 2 reviews the salient design principles associated with using iron oixde NPs for in vivo medical applications. Includes background information on the importance of NP size and the choice of polymer coating. A brief overview of the physics of magnetic resonance imaging and how iron oxide NPs can be used to enhance contrast is provided.

Chapter 3 demonstrates how the biodistribution of iron oxide NPs may be tracked using noninvasive magnetic resonance imaging with high spatiotemporal resolution. Using this full-body magnetic resonance technique, the first inter-species comparison study of NP biokinetics between mice and nonhuman primates is provided.

Chapter 4 presents another magnetic resonance imaging application of iron oxide NPs, where the volume of distribution of iron oxide NPs administered to mice bearing brain tumors via convection enhanced delivery is determined over time. A comparison of volume of distribution over time is evaluated between bare NP and NP conjugated to the tumor-targeting ligand chlorotoxin. Results show the ability of chlorotoxin to prolong the retention of NPs within brain tumors.

Chapter 5 extends the diagnostic applications of iron oxide NPs detailed in Chapters 3 and 4 to a therapeutic technique wherein the NPs are used to enhance radiotherapy in a murine model of glioblastoma. Mice recieving an injection of iron oxide NPs prior to applied radiotherapy benefit from improved survival outcomes compared to mice recieving radiothearpy only.

Chapter 6 presents another NP formulation, boron-doped graphene quantum dots and its application as a contrast agent for T1-weighted magnetic resonance imaging. Results indicated that boron-doped graphene quantum dots peform better than the clinical gold-standard T1 contrast agent while exhibted less toxicity.

Chapter 7 summarizes this research and imparts the main conclusions.

Chapter 2

KEY PHYSICOCHEMICAL PROPERTIES OF IRON OXIDE NANOPARTICLES FOR USE IN MEDICINE

The development of nanoparticles (NPs) for use in all facets of oncological disease detection and therapy has shown great promise over the past few decades. NPs have been tailored for use as contrast enhancing agents for medical imaging, as drug delivery vehicles to fight illnesses, and most recently as therapeutic components that potentiate tumor cell death in magnetic and photonic ablation therapies. Of the many possible core constituents of NPs, such as gold, silver, lipids, etc., iron oxide-based NPs have been extensively investigated due to their many favorable properties such as their superparamagnetism, biocompatibility, and biodegradability.

2.1 A Brief Overview of Iron Oxide Nanoparticles in Medicine

The development of nanoscale technologies has been widely touted as a revolutionary paradigm shift for the detection and remediation of cancer. Indeed, the surge in research efforts exploring the design and synthesis of NP systems has seen the creation of many material formulations exhibiting promising therapeutic and diagnostic (theranostic) effects towards the treatment of various cancer types in a single nanodrug.[3–5] NP configurations include those with fundamental cores of organic molecules (e.g., dendrimers, DNA, lipids, viruses, and micelles), inorganic molecules (e.g., iron oxide, gold, quantum dots, carbon nanotubes, and fullerenes), or a hybrid of two or more of these components.[6,7] Each base structure has associated advantages and disadvantages that depend on the application under consideration. Furthermore, these formulations have properties that are tunable to some degree, such as size, surface charge, and hydrophobicity, allowing them to be optimized for a desired function.

Iron oxide NPs with nanocrystalline magnetite (Fe_3O_4) cores have great potential for use in

oncological medicine due to their biocompatibility,[8] biodegradability,[9] facile synthesis,[10] and ease with which they may be tuned and functionalized for specific applications. Additionally, spherical magnetite NPs with diameters less than approximately 20 nm will exhibit superparamagnetic behavior, a property that is exploited to enhance contrast in magnetic resonance imaging (MRI).[11–13] Typically, superparamagnetic iron oxide NPs are comprised of a magnetite core providing inherent contrast for MRI and a biocompatible coating that provides ample functional groups for conjugation of additional tumor-targeting and therapeutic moieties. Some formulations of magnetite-based NPs have already gained approval for use in humans as iron deficiency therapeutics and as MRI contrast agents by the Food and Drug Administration (e.g., Feraheme®, Feridex I.V.®, and Gastromark®); consequently, extension of these NP configurations for clinical uses beyond MRI contrast enhancement such as cancer therapy via drug delivery, biotherapeutic transport, magnetic hyperthermia, photothermal ablation, and photodynamic therapy may be fast-tracked as compared to NP formulations lacking widespread acceptance of nontoxicity (e.g., other metal-core NPs).[13] This idea highlights the considerable capacity iron oxide NPs have for use in highly personalized medicine; as researchers develop a library of synthesis protocols and discrete nanoscale modules with specific roles for cancer theranostics, individualized NP formulations exhibiting a full-suite of treatment and diagnostic capabilities may be created in an efficient and effective manner. An exemplary iron oxide NP incorporating a multitude of diagnostic and therapeutic features is depicted in Figure 2.1.

Important design parameters for NP-based therapeutics are hydrodynamic size, particle size distribution (PSD), surface charge, drug-load capacity, and a surface chemistry that accommodates ligation of targeting agents and other functional moieties, which can influence immunogenicity, toxicity, pharmacokinetics, and biodistribution. They hydrodynamic size of NPs is critical because of the relationship between hydrodynamic size and biodistribution. If the hydrodynamic size is too large (> 100 nm), the NPs will quickly be recognized by the body as a foreign invader, removed from blood circulation, and sequestered to the liver and spleen by the reticuloendothelial system; if they are too small (< 100 nm) the NPs will not be retained in circulation for a significant period of time due to renal clearance.[7,14] Distinct from an NP's hydrodynamic size is the PSD,

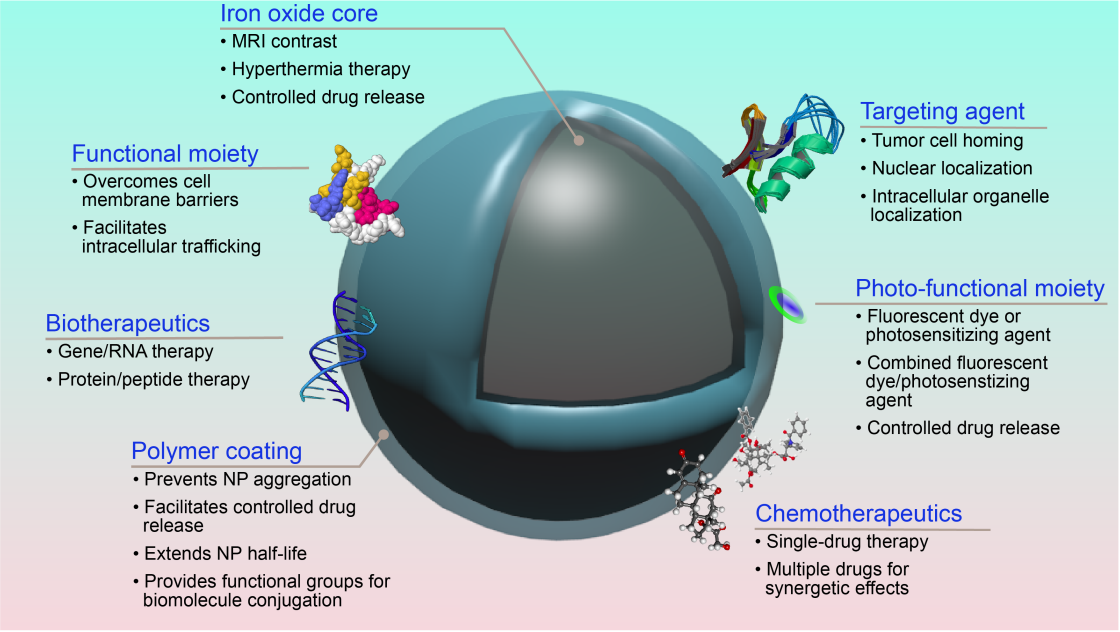

Figure 2.1: Schematic illustration of a full-suite theranostic NP. The magnetite core serves as an MRI contrast agent, and a polymer coating increases biocompatibility, mitigates uptake by the reticuloendothelial system, and allows for facile functionalization with chemotherapeutic, biotherapeutic, optical enhancement, and disease-targeting moieties.

which represents the prevalence of each possible hydrodynamic size within a sample of NPs. The overall hydrodynamic size of a sample of NPs is often quoted as the mean of the PSD. Thus, it is important to consider the PSD of drug delivery vehicles since the average hydrodynamic size of a sample of NPs may be less than 100 nm while the NP ensemble may contain a significant number of NPs with a hydrodynamic size greater than 100 nm. If these larger particles are introduced into a biological system, they may trigger an unwanted immune response. Furthermore, NPs with different hydrodynamic sizes will have different physiochemical properties (e.g., magnetic properties, biodistribution, drug loading capacity, etc.). A highly monodisperse sample of NPs will consist of individual particles with very similar properties, but a polydisperse or broadly distributed sample will have a wide variance in properties between individual NPs which could lead to variable functionality.

The hydrodynamic size of an iron oxide NP includes its inorganic interior along with any surface coating and the solvent layer that establishes in aqueous environments. Metal-core NPs tend to

aggregate in solution if they lack a surface coating; a scenario which presents a serious safety concern for in vivo use (e.g., the aggregation of NPs in the bloodstream could block blood flow). Thus, iron oxide NPs are generally coated with polymer to confer dispersion stability and increase blood circulation times. Poly(ethylene glycol) (PEG) and chitosan are examples of polymer coatings that increase the circulation half-life of NPs and afford biocompatibility (i.e., they aid the NP in avoiding the body's innate immune system). Copolymer coatings may also be employed to benefit from the combined advantages provided by the individual polymers used. For example, a chitosan-PEG copolymer capitalizes on chitosan's functional groups that facilitate ligation chemistry for attachment of functional moieties like targeting agents and on PEG's ability to provide steric hindrance resulting in improved colloidal stability and avoidance of an innate immune response.[15]

Well-chosen polymer coatings will not only confer biocompatibility onto the NP but they will facilitate the attachment of molecules (e.g., peptides) that will allow the NPs to home to specific types of cells within the body or help the NPs to cross specific biological barriers like the blood-brain barrier. With respect to cancer therapy, the method of NP accumulation at tumor sites is typically categorized into two classes: passive and active targeting. Passive targeting relies on the enhanced permeability and retention effect.[16] Passive targeting is limited however because not all tumors exhibit the enhanced permeability and retention effect and the degree of permeability of the tumor vasculature is unlikely to be homogeneous across the whole site.[17] Attempts at overcoming these limitations are made with active targeting. Active targeting is achieved by modifying an NP through the attachment of a targeting ligand to the NP surface. Ligands that recognize biological structures unique to or overexpressed in cancer cells can then preferentially accumulate at tumor sites. A third mode of targeting unique to magnetic NPs such as iron oxide is the use of an external magnetic field to draw the NPs to the site of action.[18]

Recently, it was shown that titanium dioxide and iron oxide NPs, as well as other NP formulations, induce gaps tens of microns in size between endothelial cells (i.e., cells that form the interior walls of blood vessels).[19,20] The mechanism by which NPs cause such openings was dubbed nanoparticle-induced endothelial leakiness (NanoEL).[21] Prior to the discovery of NanoEL, the routes for NPs to escape the endothelium were thought to be confined to typical transcellu-

lar endocytosis and diffusional transport through cell membranes via cell-cell junctions; however, these methods of NP transport through the endothelium alone are not sufficient to explain the speed with which NPs have been shown to enter certain highly vascularized organs like the kidneys, liver, and spleen.[21] NanoEL occurs much more rapidly than either endocytosis or diffusion through cell-cell junctions. The phenomenon of NanoEL is described by the intracellular binding of NPs to VE-cadherin; following this pairing, phosphorylation of VE-cadherin is triggered which in turn results in a rearrangement of the endothelial cell cytoskeleton.[22] This insight into the interaction of NPs with biological environments is of paramount importance as it may provide an explanation for the physical mechanism by which off-target accumulation of NPs at sites other than tumors happens. Further exploration into how specific NP characteristics like size and surface charge alter the behavior of the NanoEL effect may help nanotechnologists to mitigate off-target NP accumulation and even exploit induced endothelial leakiness for therapeutic effects.

2.2 Relevant MRI Background Information for Imaging Iron Oxide Nanoparticles

Imaging tumorous tissue is crucial in the diagnosis and treatment monitoring of cancer.[23,24] Clear depictions of tumor boundaries allow for accurate judgments of tumor distribution and its response to surgical removal and adjuvant therapies. Many imaging modalities are employed for early detection and interrogation of cancer, including X-ray, ultrasound, MRI, computed tomography, and positron-emission tomography.[23] Iron oxide NPs have been extensively researched for their use in augmenting contrast for MRI.[25] MRI provides exquisite detail of the soft tissues, has unlimited penetration depth, and is considered a noninvasive imaging technique since it uses nonionizing radiation. For these reasons, MRI is a commonly used tool that aids physicians in medical diagnosis.

MRI, and its progenitor nuclear magnetic resonance, relies on the fact that protons have an intrinsic property called spin. Associated with this spin is an angular momentum. It is important to keep in mind that spin and its associated angular momentum are quantum mechanical properties without much relation to the spin of terrestrial objects we are familiar with; the angular momentum of a proton or neutron never speeds up or slows down (like a child's spinning top would), but the direction of the axis about which the spin revolves can change. In addition to angular momentum,

the other important physical quality associated with the spin of a proton is that they generate a magnetic dipole moment. To provide a further description of what happens to a single proton during an MRI experiment would require an esoteric foray in quantum mechanics that likely would not elucidate the situation in any meaningful way. On the other hand, describing the behavior of a lone proton using classical mechanics would be inaccurate. However, a description of MRI physics that is both accurate and informative may be based on a classical mechanics view of a bulk ensemble of protons. That is, classical physics cannot describe the behavior of a single proton, but it can provide a description of the average behavior of many proton spins.

When protons are placed in a strong external magnetic field, B_0, their magnetic dipole moments tend to align with the external field. However, because protons have angular momentum, this net alignment with B_0 is not instantaneous, and the spin axis of the ensemble of protons will precess around the axis of the external field (Figure 2.2). Since the magnitude of the angular momentum associated with a proton is fixed and B_0 is static, the rate of precession will also be an unchanging value; this value is known as the precession frequency, f_0, and it is directly proportional to the magnitude of the external field B_0:

$$B_0 = \gamma f_0 \tag{2.1}$$

where γ is the gyromagnetic ratio. For protons (^{1}H), $\gamma = 42.58$ MHz T^{-1}.

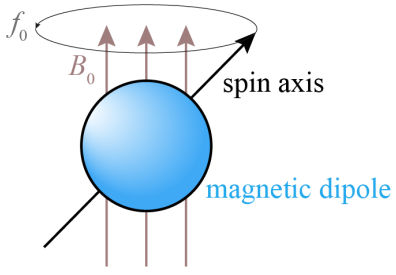

Figure 2.2: Precession of the net magnetization vector of an ensemble of protons. When many protons are placed in a static external magnetic field, B_0, the magnetic dipole moments of the individual protons tend to align in the direction of B_0 creating a net magnetization vector. However, because the protons have a constant magnitude of angular momentum, the net magnetization vector of the ensemble of protons will precess about the axis of B_0 with frequency f_0.

If we have a sample of water, with many protons in it, the net magnetic moment acquired by summing the magnetic moments of each individual proton for that sample will be zero because the magnetic moments of the protons in the sample will be randomly oriented leading to zero net magnetic moment. However, if we place that sample of water in a strong external magnetic field, B_0, as we do in an MRI experiment, over time, a net magnetic moment will arise in the sample of water as the protons in the sample align with the external magnetic field; the net magnetization vector describing the net magnetic moment of the aligned protons is called the equilibrium magnetization, M_0. Since M_0 is much smaller in magnitude and in the same direction as B_0, M_0 is not very useful because it cannot be measured (i.e., it is dwarfed by B_0).

However, if we could tip all the protons contributing to M_0 by 90°, we might be able to measure the new magnetization vector of all the tipped protons. If we apply a strong pulse at just the right frequency, we can force the net magnetic moment of our sample to tip over 90°. As soon as our pulse is removed, our protons will realign with B_0 in a process called relaxation. The frequency of the applied pulse must be f_0 of equation 2.1, or

$$f_0 = \frac{B_0}{\gamma} \tag{2.2}$$

In clinical MRI machines, B_0 is typically either 1.5 T or 3.0 T. At 3.0 T $f_0 = 128$ MHz. In fact, for the vast majority of commercial MRI machines, f_0 lies in the radio frequency (RF) range of the electromagnetic spectrum, and the coils inside MRI machines that generate the pulses that tip over the magnetic moments of the protons being imaged are called RF coils. This tipping of magnetic moments is a resonant phenomenon, where the resonant frequency is the frequency of precession, f_0, or the Larmor frequency.

The tipped protons continue to precess at the same frequency, f_0, but since the magnetization vector is 90° out of phase with B_0, the net magnetization vector becomes a measurable electromagnetic signal that will look like the signal shown in Figure 2.3. Note that in Figure 2.3, the y-axis is labeled M_{xy}; that is, Figure 2.3 depicts the measurement of the net magnetization vector of the protons being interrogated as measured in the xy-plane of 3-dimensional space, where the z-axis is taken to be parallel to the direction of B_0.

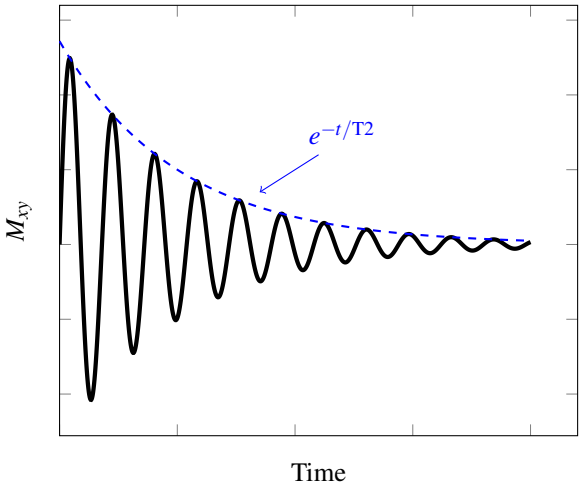

Figure 2.3: Free induction decay. Before time $t = 0$, protons in a sample are aligned in the z-direction along with an externally applied static magnetic field B_0. At time $t = 0$, an RF pulse is applied to the sample resulting in the tipping over of the net magnetization vector of the protons in the sample 90° into the xy-plane. Over time, the magnetization vector in the xy-plane decays to 0 as the net magnetization vector of the protons relaxes back into realignment with the external field, B_0, which points in the z-direction.

The xy-plane is called the transverse plane. The decay constant of the exponential decay of the net magnetization vector M_{xy} shown in Figure 2.3 is called T2. The reason the signal in the transverse plane decays to zero after the RF pulse is applied is because the protons in the sample do not precess at exactly the same frequency; each is slightly influenced by the magnetic field generated by other protons nearby. If those fields add to B_0, the precessional frequency increases, if they subtract from B_0 the frequency decreases (see equation 2.1). Soon, the magnetization vectors in the xy-plane add destructively to cancel each other out because all of the proton precessions get out of phase. Likewise, because tissues have different atomic chemical compositions, each tissue has a unique T2 value. This is how contrast arises in an MRI image, and an image created by assigning grayscale values to voxels (which are similar to pixels in 2-dimensions, but since MRI images are created by sampling the magnetic signal inside some 3-dimensional volume they are called voxels) based on the magnitude of the transverse magnetization vector measured some time after the RF pulse tipped over the magnetization vector that was aligned with B_0 into the xy-plane is called at T2-weighted (T2-W) image. Alternatively, instead of measuring M_{xy} at one time point

after applying an RF pulse, M_{xy} can be measured many times in an attempt to recreate the decay curve. From the decay curve, an estimation of the value of T2 can be made, and an image that is assigned grayscale values based on an estimation of T2 is known as a quantitative T2 (QT2) image. Note that T2-weighted images are not precisely quantitative; this is because the units of measurement when sampling M_{xy} in an MRI experiment are not known (they are "arbitrary units") because the instrument is usually not precisely calibrated to attach units of magnetic intensity to M_{xy}. On the other hand, units of milliseconds may be applied to measurements of the decay constant T2 from appropriately design MRI scan sequences because the instrument's temporal measurements are calibrated to known standards of time.

Just as the magnetization vector in the transverse plane may be measured, we may also measure the signal of the protons in the sample as they relax back into realignment with B_0. Such a signal is measured in the longitudinal plane, M_z, and would appear as the signal shown in Figure. Corollaries to generating T2-W and QT2 images apply to generating T1-weighted (T1-W) and quantitative T1 images.

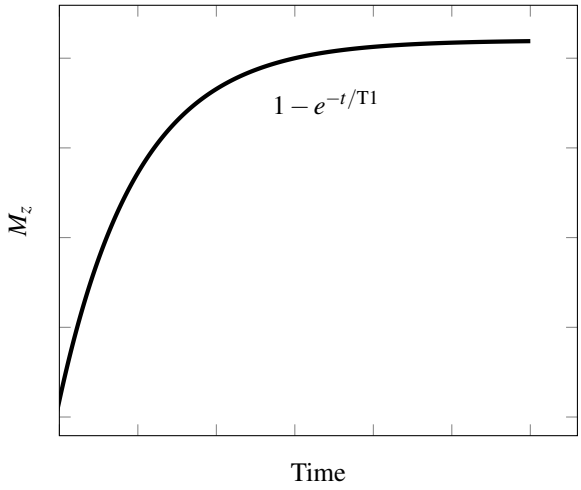

Figure 2.4: Recovery of the longitudinal magnetization vector after an RF pulse. After the RF pulse tips the net magnetization vector of the proton ensemble out of the z-plane and into the xy-plane, the magnetization vector, M_z, is slowly recovered as the proton dipole moments realign with B_0. This exponential recovery is characterized by the time constant T1.

Earlier, it was stated that the exponential decay of the transverse magnetization signal, M_{xy}, occurs because the precessing magnetic moments dephase after an RF pulse is applied, eventually leading to a net magnetic moment of zero in the *xy*-plane, and that this dephasing is caused by differences in the resonant frequencies of individual protons due to local magnetic field inhomogeneities arising from the presence of nearby protons. Such inhomogeneities may be viewed as intrinsic to the sample being imaged. A second source of magnetic field inhomogeneity is also present in any MRI experiment due to imperfections in the externally applied magnetic field, B_0; these magnetic field inhomogeneities are referred to as extrinsic inhomogeneities. Such extrinsic inhomogeneities are static, whereas the intrinsic inhomogeneities arising from molecules in a sample are in constant flux. Since extrinsic inhomogeneities are static, they can be measured and corrected for in an MRI experiment. When steps are taken to correct for extrinsic inhomogeneities, the imaging technique is a T2 method (i.e., T2-W or QT2). However, when extrinsic inhomogeneities are not corrected for, the value for the T2 decay constant is shortened, and the imaging technique is T2*-weighted (T2*-W) or a quantitative T2* (QT2*) technique.[11]

As mentioned previously, NPs with iron oxide cores less than 20 nm in diameter will exhibit superparamagnetism, which contrasts with bulk iron oxide since such large quantities of iron oxide are typically composed of both Fe^{2+} and Fe^{3+} and are characterized by ferromagnetic behavior. The unpaired electrons of iron have an associated quantum mechanical spin and form magnetic dipoles; the magnetic dipoles in iron tend to spontaneously align even in the absence of an applied external magnetic field, a phenomenon which describes a ferromagnetic material. Large crystals of Fe_3O_4 are composed of many magnetic domains; within a domain, magnetic moments are aligned, but the magnetic moments of individual domains are randomly oriented. For iron oxide crystals of sufficiently small size, approximately 70 to 150 nm, it is energetically favorable for only one magnetic domain to be present. However, once the particle size reaches 20 nm or below, the single magnetic domain persists, but the thermal energy present at room temperature is of sufficient magnitude to cause the direction of the magnetic dipole to freely fluctuate in direction. Such a freely fluctuating magnetization vector is characteristic of paramagnetic atoms. What is unique about a sufficiently small crystal of Fe_3O_4, is that it is composed of thousands of atoms, each with a mag-

netic dipole moment aligned with the other atoms leading to a large magnitude of magnetization vector, and this magnetization is free to fluctuate in direction (just like a paramagnetic atom can, but unlike the domains of bulk Fe_3O_4). These nanoscale particles of iron oxide are described as superparamagnetic, and their large magnetization vectors that are able to freely align with externally applied magnetic fields allow them to influence movement of the magnetic dipole moments of protons during MRI. As such, the presence of superparamagnetic iron oxide NPs may be indirectly detected via MRI.

Chapter 3

NONINVASIVE INVESTIGATION OF MULTI-ORGAN BIOKINETICS OF IRON OXIDE NANOPARTICLES IN SMALL AND LARGE ANIMAL MODELS USING MRI

Despite the preponderance of medical successes attributable to the engineering of iron oxide nanoparticles (NPs) extant in the experimental literature based on small animal models, widespread clinical translation of these NPs lags behind. A better understanding of how NP pharmacokinetics vary between small and large animal models is needed to rapidly customize NPs for optimal performance in humans. We capitalized on the ability for iron oxide NPs to enhance contrast in magnetic resonance imaging (MRI) to track these NPs through a large number of organ systems in vivo to investigate NP biokinetics in both mice and nonhuman primates (NHPs). We demonstrate that pharmacokinetics are similar between mice and macaques in the blood, liver, spleen, and muscle, but differ in the kidneys, brain, and bone marrow. Our study also demonstrates that full-body MRI is practical, rapid, and cost-effective for tracking magnetic NPs noninvasively with high spatiotemporal resolution. Our techniques using a nonhuman primate model may provide a platform for testing a range of NP formulations.

3.1 Introduction

Nanostructured materials have the potential to transform the diagnosis and treatment of many diseases, including neoplasms.[26] Although the number of successful preclinical NP studies is rapidly growing, NPs have been relatively slow to reach the clinic,[27] and only a few low-toxicity NP formulations have entered clinical trials.[28,29] A shared opinion in the field is the need to more fully understand how experimental NPs might distribute throughout the human body.[30–32] Such knowledge would help predict treatment effects as well as toxicity in organs of excretion and the

hematopoietic bone marrow compartment.[27,33]

It has been well established in rodent models that NP size, charge, and surface coating greatly influence biodistribution.[34–36] Murine NP biokinetics have been investigated via MRI,[37,38] radioactive labeling,[39,40] inductively coupled plasma measurement,[41,42] and visible light imaging.[35] MRI, specifically, can be repeated in vivo without ionizing radiation, and murine studies have used MRI to noninvasively monitor NPs as they traverse three to four organs over time.[34,38,43–45] A study seems overdue that demonstrates in vivo MRI tracking of particles through all major organ systems, while translating this knowledge of NP biodistribution from the common lab mouse to a species more physiologically comparable to humans. Without direct experiments, the assumption of equivalent biokinetics between mice and primates is a risky one, and it can lead to underinformed clinical trials requiring cessation due to unexpected toxicity and off-target delivery.

In this work, we report on the interspecies comparison of NP biokinetics between mice and NHPs and provide a systematic study that continuously tracks NPs in macaques using MRI through the largest number of organ systems accomplished to date. NHPs are preferred animals for preclinical identification of NP biokinetics and toxicity profiles as NHPs approximate humans in physiology and genetics more closely than any other animal.[46] MRI is a convenient tool to quickly and noninvasively test NP biokinetics in NHPs where the number of NHPs is limited and radiation quantification is not feasible or accessible. We compare in vivo organ uptake of an iron oxide NP coated with a siloxane poly(ethylene glycol) (PEG) monolayer (IOSPM) between the two species. IOSPM has a number of favorable properties supporting its use as a clinical MRI contrast agent including superparamagnetism, small and uniform size, high stability in aqueous solution, and excellent biodegradability.[47] We find that NP biokinetics are nearly identical in blood, liver, spleen, and muscle but differ in brain, bone marrow, and kidney between the two species. Our approach allows us to resolve and quantify MRI signals with temporal and spatial resolutions not obtainable by other existing noninvasive imaging modalities. The work here describes IOSPM NP organ kinetics providing valuable physiological information and presents a cost-effective, widely applicable strategy to assist in the clinical translation of NPs.

3.2 Results and Discussion

3.2.1 Characterization of the NP System

IOSPM NPs (Figure 3.1a) were designed to maximize MRI contrast and provide comparable chemical behavior to iron oxide NPs commonly used in the literature. Oleic acid-coated iron oxide NPs (IOOAs) were synthesized by thermal decomposition of iron organometallic compounds, yielding monodisperse NPs.[48] Silanization and subsequent grafting of amine-functionalized PEG displaced oleic acid from the IOOA surface, thereby enhancing water solubility.[49]

Superparamagnetic iron oxide NP core size has a significant effect on MRI relaxivity and impacts MRI contrast in vivo.[50] IOSPM NPs had a core size of 12 nm, determined by TEM (Figure 3.1b). R2 (1/T2) relaxivities of the NPs in phosphate buffered saline (PBS) were evaluated to be 45.3 and 61.4 mM^{-1} s^{-1}, at 3 T and 14 T field strengths, respectively (Figure 3.1c). A linear relationship was established between quantitative T2 (QT2) measurements and relative changes in T2*-weighted (T2*-W) signals, as particle concentration varied (Figure 3.1d).

Hydrodynamic size and surface properties of NPs are primary factors that dictate in vivo uptake, retention, and clearance.[35,51] The IOSPM NP hydrodynamic diameter was 31.5 ± 2.0 nm in PBS (Figure 3.1e), well within the range to minimize renal and mononuclear phagocyte system clearance.[51] IOSPM NPs remained stable in biologically relevant fluid, Dulbecco's Modified Eagle's Medium (DMEM) with 10% fetal bovine serum (FBS), over 10 days (Figure 3.1f). At pH 7.4, IOSPM NPs had a modestly negative zeta-potential of -14.4 ± 7.2 mV (Figure 3.1g).

A subset of IOSPM NPs was labeled with Cy5.5, a near-infrared fluorophore, to facilitate whole-organ fluorescence imaging. UV-vis spectroscopy was used to quantitate Cy5.5 labeling (Figure 3.1h). Based on the absorbance maximum (673 nm) of IOSPM Cy5.5 and the extinction coefficient of Cy5.5 (2.09×10^5 M^{-1} cm^{-1}), the molar ratio of fluorophore:IOSPM was calculated to be 50 : 1.

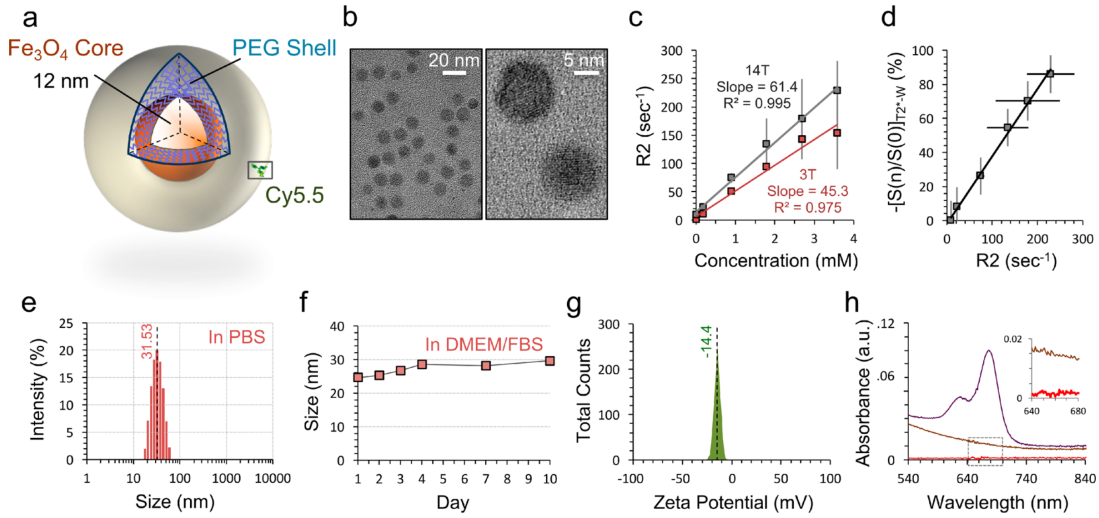

Figure 3.1: Characterization of iron oxide NPs. (a) Schematic of NP with metallic iron oxide core and amine-terminated PEG shell. The core and shell are joined by a cross-linked siloxane intermediate layer. Cy5.5 fluorophore is conjugated onto a subset of the NPs. (b) TEM of the NPs at low magnification (left) demonstrates monodispersity and spherical core shape. High magnification TEM (right) displays linear features of the iron oxide crystal lattice. (c) Magnetic T2 relaxivity of IOSPM NPs in PBS at 25°C is calculated to be 45.3 mM^{-1} s^{-1} at 3 T (red) and 61.4 mM^{-1} s^{-1} at 14 T (gray). (d) Quantitative IOSPM NP data at 14 T. NP concentrations and R2 values in (c) are plotted against respective T2*-W signal changes from baseline, demonstrating a linear relationship between these two measurement techniques. (e) Dynamic light scattering data demonstrates an average NP hydrodynamic size of 31.5 nm in PBS, with good size uniformity. (f) Monitoring of NP size in DMEM/FBS reveals < 5 nm change over 10 days, with a stable hydrodynamic size of $\sim$29 nm reached between days 4–10. (g) Zeta-potential measurement shows a net-negative particle surface charge of –14.4 mV. (h) Confirmatory biodistribution experiments in mice required fluorophore labeling with Cy5.5. UV-vis spectra for NP samples prior to Cy5.5 conjugation (brown) and after conjugation and purification (purple) confirm the presence of the fluorophore (UV-vis baseline was PBS and samples of equivalent Fe_3O_4 concentration are shown). The aqueous buffer from the purified Cy5.5-labeled sample was extracted by centrifugation (30×10^3 MW cutoff spin column) to demonstrate good binding, from an absence of Cy5.5 in the supernatant (red inset).

3.2.2 In Vivo NP Tracking in Macaque Organs

IOSPM NPs were delivered to three macaques by saphenous vein injection. As our pilot experiments show full clearance of clinically relevant low-dose IOSPM NPs (2.4 mg Fe kg^{-1}) from the blood within 4 h, we scanned animals during this time frame using interleaved QT2, quantitative T2* (QT2*), and T2*-W imaging. MRI of the head and full torso was performed using T2 mapping up to 4 h after injection (Figure 3.2). Figure 3.2a displays a T2 map of the liver before and after NP injection, with relatively consistent NP uptake (red) across the organ. A rapid change in liver T2 from 45 ms to 24 ms occurred after injection, indicative of expected first-pass metabolism. Sagittal (Figure 3.2b) and coronal (Figure 3.2c) views are provided of the upper torso, with colored regions of interest (ROIs) marked. Raw data from a multispin echo QT2 sequence (Figure 3.2d) demonstrate good signal in liver (red dashed line), spleen (green dashed line), and kidney (purple dashed line). An inset shows a separate slice of the kidney, with renal pelvis highlighted (orange).

Color-coded ROIs were used to interrogate QT2 images, with temporal T2 plots obtained from eight compartments: blood (yellow), muscle (gray), renal cortex (purple), renal pelvis (orange), spleen (green), marrow (light blue), deep gray matter (dark blue), and liver (red) (Figure 3.2e). T2 values at $t = 0$ ms were acquired immediately before NP injection. Inspection of the carotid artery lumen demonstrates an immediate post-injection change in T2, followed by elimination with a linear decay profile ($R^2 = 0.97$). From a pharmacological perspective, linear (zero-order) kinetics suggests that the elimination biomachinery of NP is saturated. The elimination half-life of the IOSPM is approximately 2 h.

Time courses from the three macaques demonstrate considerable similarity between animals. In muscle, there is little T2 change after NP injection, suggesting a negligible amount of NPs present in muscle. In liver and spleen, T2 changes rapidly and saturates for the duration of imaging, suggesting that NPs remain in the liver and spleen at 4 h. The renal cortex of three animals shows comparable profiles of NP uptake followed by elimination. MRI behavior in renal cortex is accompanied by information from the renal pelvis, the space where new urine is first expelled as it travels to the bladder. Prior to NP injection, the T2 of urine in the renal pelvis closely matches the

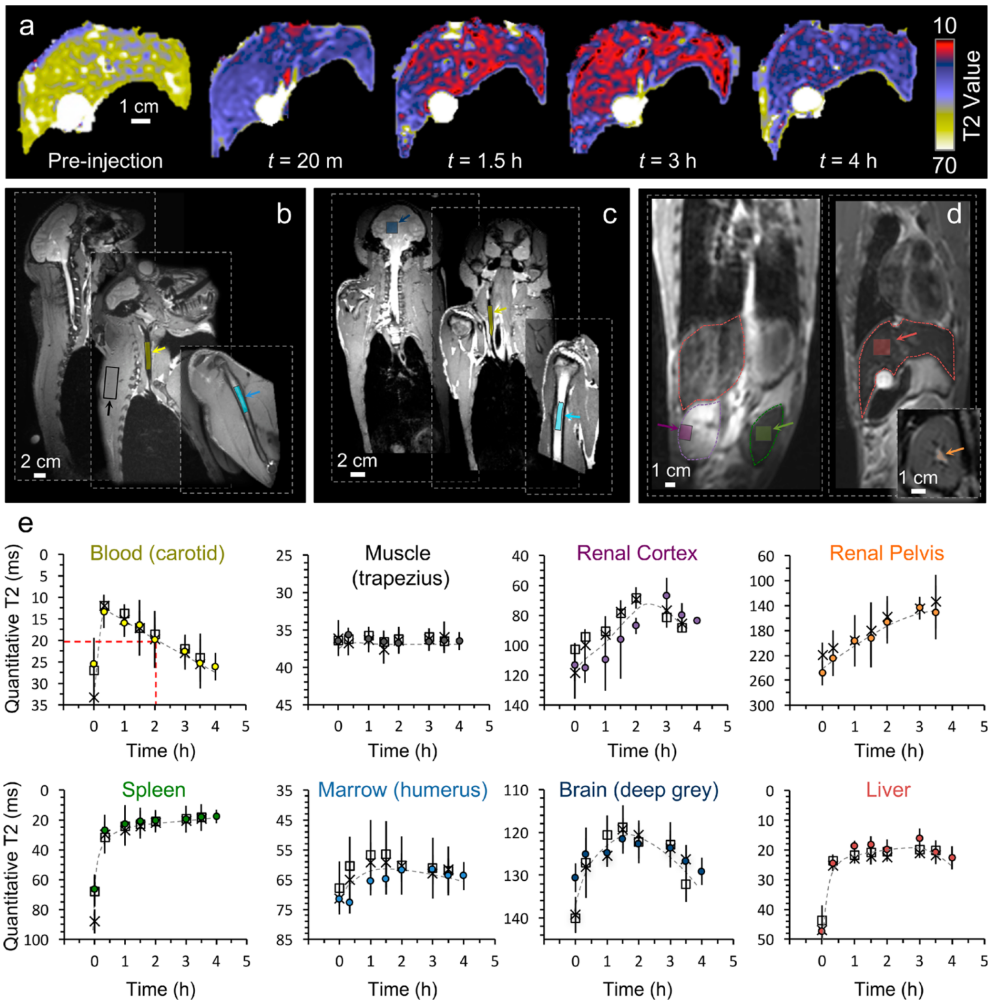

Figure 3.2: Noninvasive measurement of IOSPM NP biodistribution in macaques. (a) Quantitative T2 maps of the macaque liver show homogeneous changes in T2 throughout the organ after IOSPM NP injection. (b) Sagittal and (c) coronal T2-weighted structural images of the head and upper torso are used to display ROIs for quantitative analysis of blood (yellow), muscle (gray), bone marrow (light blue), and deep gray matter of the brain (dark blue). (d) Example raw images from the multispin-echo sequence demonstrate ROIs of the liver (red), spleen (green), and renal cortex (purple). A separate slice is used to display the renal pelvis (orange, inset). ROIs were chosen to avoid obvious large vessels within each compartment. (e) Average T2 was calculated within ROIs for each time point collected over a 4 h period. Colored circles represent T2 values from the first macaque (matched to color of respective ROIs), adjacent open squares show data from the second macaque, and $\times$ symbols designate the third macaque. Dashed gray lines are a guide to the eye. Red dashed lines added to the blood compartment highlight the equivalent bloodstream kinetics in the three macaques. Each compartment displays a signature time course. Due to positioning of slices and anatomical differences between animals, a reliable ROI within the renal pelvis could only be obtained for the second macaque scanned.

T2 of water at 3 T (∼250 ms). The T2 in the renal pelvis falls after injection and plateaus around a similar time to the renal cortex minimum (∼2 h). In the marrow and brain, T2 slowly decreases and reaches a minimum value between 1–3 h after injection. The temporal window of 4 h captures the beginning of NP elimination from marrow and brain, although a full return to baseline is incompletely visualized.

Within each organ, changes in T2 arise from a combination of intravascular and extravascular NPs. Relative blood volume can therefore be expected to influence measured T2 behavior. Although large vessels were avoided when placing the ROIs, there is no way to eliminate vascular partial volume effects. We are reassured by the disparate trends between carotid blood T2 and the T2 of other organs, suggesting that the vascular influence on organ T2 is minimal. Muscle is a compartment with high vascularity yet demonstrates negligible change. Splenic and hepatic T2 remain at a plateau even as blood T2 returns to baseline. Brain and marrow display significantly delayed NP uptake compared to the blood time course, and renal kinetics are entirely different from the signal profile in blood. Another biophysical influence that may alter T2 and T2* is the bulk magnetic susceptibility change that occurs when NPs form intracellular clusters, leading to a breakdown of quantum mechanical static dephasing assumptions.[52–54] This effect is explored in Section A.1 of Appendix A.

3.2.3 In Vivo NP Biokinetics in Mice

Mice were injected using the same dose (2.4 mg Fe kg^{-1}), MRI scanning duration (4 h), and IOSPM NP synthetic batch as the macaques. We selected nude athymic mice as our experimental model, a common choice practiced in most laboratories, to provide the greatest relevance to studies of contrast agents. Transverse cross sections of mouse anatomy from pelvis to head acquired by high-resolution 14 T MRI are shown in Figure 3.3a. IOSPM NPs exhibited greater MRI sensitivity at 14 T than at 3 T, while maintaining linearity between NP concentration and T2 or T2* (Figure 3.1c, d). Representative raw images are provided in Figure A.2 of Appendix A. IOSPM NP uptake and elimination are shown in Figure 3.3, based on the T2*-W (Figure 3.3b) and QT2 (Figure 3.3c) signal change, indicating that the elimination half-life of the IOSPM NP is ∼2 h.

Multi-animal averages are shown as colored lines, while data from individual animals are shown in gray. Excellent overall correspondence is seen between animals.

The use of interleaved T2*-W and QT2 acquisition provided high-quality data in a large number of organ compartments. With shorter overall T2 values at 14 T compared to 3 T, automated QT2 calculation was potentially prone to occasional inaccurate fitting of decay curves, especially in areas such as the liver and blood with T2 $\leq$ 20 ms. We therefore performed nonlinear curve fitting for calculation of all T2 values and have displayed representative fits in Figure A.3 of Appendix A. The spleen posed a different challenge for QT2 imaging, as the bright and dark speckled architecture generated artifact from slight respiratory motion between spin-echoes. We relied solely on T2*-W data in the spleen because of these artifacts (described in Figure A.4 of Appendix A). QT2 data were exclusively used in the liver, as high baseline iron content made the quickly decaying T2*-W signal nearly black, even prior to NP injection. The subtle T2*-W signal change in the brain was detectable with high contrast-to-noise properties of T2*-W imaging, but not with QT2 brain imaging (Figure A.5 of Appendix A). MRI was not used to interrogate the lung or heart, due to lung air spaces and cardiac motion. All T2*-W trends include linear correction of baseline signal by the intensity of an adjacent water phantom, to account for fluctuations in hardware sensitivity (Figure A.6 of Appendix A).

To support MRI-derived trends, we performed near-infrared fluorescence (NIRF) imaging of extracted organs after injection of fluorescently labeled IOSPM NPs (Figure 3.4). Prior validation of this ex vivo method showed comparable results from whole organs and histological sections.[8,55] Four groups of nude mice were used, with one group receiving no injection, and mice of the other groups sacrificed at sequential times after injection. While the addition of a fluorescent label may somewhat alter the surface properties of the NPs, key characteristics including hydrophilic coating (PEG), core size (12 nm), hydrodynamic size (27.7 nm), and zeta-potential (–12.1 mV) were similar to the nonlabelled NPs.

Figure 3.4a displays NIRF organ images, along with 200 μL of whole blood from each mouse. NP accumulation was greatest in liver, with substantial relative quantities found in blood, bone, kidney, and spleen. NIRF time courses are displayed in Figure 3.4b and agree qualitatively with

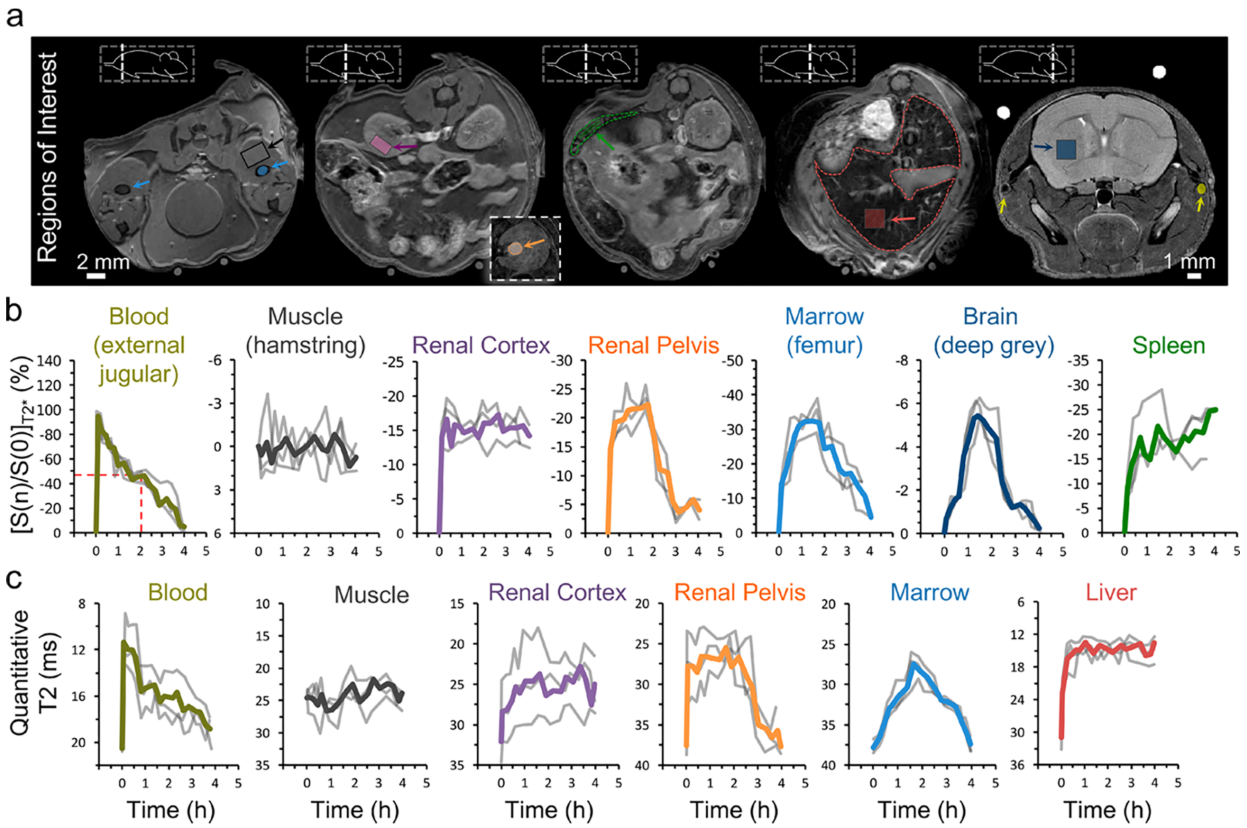

Figure 3.3: Noninvasive measurement of IOSPM NP biodistribution in mice. (a) Transverse cross sections display mouse anatomy from pelvis to head (slice position relative to the mouse shown in adjacent graphic). External jugular vein was used as the blood ROI (yellow) due to low vessel pulsatility and minimal respiratory artifact in the surrounding tissues. Hamstrings provided the largest area for muscle ROIs (black). Femur provided a consistent cylindrical compartment for bone marrow (light blue). ROIs are also shown in the renal cortex (purple), renal pelvis (orange, inset), spleen (green), liver (red), and brain (dark blue). Dashed outlines indicate borders of the liver (red) and spleen (green). Water phantom can be seen below the abdomen and above the head, with differences in phantom brightness indicative of the shorter TE used in structural imaging of the abdomen. (b) T2*-W signal change from pre-injection baseline (expressed as percent), after normalization of each value with corresponding signal produced by the water phantom. Excellent correspondence is seen over time in signal behavior between individual animals (gray). Average normalized signal change between animals is displayed as the colored line. T2*-W signal change after NP injection could not be reliably determined in the liver due to low T2*-W signal at baseline. (c) Quantitative T2 imaging provides trends for the blood, muscle, renal cortex, and renal pelvis consistent with T2*-W data. Spin-echo refocusing allows visualization of signal change in the liver.

MRI trends. We observed a linear correlation between MRI and NIRF data ($R^2 = 0.93$–0.96) (Figure 3.4c). Representative QT2 comparisons with NIRF are shown for renal cortex and liver, and T2*-W comparison data with NIRF are shown for marrow and brain.

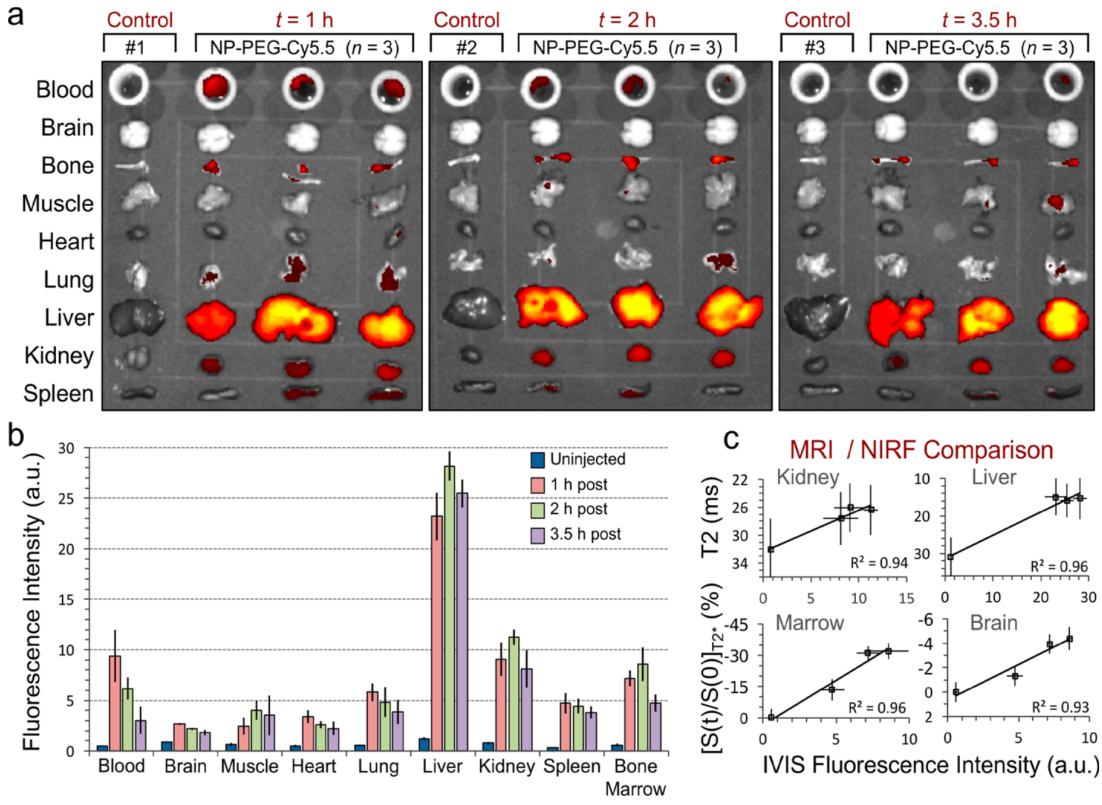

Figure 3.4: NIRF imaging of whole-organ NP uptake. (a) 12 mice were used to confirm in vivo MRI patterns of IOSPM NP biodistribution with ex vivo organ fluorescence intensity measurement. Consecutive panels show blood (200 µL) and whole organs (brain, bone, muscle, heart, lung, liver, kidney, and spleen) from mice sacrificed at 1, 2, and 3.5 h post-injection. Organs at each experimental time point were imaged alongside organs from separate noninjected control mice. Images display the highest IOSPM-Cy5.5. NP uptake in the liver, with visible fluorescence change in the blood, bone, lung, kidney, and spleen. (b) Fluorescence intensity in all organs was calculated and is displayed graphically for each time point. Error bars represent ± standard deviation of the mean from the three independent measurements. (c) A direct comparison between MR and fluorescence results suggests a linear relationship between the two measurement techniques. Such linearity is demonstrated both for examples using QT2 imaging (displayed for the kidney and liver) and with T2*-W imaging (shown in the marrow and brain). R^2 values ranging from 0.93 to 0.96 are shown, adjacent to the respective linear fits.

3.2.4 Interspecies Biokinetics are Organ Dependent

T2*-W changes are displayed within the mouse and macaque brain, 30 min after NP injection (Figure 3.5a). These scans show predominant intravascular NP effects (color threshold = 10% change). From an examination of Figures 3.2 and 3.3, we know that signal changes occur in areas of the deep gray matter chosen to avoid large vessels. These signal changes are smaller ($\sim$6%), delayed in peak uptake and elimination compared to blood signal, and highly reproducible between animals. The signal profile in large vessels (e.g., sagittal sinus, white dashed line) achieves an immediate peak and displays zero-order elimination kinetics, similar to behavior of the carotid.

Figure 3.5b shows a direct comparison of macaque and mouse biokinetics, with mouse data subsampled at equivalent time points to macaque data and trends scaled so that minimum and maximum values in either species were recalibrated to values of 0 and 100, respectively. Using these amplitude-matched curves, the relative difference between macaque and mouse was calculated. In the renal pelvis at 1 h, the mouse displayed an approximatey $2\times$ greater signal change compared to the macaque, and -50% is displayed on the comparison plot; at 3 h, the mouse trend shows nearly complete washout, while the macaque trend was at its peak, and therefore, a large positive difference ($+80\%$) is displayed. Despite dissimilar kinetics in the kidney and prolonged elimination from macaque brain and marrow, IOSPM NP kinetics are similar in blood, liver, spleen, and muscle. MRI profiles in the blood are further supported by highly linear correlation with macaque plasma iron measurement (Figure 3.5c) and mouse blood fluorescence measurement (Figure 3.5d). Plasma iron data show a 9 μg mL^{-1} variation over the 3.5 h period of MRI data collection. Zero-order iron elimination from the macaques occurs at a rate of 2.6 μg mL^{-1} h^{-1}, corresponding to the T2 reduction of 7.3 ms h^{-1}.

3.2.5 NP Acute Toxicity Evaluation in Macaques

Macaque clinical laboratory data are shown in Figure 3.6. Prior work demonstrated a lack of murine toxicity for a similar NP base formulation.[8] Insepction of macaque cell count (Figure 3.6a) reveals no elevation outside of reference ranges in white blood cells (WBC; reference range in

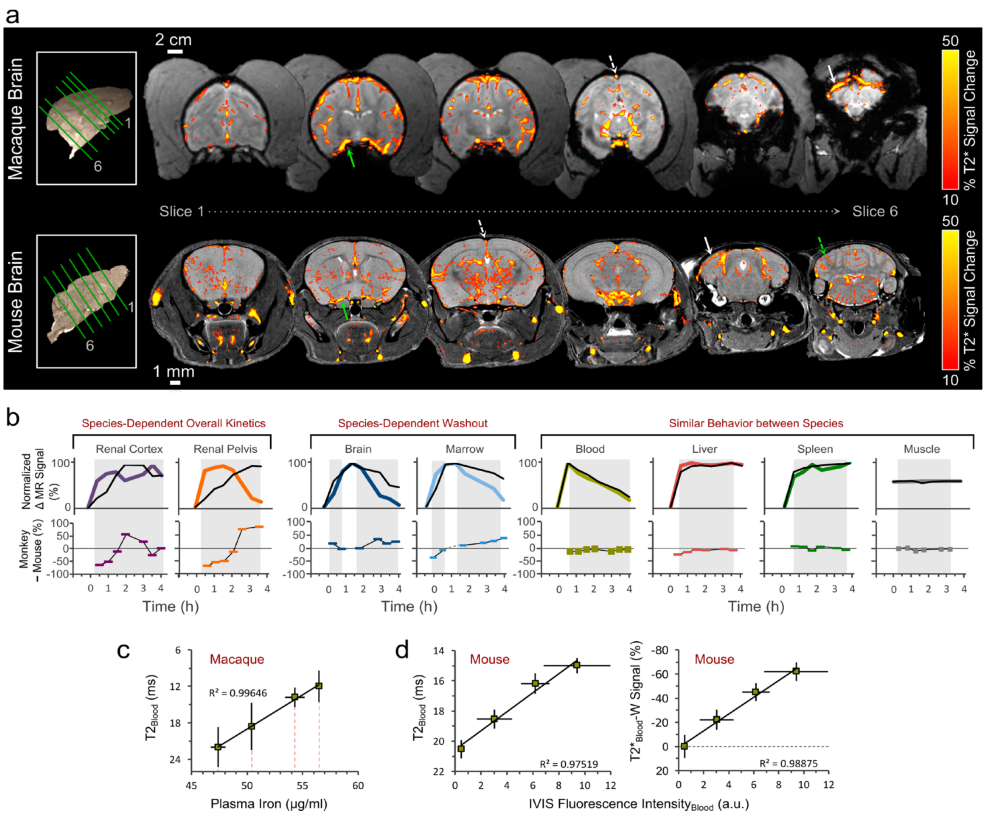

Figure 3.5: Interspecies comparison of IOSPM biodistribution. (a) For both species, the largest intracranial NP signal change occurs in the vasculature. T2*-W signal is shown across six brain slices, 30 min after NP injection, for macaque (top row) and mouse (bottom row). A minimum threshold of 10% eliminates visible signal change from most regions other than the large vessels, which display localized signal changes up to 60%. NP highlights the deep cerebral draining veins in both species and, in the case of the mouse, generates small signal markings from radially oriented vessels in the cerebellum (dashed green arrow). Solid green arrow depicts middle cerebral artery, dashed white arrow points to superior sagittal sinus, and solid white arrow points to transverse sinus. (b) The relative kinetics of NP uptake and elimination are compared between mouse (colored line) and macaque (black line), by modifying the observed minimum and maximum signal changes to exist on a range from 0 to 100%. Data from the mouse, which were obtained at higher temporal frequency, were subsampled using only points acquired at equivalent times to the macaque. The equivalently scaled data were then subtracted, with negative values signifying greater relative uptake in the mouse and positive values signifying greater relative uptake in the macaque (bottom plots in b). Shadowed regions indicate data that were used in the comparison. (c) A linear relationship is seen ($R^2 = 0.996$) between macaque blood T2 values and directly measured inductively coupled plasma iron content of blood samples. (d) A linear relationship is observed between mouse bloodstream T2 values and blood NIRF intensity ($R^2 = 0.975$, left plot). Change in T2*-W signal displays a similarly linear relationship with NIRF blood fluorescence intensity ($R^2 = 0.989$, right plot).

macaque = 8.1–15.4 $\times 10^3$ cells μL^{-1}), which would otherwise indicate an immune response. However, the percentage of neutrophils showed a minimal, transient increase at 4 h post-injection but returned to baseline by 2 weeks, indicating possible mild, acute stress. Considering the prolonged retention of IOSPM NPs in the macaque bone marrow, it is important to see no evidence of bone marrow toxicity, which could be marked by dropping hematocrit (Hct), WBC, or platelet levels. However, no significant drop in Hct, WBC, or platelets was observed indicating a lack of acute bone marrow toxicity.

Liver enzymes (Figure 3.6b) showed no significant elevation of aspartate transaminase (AST), alanine aminotransferase (ALT), alkaline phosphatase (ALP), or γ-glutamyl transpeptidase (GGT). In addition, there was no elevation of albumin or total bilirubin levels, indicating normal liver function and absence of acute hepatoxicity. Review of blood chemistries reveals maintenance of electrolyte balance throughout IOSPM NP injection (Figure A.7 of Appendix A). MRI biodistribution data show that renal NP clearance is delayed in the macaque, and there is no elevated creatinine (Cr) or abnormal blood urea nitrogen (BUN)/Cr ratio that would suggest kidney dysfunction. These results confirm that IOSPM NPs have no acute toxicity to bone marrow or liver and display no apparent immunogenicity, which overcomes a major barrier for its clinical translation as a contrast agent.

3.3 Materials and Methods

3.3.1 Materials

All chemicals were purchased from Sigma-Aldrich (St. Louis, MO, USA) unless otherwise specified. 3-(Triethoxysilyl)propyl succinic anhydride (SATES) was purchased from Gelest (Arlington, VA, USA). 2000 MW monoamine functionalized poly(ethylene) glycol (mPEG2K-NH_2) was purchased from Laysan Bio (Arab, AL, USA).

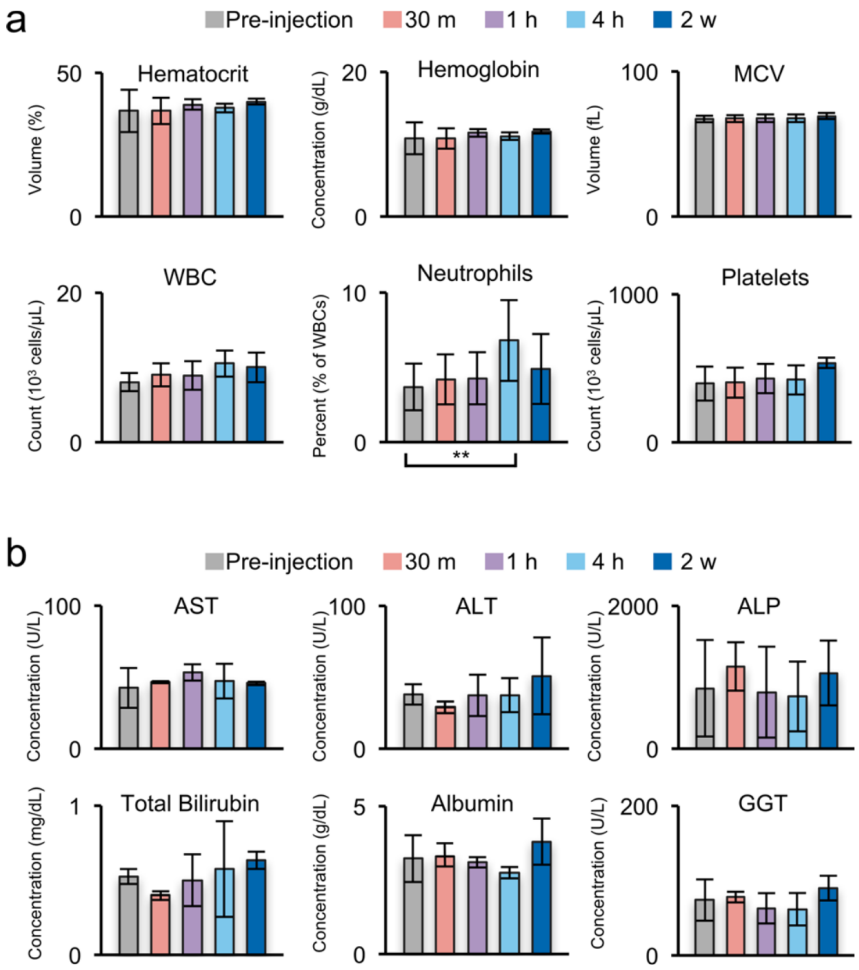

Figure 3.6: Macaque laboratory values before and after IOSPM injection. (a) Complete blood cell count, and (b) liver enzymes are displayed for three macaques. A minimal increase in the percent of WBC count corresponding to neutrophils ($^{**}p < 0.05$) were observed 4 h post-injection; however, these values returned to normal by 2 weeks. WBC count remained below laboratory criteria for abnormal elevation in the macaque ($< 14 \times 10^3$ cells μL^{-1}) (a). Liver enzymes showed no significant change over the course of the study (b). Averages and standard deviations were determined from blood samples of four macaques.

3.3.2 NP Synthesis and Coating

50 mg of IOOA was suspended in 43 mL of anhydrous toluene, followed by addition of 50 µL of triethylamine in a three-neck round-bottom flask fitted with a Graham condenser. The flask was sealed with rubber septa and purged with nitrogen. The solution was heated to 100°C, and 0.10 mL of SATES was added to the flask. 187.5 mg of mPEG2K-NH_2 was dissolved in 7 mL of anhydrous toluene, and the resultant solution was added to the flask 15 min after the addition of SATES. An additional 50 µL of SATES was injected 1 h after the mPEG2K-NH_2 injection, and the solution was reacted for a further 6 h and 45 min. The solution was transferred to a single-neck round-bottom flask, and NPs were precipitated with hexane. The NP precipitate was dispersed in tetrahydrofuran (THF), sonicated for 10 min, and precipitated with hexane. The resulting NP pellet was suspended in 10 mL anhydrous THF and sonicated for 10 min. 62.5 mg of mPEG2K-NH_2 and 187.5 mg of 2000 MW bis(amine) functionalized PEG (PEG2K-bis(amine)) were dissolved in 12 mL of anhydrous THF and added to the NP solution. The flask was then sealed with a septum and purged with nitrogen. 12.5 mg of N,N^1-dicyclohexylcarbodiimide was dissolved in 2 mL of anhydrous THF and added to the flask, the reaction solution was placed in a sonication bath at 25ºC and allowed to react for 16 h. Fully PEGylated NPs were precipitated with hexane, redispersed in 20 mL ethanol, sonicated for 10 min, and precipitated again with hexane. The pellet was fully dried and dispersed in PBS with sonication for 10 min.

3.3.3 NP Size and Zeta Potential Characterization

The initial hydrodynamic size of NPs was analyzed at 100 µg mL^{-1} in PBS (pH 7.4). NP stability in biological fluid was analyzed at 100 µg mL^{-1} in DMEM supplemented with 10% FBS and 1% antibiotic-antimycotic. The zeta potential of NPs was analyzed at 100 µg mL^{-1} in 20 mM HEPES buffer (pH 7.4).

3.3.4 TEM Analysis of NPs

Samples were prepared by diluting NPs to 100 μg mL^{-1} in deionized H_2O, and 5 μL of the dilute solution was placed on a Formvar/carbon-coated 300 mesh copper grid (Ted Pella Inc., Redding CA, USA). After 5 min, the NP solution was removed, and the grid was allowed to dry overnight before imaging.

3.3.5 Cy5.5 Labeling

IOSPM NPs (2 mg) were reacted with 0.5 mg of Cy5.5 (GE Healthcare, Piscataway, NJ, USA) in 100 mM sodium bicarbonate buffer, pH 8.5 for 1 h at room temperature, protected from light and with gentle rocking. The resultant IOSPM-Cy5.5 NPs were purified using size-exclusion chromatography in S-200 resin equilibrated with PBS and stored at 4°C. UV-vis spectrophotometric analysis was performed for Cy5.5-labeled samples. Data used for display (Figure 1h) were blanked against PBS. The system was then blanked with NPs in PBS and absorbance (673 nm) was determined for IOSPM-Cy5.5 NPs at an equivalent Fe concentration. Using an extinction coefficient of 2.08×10^5 $M^{-1}cm^{-1}$ and an NP molecular weight of 2×10^6 g mol^{-1}, the number of fluorophores per NP was determined to be 50. PBS solvent from Cy5.5-labeled samples was extracted by centrifugation in a 30×10^3 MW cutoff spin column, with UV-vis testing performed on this sample to confirm lack of a Cy5.5 peak.

3.3.6 Nanoparticle Administration

Sterile prepared IOSPM NPs were transferred into medical-grade saline (pH 7.5) and injected at a dose of 2.4 mg Fe kg^{-1} for both mice (nude athymic) and macaques (*Macaca nemestrina*). NPs were administered in mice by tail vein injection over 5 s and in macaques by saphenous vein injection over 5 min. All procedures were performed in accordance with the University of Washington Institutional Animal Care and Use Committee. Injected IOSPM NP volume was ∼18 mL in macaque experiments and ∼120 μL in mouse experiments, with individual injection volumes adjusted for exact animal weight. Three macaques were approved for MRI scanning on the current

protocol. Four macaques were approved for clinical laboratory evaluation of blood counts, blood chemistry, and liver enzymes. Six mice were utilized for MRI experiments, and 12 mice were used for a confirmatory fluorescence-based study of IOSPM-Cy5.5 NP biodistribution over the 4 h after injection. In this confirmatory mouse experiment, 200 μL of blood and whole extracted organs were harvested pre- and post-injection and examined using NIRF imaging (IVIS Lumina II system, PerkinElmer).

3.3.7 In Vivo Mouse MRI

Mice were scanned with a Bruker 14 T vertical-bore imaging system (Ultrashield 600 WB Plus). Three mice were positioned in a 25 mm single-channel ^{1}H radiofrequency (RF) receiving coil (PB Micro 2.5) centered on the abdominal region, and three separate mice were positioned with the head and neck at isocenter. Use of these two scanning groups was necessary for imaging of the head and full torso, given the limitations in coil length (longitudinal field of view 6 cm). Head/neck imaging included a structural rapid acquisition with refocused echoes (RARE) sequence (TR/TE = 4000/27 ms, in-plane resolution 52 × 78 μm^2, matrix 384 × 256), T2*-weighted (T2*-W) 2D fast low-angled shot (FLASH) sequence (TR/TE = 1000/6 ms, in-plane resolution 98 μm^2, matrix 256 × 256), and quatitative T2 (QT2) multispin multiecho (MSME) sequence (TR = 4000 ms, TE = 6.7 + 6n ms, $[n = 0–16]$, in-plane resolution 52 × 78 μm^2, matrix 384 × 256). Abdominal scans maintained the same slice thickness, but were prescribed with a larger field of view, used respiratory gating, and the following different parameters: structural RARE sequence (TR/TE = 691/5.5 ms, in-plane resolution 65 × 97 μm^2, matrix 384 × 256), T2*-W sequence (in-plane resolution 98 μm^2, matrix 256 × 256), QT2 sequence (in-plane resolution 97 × 195 μm^2, matrix 256 × 128). Total image time for each sequence was approximately 4 min. Slices for sequential scans on a single mouse were prescribed identically, with 0.5 mm slice thickness. For head/neck scans, 14 coronal slices were positioned from the olfactory bulb extending to the cerebellum. For abdominal scans, 20 slices were positioned in the transverse plane with 0.75 mm interslice gap allowing coverage from the liver to the pelvic floor.

3.3.8 In Vivo Macaque MRI

Macaques were scanned with a Phillips 3 T Achieva MRI. All scans were obtained with respiratory gating. Baseline structural T2-W 3D turbo spin-echo images (TR/TE = 2500/250 ms, resolution 1 mm^3, matrix 452 $\times$ 226), QT2 2D turbo spin-echo images (TR/TE = 5000/12 + 12n ms, $[n = 0–8]$, in-plane resolution 0.94 mm^2, matrix 228 $\times$ 113, slice thickness 4 mm), and 3D quantitative T2* (3D fast-field echo sequence, TR/TE = 75/6.9 + 6.9n ms,$[n = 0–8]$, resolution 0.94 $\times$ 0.94 $\times$ 4 mm^3, matrix 228 $\times$ 228 $\times$ 113) were obtained in coronal orientation over a body region spanning from the top of the head to the pelvis. 3D T2*-W images were obtained of the head only, in an oblique plane (TR/TE = 45/25 ms, resolution 0.89 $\times$ 0.89 $\times$ 4 mm^3, matrix 100 $\times$ 100). Interleaved scanning of brain (T2*-W) and head/torso (QT2) was performed after NP administration. Scan times were 6.2 min (T2W structural image), 20.3 min (QT2 image), and 1.9 min (T2*-W image).

3.3.9 Magnetic Characteriztion of Aqueous NP Samples

NP phantoms were constructed via dilution of concentrated IOSPM NP stock to concentrations of 0, 10, 50, 100, 150, and 200 μg mL^{-1} in PBS. Tubes containing NPs were 2 mm in diameter for 14 T phantoms and 1 cm in diameter for 3 T phantoms. Sample tubes containing NPs were fixated and surrounded by a homogeneous external PBS medium to minimize magnetic susceptibility fluctuations around the samples. Imaging of phantoms was performed using the same QT2 and T2*-W sequences used for in vivo imaging. T2 values as well as T2*-W signal changes induced by the NPs at each concentration were determined within circular 50-voxel ROIs at either field strength.

3.3.10 MRI Data Analysis

Analysis of MRI data was performed using FMRIB software library (FSL),[56] Bruker Paravision 5.1 analytic package, Phillips integrated software, Osirix (Pixmeo), and Matlab (Mathworks). Processing stages for QT2 and QT2* data included (i) ROI definition, (ii) automated T2 value calculation within the ROI (Paravision 5.1 or Phillips software), (iii) manual T2 calculation within the ROI by exponential least-squares fitting of the raw spin-echo data (Matlab), and (iv) translation of the

ROI over all images in the 4D time-series, using anatomical landmarks to confirm appropriate ROI placement. Imaging of the head/neck in both macaques and mice permitted automated rigid body registration/motion correction prior to the four analysis steps above (FSL, 3 degrees-of-freedom). Due to peristaltic movement within the abdomen and the noncylindrical image contour, image registration could not be used reliably on body images.

Analysis of nonquantitative T2*-W data involved normalization of intensity within each image by signal amplitude of the adjacent water phantom to correct for temporal fluctuations in hardware sensitivity and scan-to-scan differences in the pulse power/receiver gain settings. ROIs were defined and interrogated in an equivalent manner to QT2 and QT2* scans. ROIs were placed in locations that captured the largest possible area of an organ compartment. In placing ROIs, caution was taken to avoid the capsule or external margin of a given organ. Although all parenchymal ROIs inevitably contain partial volume artifact from intervening vascular structures, effort was made to avoid obvious large vessels within the selected region. Areas contaminated with vessel pulsatility artifact or respiratory artifact were avoided. The choice of common carotid artery for vascular ROI in the macaque was made, as this vessel was easily identifiable and was visualized within the slice plane for a long distance in all macaques scanned. Pulsatility artifact was not obvious for the common carotid, given the selected imaging parameters and slice orientation. The greater T2 value of the carotid vessel wall provided a good visual boundary to ensure accurate placement of the ROI. Although readily identifiable on imaging, larger vascular structures (e.g., aorta, vena cava) were not chosen as vascular ROIs due to the common aortic pulsatility artifact, which also affected the nearby vena cava. Choice of external jugular vein for vascular ROI in the mouse was made primarily due to the large size of this vessel and lateral location in the neck. Within more central regions of the mouse neck, respiratory artifact from the trachea would intermittently overlap with the central vascular structures. Use of ear-bars for head fixation further reduced motion artifact in the head and neck, making the external jugular vein an attractive vascular choice compared to larger structures within the thorax or abdomen that could not be rigidly fixed in place. Given the anatomy of the two species and requisite position in the MRI coils, different regions were chosen to interrogate the signal from muscle and bone marrow. In the macaque, the shoulder and arm

were contained entirely within the torso acquisition window, allowing placement of ROIs in the trapezius muscle and humeral medullary compartment; in the mouse, natural folding of the legs into the 25-mm coil for abdominal imaging made hamstring and femur optimal choices for muscle and bone marrow ROIs, respectively. A complete list of ROI sizes is included in Table A.1 of Appendix A.

Colorized maps of signal change within the brains (Figure 3.5a) were produced by digital image subtraction of co-registered T2*-W images pre- and 30 min post-IOSPM NP injection. Maps were thresholded at 10% of maximum signal change and overlaid on baseline structural images.

Data analysis to produce baseline-corrected comparative signal change plots for mouse and macaque (Figure 3.5b) involved transformation of the averaged curves, with pre-injection signal arbitrarily called 0% and max signal change during the 4 h time course called 100%. Although time between comparable scans for the mouse was $\sim$10 min, macaque data was separated by a time delay of 30 min. Mouse data were therefore sub-sampled for this analysisn to include only the data points acquired at the same times as macaque data. The appearance of noise for mouse data is therefore artificially reduced in this representation, due to the inclusion of fewer values. Comparison was then performed by subtraction of normalized mouse values from normalized macaque values. The first data value (0%) was not included in this analysis, since it was artificially normalized to 0% for both mouse and macaque. If the max signal change occurred at the same time delay after NP injection for mouse and macaque (e.g., 100% at 20 min), these data were also not included in the comparison. Inclusion of data in the comparative analysis was denoted by the presence of a gray rectangle surrounding the data.

Interleaved QT2* and QT2 data were obtained from the first macaque, using equivalent ROIs in the blood (common carotid artery), muscle, renal cortex, bone marrow (humerus), brain (deep gray matter), and liver.

3.3.11 Plasma Half-Life

Macaque blood samples for inductively coupled plasma measurement were collected at 0.5, 1, 2, and 4 h post-NP injection, and plasma was prepared by centrifugation of whole blood at $2,000 \times g$

for 15 min at 4°C. 80 μL of plasma was reacted with 120 μL of 12 M hydrochloric acid overnight at room temperature and diluted to 6 mL with deionized water (75× dilution). Three aliquots (1 mL) each of the prepared blood plasma solutions were analyzed three times each by inductively coupled plasma atomic emission spectroscopy to determine the iron content of the samples.

3.3.12 Whole-Organ Fluorescence Measurement

NIRF imaging was performed on an IVIS Lumina II system (PerkinElmer, Waltham, MA, USA). A total of 12 nude mice were used for the confirmatory biodistribution experiment. Cy5.5-labeled NPs were administered by lateral tail vein injections into 9 mice, with groups of 3 mice sacrificed at 1, 2, and 3.5 h. Three additional mice were used as noninjected baseline fluorescence controls. Immediately after sacrifice, 200 μL blood samples were obtained from each mouse, and organs were harvested. NIRF images were acquired on an IVIS system, with excitation and emission filters for Cy5.5. Fluorescence data were analyzed using oval ROIs placed around the external border of each organ. Whole organ photon counts were averaged over the three animals in each of four groups.

3.4 Conclusions

Recognizing and understanding interspecies differences is critical for future translational studies to assess organ targeting and toxicity. One of the hurdles that usually delays translation of nanomedicine technologies from the benchtop to clinical practice is that we are not sure whether a given NP that works well in small animal models will still work the same in humans. This is mainly because the animal experiments were usually focused on one species and lack systematic comparisons between species. Here we used noninvasive MRI to track IOSPM NPs through several important organs in vivo to investigate the biokinetics of NPs in both mice and macaques. We used IOSPM NPs due to their potential to serve as next-generation clinical contrast agents that provide functionality to facilitate applications for cancer therapy. Several iron oxide NPs including Feridex, Combidex, and Ferumoxytol were approved by the FDA a decade ago for use as clinical

contrast agents in MRI and in iron replacement therapy.[57,58] However, their widespread use is limited due to issues with their stability and lot-to-lot variability as a result of the sensitivity of their physicochemical characteristics to manufacturing conditions.[58,59] These first-generation iron oxide NPs had simple, physically absorbed coatings that lacked functionality. By contrast, IOSPM NPs developed in our lab have long-term colloidal stability and consistent physicochemical properties due to the presence of a highly dense and stable PEG coating.[47] Furthermore, IOSPM NPs have a simple and well-defined composition, and both PEG and iron oxide are commonly used in humans as a component of drug formulations and contrast agents, respectively. The dense PEG coating and functional amine groups allow for further modifications of the base IOSPM NPs for specific targeting of cancer and delivery of therapeutics.[60]

We used 14 T MRI to acquire MR images of mice and 3 T MRI to obtain MR images of macaques. Different field strengths were used because mouse anatomical structures are an order of magnitude smaller than those of the macaque (see Figures 3.2b and 3.3a), and imaging at a high spatial resolution of MRI allowed us to average over a similar number of voxels in the mouse and macaque (see Table A.1 of Appendix A), resulting in a commensurate comparison of cross-species NP biokinetics. We took several approaches to improve MRI quantitation including the creation of custom holders to keep the animals well-positioned with respect to the gradients during imaging, control of respiratory gating, using rationally designed scan sequences, applying T2*-W or QT2 imaging to acquire data from different tissues based on their physiological properties, judicious placement of ROIs to avoid large vessels, and choosing the external jugular vein for our vascular ROI to avoid aortic pulsatility associated with larger vascular structures. We were able to detect the subtle signal change (6%) in the brain with high contrast-to-noise using interleaved T2*-W imaging (see Figures 3.2, 3.3, and A.5 of Appendix A), a much more sensitive technique than conventional MRI QT2 imaging which typically has a lower limit of detectable signal change around 10–20%.

The biokinetics of IOSPM NPs in mice and macaques is similar in the blood, liver, spleen, and muscle. QT2 and T2*-W data from blood demonstrated zero-order eliminations kinetics, with near-complete return to baseline within 4 h. The IOSPM NP profile in blood determined by MRI

is consistent with macaque plasma iron measurement (Figure 3.5c) and mouse blood fluorescence (Figure 3.5d). Our data suggest that in vivo T2 measurement of blood can function as a surrogate for relative plasma NP content in cases where invasive blood sampling is undesirable. In liver and spleen, T2 changes rapidly and saturates for the duration of imaging, suggesting increased NP uptake by the liver and spleen, and NPs remain in the liver and spleen at 4 h. NPs entered liver and spleen primarily by sinusoidal vasculatures lined by macrophages.[10,61] The similar uptake by liver and spleen cross species might be due to the similar density of vasculatures across the species and low uptake of IOSPM NPs by macrophages. Our previous study showed that the highly dense and strongly bound PEG coating on iron oxide core NPs resulted in low nonspecific protein adsorption onto NPs and a low uptake of NPs by macrophages.[47] Macrophages in the livers of mice and NHPs are reported to be different.[62] Other studies show that iron oxide NPs degrade over time and disappear in approximately 3 weeks after introduction to the liver.[42,63] Within the liver, opsonization by macrophages, followed by degradation within acidic endosomes is the primary mechanism for NP degradation.[14] Studies show no apparent difference exists in the main enzymes that play a critical role in the metabolism and pharmacokinetics of xenobiotics in the liver among species including man.[64] Both mice and monkeys showed little T2 change in muscle after NP injection, suggesting a negligible amount of NPs present in muscle.

The biokinetics of IOSPM NPs in mice and macaques is different in kidneys, brain, and bone marrow. The kidney was revealed to be the compartment with the greatest interspecies difference in biokinetics (Figure 3.5b). Compared to the other plots of Figure 3.5b, the NP kinetics of the kidney is much more divergent between the species than the other organs of interest. It is necessary to emphasize that our method does not specify relative amounts of renal excretion in either species. Obtaining such information would be possible through bladder catheterization and/or radiotracer monitoring. However, our data provide relative temporal trends in renal uptake and washout during the time that NPs persist in blood. Prior work has suggested that careful attention to renal clearance is necessary to avoid unexpected renal toxicity in human NP applications.[65] MRI signal change within the renal pelvis indicates that renal clearance of IOSPM NPs occurs with a greater time delay in the primate compared to the mouse. The observed differences in renal clearance may be

explained by species-dependent variations in glomerular filtration rates (GFR).[66] GFR, in general is inversely correlated with body mass or body surface area,[67] suggesting that the IOSPM NP renal clearance delay observed in macaques may be amplified in humans. These results confirm that utmost caution must be taken when making predictions regarding elimination of NPs by the human kidney.

Bone marrow displayed dissimilar washout kinetics with macaques exhibiting delayed washout of IOSPM NPs as compared to mice (Figure 3.5b). Marrow is a region of great clinical interest, as prolonged retention can have both positive implications for treatment studies of hematological malignancy and negative implications for off-target bone marrow toxicity during the treatment of other organ systems. NHPs are relatively rich in lymphocytes, while nude athymic mice lack mature T cells, however, it is unlikely the washout difference is due to an immune response since it would be expected that the reaction would take place faster in the monkeys containing intact T cells.[68] Researchers have previously shown that macrophages play a key role in observed species-dependent differences in bone marrow uptake of liposomal NPs,[69] and macrophage activity may explain similar differences observed with IOSPM NP washout; however, further studies are needed to elucidate the role of macrophages in NP bone marrow uptake and washout.

It is known that iron oxide NPs are capable of passively crossing the intact blood-brain barrier (BBB) in small quantities, with the extent of crossing often augmented intentionally through active mechanisms such as the use of homing ligands.[70] Here, we observed brain uptake of IOSPM NPs for both mice and NHPs, with washout delayed in the NHPs. Complete return of blood T2 signal to baseline within 4 h eliminates blood partial volume effects as a possible explanation for these findings, confirming actual retention of NPs within the brains of the macaques. The delayed washout from the macaque brain is likely due to NP-induced endothelial leakiness[21] and effects from species-dependent differences in cerebral spinal fluid turnover rate.[71] Expression of many membrane proteins that are determinant of endothelial permeability at the BBB are greater in mice than monkeys and could be partially responsible for the observed washout differences.[72] In addition, species differ not only at the expression level of transporter proteins but also in functional activity, and more research is needed to understand the implications of these differences on NP

uptake and washout in the brain. Turnover rates of cerebral spinal fluid are species dependent with mice and rats exhibiting far greater turnover rates than larger animals such as dogs, NHPs, and humans.[73] This species difference could play a major role in uptake and washout of hydrophilic compounds such as IOSPM NPs, as high cerebral spinal fluid flow rates may minimize diffusion of these hydrophilic particles into target tissue.[71]

In summary, we have systematically investigated PEGylated iron oxide NP biokinetics in macaques for the largest number of organ systems accomplished to date and have compared the biokinetics between macaques and mice. We found that blood T2 measurement can serve as a reliable surrogate for blood sampling. We conclude that NP biokinetics in primates and mice are similar in the majority of compartments including blood, liver, spleen, and muscle but differ in kidneys, marrow, and brain for our NP formulation. Our findings provide researchers important information on whether NP biokinetics in NHPs is necessary in preclinical tests of similar NPs based on the targeted application of specific organs, which can significantly reduce costs for preclinical testing. Further, our study demonstrated that full-body MRI is practical, rapid, and cost-effective for tracking NPs noninvasively in macaques with high temporal and spatial resolutions. The approach we developed here may be further used as a platform for testing other nanomaterial formulations and provide interesting springboards to understand important interspecies distinctions.

Chapter 4

CONVECTION-ENHANCED DELIVERY OF IRON OXIDE NANOPARTICLES TO A HUMAN GLIOBLASTOMA MOUSE MODEL ASSESSED USING MRI

Convection-enhanced delivery (CED) provides direct access of infusates to brain tumors; however, clinical translation of this technology has not been realized because of the inability to accurately visualize infusates in real time and the lack of targeting modalities against diffuse cancer cells. In this study, we use time-resolved magnetic resonance imaging (MRI) to reveal the kinetics of CED processes in a glioblastoma (GBM) model using iron oxide nanoparticles (NP) modified with a glioma-targeting ligand, chlorotoxin (CTX). Mice bearing orthotopic human GBM tumors were administered a single dose of targeted CTX-conjugated NP (NPCP-CTX) or nontargeted NP (NPCP) via CED. High-resolution T2-weighted, T2*-weighted, and quantitative T2 MRI were used to image NP delivery in real time and determine the volume of distribution (V_D) of NPs at multiple time points over the first 48 h post-CED. GBM-specific targeting and intracellular NP localization were evaluated by flow cytometry and histologic assessment, respectively. NPCP-CTX produced a V_D of 121 ± 39 mm^3 at 24 h, a significant increase compared with NPCP, while exhibiting GBM specificity and localization to cell nuclei. Notably, CED of NPCP-CTX resulted in a sustained expansion of V_D well after infusion, suggesting a possible active transport mechanism, which was further supported by the presence of NPs in endothelial and red blood cells. In summary, we show that time-resolved MRI is a suitable modality to study CED kinetics, and CTX-mediated CED facilitates extensive distribution of infusate and specific targeting of tumor cells.

4.1 Introduction

CED is an alternative infusate delivery method aimed at addressing limitations of systemically delivered drugs for treatment of neurologic diseases such as GBM.[74] The use of conventionally administered chemotherapy is hindered by the presence of the blood-brain barrier (BBB) that prevents many chemotherapeutics from reaching brain tumors.[75] CED bypasses the BBB affording direct delivery of infusates to tumor by slow infusion through a cannula within the tumor mass and provides broad distribution of infusate facilitated by positive pressure gradients that drive convection within the brain.[76] The fluid convection process of CED provides considerably better V_D than direct diffusion-controlled delivery methods such as implantable delivery wafers (Gliadel) and intraneoplastic injection.[77] However, CED has demonstrated limited success in clinical trials due to irreproducible distribution of infusate,[78] poor infusate distribution to peripheral areas of diffuse gliomas, and an inability to accurately visualize the distribution of infused drug in real time. Multifunctional nanoscale materials are particularly well-suited to address these limitations by (i) providing endogenous imaging capabilities, (ii) allowing for control of size and surface properties, and (iii) facilitating facile addition of ligands to provide multivalent targeting of GBM.[77,79]

Preclinical research has shown promise in NP-facilitated CED to GBM with specific targeting against overexpressed surface receptors.[80–82] Our previous work indicated extensive distribution of CTX-labeled iron oxide NPs throughout tumors and surrounding tissue post-CED in a GBM xenograft model.[83] However, these observations were made ex vivo and therefore only at limited time points providing little insight on early time-dependent kinetics of CTX-mediated CED. Here, using real-time MRI, we investigate the role of the GBM-targeting ligand CTX with respect to dispersion of infusate in a CED system comprised of a superparamagnetic iron oxide NP core, a poly(ethylene glycol) (PEG) grafted chitosan surface coating (NPCP), and CTX (NPCP-CTX).

4.2 Materials and Methods

4.2.1 Materials

All reagents were purchased from Sigma Aldrich unless otherwise specified. CTX was purchased from the Fred Hutchinson Cancer Research Center (Seattle, WA). The heterobifunctional linker 2-iminothiolane (2IT) was purchased from Molecular Biosciences. NHS-PEG_{12}-maleimide [$SM(PEG)_{12}$] was purchased from Thermo Fisher Scientific. Tissue culture reagents including Dulbecco's Modified Eagle Medium (DMEM) and antibiotic–antimycotic were purchased from Invitrogen. Fetal bovine serum (FBS) was purchased from Atlanta Biologicals.

4.2.2 NPCP Synthesis

Iron oxide NPs coated with a copolymer of chitosan-grafted PEG were synthesized via a coprecipitation method as previously reported.[84] The synthesized NPCPs were purified using size-exclusion chromatography in S-200 resin (GE Healthcare) into 100 mM sodium bicarbonate buffer, pH 8.0, containing 5 mM ethylenediaminetetraacetic acid. A subset of NPCPs was set aside for Cy5 and/or CTX labeling while the remaining NPCPs were prepared for CED. For CED, NPCPs were further purified in phosphate buffered saline (PBS), concentrated using a Vivaspin 2 Centrifugal Concentrator (Vivaproducts) to 2 mg mL^{-1}, supplemented with 2.5% 600 MW PEG (w/w) and 2.5% dextrose (w/w), flash-frozen in liquid nitrogen, and stored at $-80^{\circ}C$ until used.

4.2.3 Cy5 and CTX Labeling of NPCP

NPCP (3.5 mg) in 100 mM sodium bicarbonate buffer, pH 8.0, was reacted with 1 mg of Cy5 (GE Healthcare) dissolved in dimethyl sulfoxide (10% v/v) for 1 h at room temperature, protected from light, and with gentle rocking. A 1 mg mL^{-1} solution of CTX was prepared in thiolation buffer and reacted with 2IT at a 1.2:1 molar ratio of 2IT:CTX for 1 h in the dark. Concurrently, NPCP and NPCP-Cy5 were reacted with $SM(PEG)_{12}$ at 216 μg of $SM(PEG)_{12}$ per mg of Fe in the dark with gentle rocking for 30 min. The $SM(PEG)_{12}$ modified NPCP/NPCP-Cy5 was then reacted with

CTX-2IT at 1 μg CTX per 4.5 μg Fe for 1 h in the dark to produce NPCP-CTX and NPCP-Cy5-CTX. NPs were purified using size-exclusion chromatography in S-200 resin equilibrated with PBS and stored at 4°C. For CED, NPCP-Cy5, NPCP-Cy5-CTX, and NPCP-CTX were concentrated using a Vivaspin 2 Centrifugal Concentrator to 2 mg mL^{-1}, supplemented with 2.5% 600 MW PEG (w/w) and 2.5% dextrose (w/w), flash-frozen in liquid nitrogen, and stored at −80°C until used.

4.2.4 NP Characterization

To measure the hydrodynamic size and zeta potential of NPs, the NPs (2 mg mL^{-1}, 2.5% w/w PEG and dextrose) were diluted to 100 μg mL^{-1} in 20 mM HEPES buffer (pH 7.4) and analyzed at 37°C using a DTS Zetasizer Nano (Malvern Instruments).

To quantify the degree of CTX attachment to NPs, NPCP-CTX was prepared as described above except that free CTX was not purified from the NPCP-CTX reaction mixture. Free, unreacted CTX was separated from the CTX conjugated to NPs through SDS-PAGE and quantified using the Quantity One software package and a standard curve of known concentrations of CTX. CTX conjugated to NPs was calculated by subtracting the amount of free CTX remaining in the reaction mixture from the total initial amount of CTX in the reaction.

A Capillary Viscometer (CANNON Instrument Company) was used to determine the viscosity of NPCP and NPCP-CTX solutions (NP concentration of 2 mg mL^{-1} with 2.5% w/w PEG and dextrose) with and without Cy5 fluorophore. A recirculating water bath (Thermo Fisher Scientific) was prepared at 40°C. The capillary viscometer was submerged in the water bath vertically with the water height 2 inches above the upper limit demarcation. The viscometer was equilibrated with the water bath for 15 min. A standard volume of 400 μL of sample was charged into the capillary viscometer by pipette, and the sample was equilibrated to 40°C over 5 min. Measurements were made following the manufacturer's protocol and values were normalized to saline.

Transmission electron microscopy (TEM) images were acquired with an FEI TECNAI F20 TEM operating at 200 kV. NP core diameters were analyzed with ImageJ software, and the size distribution, mean diameter, and s.d . were calculated from 100 NP measurements.

4.2.5 Animal Model

All procedures were performed in accordance with the University of Washington Institutional Animal Care and Use Committee guidelines and approvals. GBM6 cells were obtained from the Mayo Clinic and maintained as flank tumors in nude mice.[85] For intracranial implantation of GBM6 tumors, flank tumors were harvested, minced with a scalpel, then suspended into an equal volume of ice cold PBS (1 mL PBS per 1 g of tumor). Tumor cells were disaggregated by gentle pipetting, then filtered through a 40 μm filter and kept on ice at 10^7 cells mL^{-1}. Mice (nude athymic) were anesthetized with isoflurane and affixed to the base of a stereotaxic frame with ear bars. The skull was exposed through a 1-cm midline incision, then a burr hole was made 2 mm to the right of bregma and 1 mm posterior to the coronal suture using a Dremel tool equipped with a 1-mm tip. Using a Hamilton syringe attached to the stereotaxic frame, 2 μL of cells (20,000 cells) were injected over 1 min at a depth of 3 mm. After injection, the syringe was kept in place for 1 min prior to withdrawal and the incision closed with skin glue. Animals were monitored for tumor growth through Xenogen IVIS luminescent imaging. The same process outlined above was used to establish the syngeneic mouse model using C57Bl/6 mice and murine GL261 glioma cells.

4.2.6 Cranial Implantation of Cannula

Once tumors grew to approximately 30 mm^3 in size, an MRI-compatible cranial cannula (Plastics 1) was implanted to facilitate CED. Mice (nude athymic) were anesthetized with isoflurane and affixed to the base of a stereotaxic frame with ear bars. The skull was exposed through a 1-cm midline incision, then a burr hole was made 2 mm to the right of bregma and 1 mm posterior to the coronal suture using a Dremel tool equipped with a 1-mm tip. The MRI-compatible cranial cannula was then placed according to the manufacturer's instructions.

4.2.7 Administration of NPs

NPCP or NPCP-CTX was administered via cranial cannula to two randomized cohorts (NPCP = 4, NPCP-CTX = 5). NPs (3 μL) were infused at a rate of 1 μL min^{-1} using a Hamilton syringe.

4.2.8 Measurement of the MR Transverse Relaxation Rate of Aqueous NP Samples

All in vivo and in vitro MRI was performed using a Bruker Avance III 14 T (Ultrashield 600 WB Plus) vertical-bore imaging system. Serial concentration gradients of NPCP and NPCP-CTX were prepared via dilution of concentrated NP stock (2 mg mL^{-1} with 2.5% w/w PEG and dextrose) to concentrations of 0, 10, 50, 100, 150, and 200 µg Fe mL^{-1} in PBS. Glass vials (3.25 mm I. D., 5 mm O. D., 200 µL volume) were loaded with 150 µL of NPs. Sample tubes containing NPs were fixed in place inside a reservoir of PBS; this PBS reservoir served as a homogeneous background signal to minimize magnetic susceptibility variations near the samples. The secured vials were placed in a 25-mm single-channel ^{1}H radiofrequency receive coil (PB Micro 2.5) at 20°C. The transverse relaxation rates for NPCP and NPCP-CTX were evaluated using a quantitative T2 multi-spin multi-echo (MSME) pulse sequence with TR = 2,500 ms, TE $= 6.7 + 6n$ ms ($n = 0$–16), 52×78 µm^2 in-plane resolution, matrix 384×256, and 0.5 mm slice thickness for 14 slices.

4.2.9 In Vivo MRI

After anesthetization and cannula placement, mice were positioned in a 25-mm single-channel ^{1}H radiofrequency receive coil (PB Micro 2.5) centered on the head. During imaging, mice remained anesthetized with isoflurane (Piramal Healthcare) and secured in a coil-integrated Respiratory Monitoring System (SA Instruments; MRI-compatible small-animal monitoring and gating system) with nose-cone for oxygen/anesthetic, ear-bar head holder, circulating temperature control bath, and residual gas extraction. A 3D fast imaging with steady-state precession (FISP) scan sequence was performed (TR/TE $= 15/17.5$ ms, resolution $106 \times 108 \times 152$ µm^2, matrix $284 \times 186 \times 132$) to monitor cannula positioning. Prior to NP administration, a T2-weighted 2D rapid acquisition with refocused echoes (RARE) sequence (TR/TE $= 4,000/27.1$ ms, in-plane resolution 52×78 µm^2, matrix 384×256), and a 2D quantitative T2 (QT2) multi-spin multi-echo (MSME; TR $= 4,000$ ms, TE $= 6.7 + 6n$ ms, ($n = 0 - 16$), in-plane resolution 52×78 µm^2, matrix 384×256) sequence were acquired to form a suite of baseline imaging measurements to compare with post-CED imaging. After NP administration, the same T2-weighted, T2*-weighted, and QT2

scan sequences were serially acquired in an interleaved fashion immediately after CED and at 20 min, 1 h, 4 h, 12 h, and 48 h for a single animal. For a statistical comparison of V_D between mice receiving CED of NPCP ($n = 4$) to mice receiving CED of NPCP-CTX ($n = 5$), the same interleaved imaging suite was acquired prior to CED and at 12 h and 24 h post-CED. Total imaging time for each scan sequence was approximately 4 min. Slices for sequential scans were prescribed identically between time points by registering the 14 transverse, 0.5-mm thick slices to extend from the notch formed between the olfactory bulb and the cerebral cortex until the anterior cerebellum.

4.2.10 MRI Data Analysis

Analysis of MRI data was performed using the FMRIB software library (FSL),[56] Bruker Paravision 5.1 analytic package, and Osirix (Pixmeo). Processing stages for in vitro QT2 data included (i) region of interest (ROI) definition as a circular 100-voxel area residing within a sample cross-section, (ii) automated mean T2 value and s. d. calculation from within the 100-voxel ROI (using the Paravision 5.1 software package), and (iii) calculation of the transverse relaxation rate as the slope of the plot of R2 (computed as $1/T2$ using FSL) versus Fe concentration determined through computation of the best-fit line via least-squares linear regression.

Visualization of the V_D of NPs administered via CED was achieved by applying threshold color maps to the 2D transverse T2-weighted images of mice for each of the NPCP and NPCP-CTX cohorts at different time points. T2-weighted signal intensity was normalized in each image to the signal amplitude of a water phantom placed adjacent to the skull of the animal during imaging to correct for temporal fluctuations in hardware sensitivity and scan-to-scan differences in pulse power/receiver gain settings. Only voxels with a percent signal change greater than the applied threshold value (e.g., 10% or 15%) relative to pre-CED images were colored.

Similarly, the V_D values of NPCP and NPCP-CTX were calculated by applying a 15% threshold to T2-weighted signal changes referred to pre-CED images after signal normalization. The volume of the voxels composing the subset of voxels representing a 15% signal change or greater was computed as the V_D for each animal at the 12-h and 24-h time points. The mean and s. d. for the V_D of each cohort ($n = 4$ for NPCP and $n = 5$ for NPCP-CTX) were determined for both 12-h and

24-h time points. A Student's t-test was used to determine statistically significant differences in V_D between cohorts and time points. V_D for the single mouse imaged at 20 min, 1 h, 4 h, 12 h, and 48 h post-CED was determined as above, and error was determined by computing the V_D at each time point with thresholds of 10% and 20% instead of 15%.

QT2 images were used to determine the extent of CED over time by plotting the measured T2 values within 5 specified ROIs in tumor tissue and healthy brain for a single mouse receiving CED of NPCP-CTX or NPCP. ROIs were defined as 50-voxel squares and were prescribed in precisely the same location within the brain across all time points. The represented T2 values are displayed as the mean and s. d. of the T2 value of the 50-voxel ROI.

4.2.11 Flow Cytometry Analysis

Twenty-four h after NP administration, animals were euthanized and tumors were isolated and placed in ice cold PBS. Tumors were sectioned and tumor cells were disassociated and passed through a 70 μm cell strainer (Thermo Fisher Scientific) to acquire a single-cell suspension. Cells were then subjected to staining with GBM stem cell marker anti-CD44-PE (Abcam) following the manufacturer's protocol and analyzed using a BD FACSCanto Flow Cytometer (Beckton Dickinson). Data analyses were performed using the FlowJo software package (Tree Star).

4.2.12 Histologic Analysis

Whole brains were removed through necropsy 48 h post-CED of NPs and preserved in 10% formalin for 48 h. Whole brains were then embedded in paraffin wax, sliced into 5 μm thick sections, and stained with hematoxylin and eosin (H&E) or Prussian blue/Nuclear fast red using standard clinical laboratory protocols. Microscopic images of brains were acquired using an E600 Upright Microscope (Nikon) equipped with a CCD color camera. Additional preserved brains were provided to the University of Washington Pathology Research Services Laboratory to acquire electron micrographs.

4.3 Results

NPCPs were synthesized via coprecipitation of iron chlorides utilizing a chitosan-PEG polymer as described previously.[84] NPCP-CTX was produced by immobilization of CTX on the polymer surface of NPCP through a thioether bond, to provide GBM-targeting specificity. Table 4.1 summarizes the key physicochemical properties of NPCP and NPCP-CTX. The amount of CTX conjugated to NPCP, quantitated using a gel electrophoresis assay, was 17 ± 3 CTX molecules per NP. The hydrodynamic size of NPCP and NPCP-CTX were 55 ± 3 and 54 ± 2 nm, respectively, and zeta potentials were 2.18 ± 6.6 and 1.04 ± 8.5 mV, respectively (Figure 4.1a and b). The hydrodynamic size and zeta potential of NPCP and NPCP-CTX were comparable and well within the limits for optimal CED.[77] Viscosities of NPCP and NPCP-CTX, with and without Cy5 fluorophore, were measured using a capillary viscometer to ensure viscosity differences between NP constructs were not responsible for any observable differences in V_D. Viscometry measurements showed no significant difference between NPs, with saline normalized values ranging from 1.18 to 1.25 (Figure 4.1c). The transverse MRI relaxivity (r_2) for NPCP and NPCP-CTX determined at a field strength of 14 T were comparable at 40.0 ± 0.8 and 40.3 ± 1.0 s^{-1} mM^{-1}, respectively (Figure 4.1d), indicating the addition of CTX does not appreciably affect transverse MRI relaxation properties of NPCP. Figure 4.1e shows the TEM images of NPCP and NPCP-CTX. The diameter of the NP iron oxide core was measured to be 7.0 ± 1.4 nm.

Table 4.1: Primary physicochemical properties of NPCP and NPCP-CTX

Infusate	CTX molecules per NP	Hydrodynamic size (nm)	Zeta potential (mV)	Viscosity $\left(\frac{Pa \cdot s_{exp}}{Pa \cdot s_{saline}}\right)$	Transverse relaxivity $\left(\frac{1}{s \cdot mM}\right)$	Core size (nm)
NPCP	0	55 ± 3	2.18 ± 6.6	1.25 ± 0.05	40.0 ± 0.8	7.0 ± 1.4
NPCP-CTX	17 ± 3	54 ± 2	1.04 ± 8.5	1.22 ± 0.09	40.3 ± 1.0	7.0 ± 1.4

Intracranial GBM6 xenografts were established in nude athymic mice to evaluate the effects of CTX modification of NP on V_D during CED. GBM6 is a clinically relevant human primary tumor that is maintained by serial subcutaneous tumor passage, thereby sustaining key molecular and morphologic phenotype of the human primary tumor.[86] Tumor growth was monitored by Xenogen

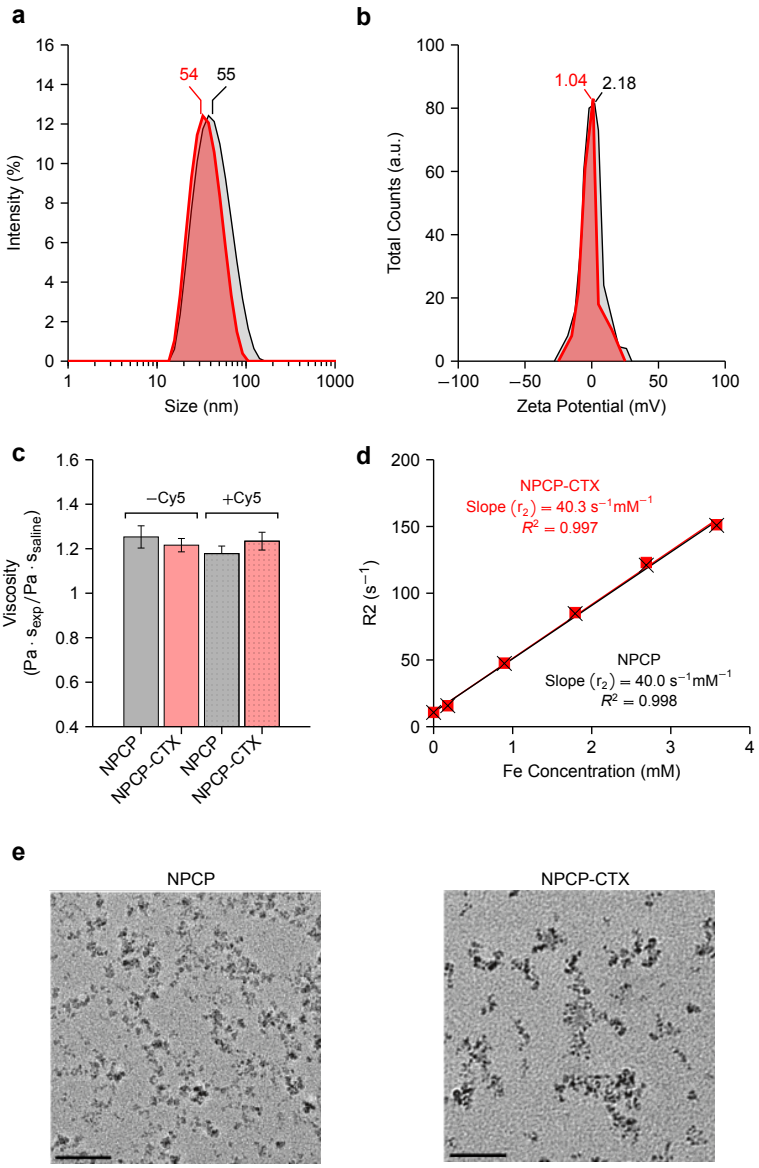

Figure 4.1: Physicochemical properties of NPCP and NPCP-CTX. (a) Hydrodynamic size distribution of NPCP (gray) and NPCP-CTX (red). (b) Zeta potential of NPCP (gray) and NPCP-CTX (red). (c) Viscosity comparison of NPCP and NPCP-CTX with and without Cy5 fluorophore conjugated and normalized to the viscosity of saline. (d) Transverse MRI relaxation rate, R2, of NPCP ($\times$, gray), and NPCP-CTX (■, red) measured as a function of iron concentration at a field strength of 14 T. The slopes of the lines represent the transverse relaxivity (r_2) and were calculated to be 40.0 and 40.3 s^{-1} mM^{-1} for NPCP and NPCP-CTX, respectively. (e) TEM images of NPCP (left) and NPCP-CTX (right); scale bars = 50 nm.

IVIS luminescent imaging, and once tumors were established, cannulas were placed through a burr hole made 2 mm to the right of the bregma and 1 mm posterior to the coronal suture to center the cannula within the tumor. Figure 4.2a schematically depicts the experimental CED configuration using a 14 T MRI system. Surface reconstruction of a 3D FISP scan sequence demonstrates cannula entry and approximate location (Figure 4.2b). A T2-weighted 2D coronal slice indicates the exact location of the cannula denoted by a red box around the ROI (Figure 4.2c). The ROI in Figure 4.2c is shown in an expanded view to provide more accurate cannula dimensions (Figure 4.2d).

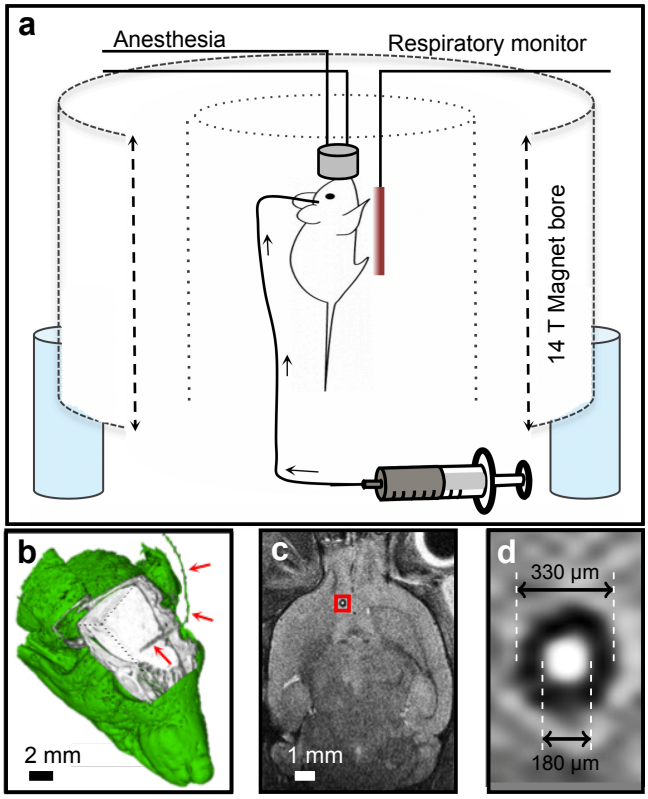

Figure 4.2: Experimental design for real-time monitoring of CED. (a) Schematic illustration of in vivo MRI using a 14 T field strength vertical bore MRI system, animal monitoring system, and intracranial cannula. (b) Surface reconstruction of a cranial 3D FISP scan sequence demonstrating the cannula location (arrows, cannula). (c) A coronal slice demonstrates dimensions and approximate implant location. The ROI (marked with a red frame) in (c) is enlarged and shown in (d).

NPs were delivered (3 μL volume at a rate of 1 μL min^{-1}) to each mouse by a CED process with the animal positioned within the magnet to facilitate serial imaging post-CED. Interleaved T2-weighted, T2*-weighted, and QT2 imaging were performed before and immediately after CED and at 20 min, 1 h, 4 h, 12 h, and 48 h post-CED in a representative animal for NPCP and NPCP-CTX. Additional animals were imaged pre-CED of NPs and at 12 h and 24 h after NPCP ($n = 4$) or NPCP-CTX ($n = 5$) administration to provide a statistical comparison of V_D between CTX-targeted and nontargeted NPs. Figure 4.3a and b display T2-weighted signal change at 0 h (immediately post-CED) and 48 h after CED in 7 adjacent image slices in the transverse plane encompassing the tumor region of animals administered (i) NPCP or (ii) NPCP-CTX. The blue color map denotes % T2-weighted signal change of voxels within the brain at 0 h, and the red color map denotes % T2-weighted signal change at 48 h corresponding to increased NP concentration. These images show a substantially greater V_D for CTX-enabled NPs throughout the tumor space compared with nontargeted NPs at 48 h. Highly sensitive T2*-weighted transverse images of slices centered on the cannula insertion tracts of NPCP- (Figure 4.3c) and NPCP-CTX- (Figure 4.3d) treated animals were used to detect low concentrations of NP at the periphery of the expanding V_D over time from preinjection to 48 h postinjection. Iron oxide NP provides negative contrast enhancement; therefore, a voxel containing NP will appear darker in the MR image. The distribution of NPCP-CTX continued to increase to 48 h and broadly covered the tumor, but NPCP receded by 48 h within the transverse plane.

V_D of NPCP and NPCP-CTX at 12 h and 24 h was calculated by identifying all voxels within 2D transverse slices that passed a 15% threshold of the maximum signal change at 12 h and 24 h, respectively (Figure 4.3e). V_D of NPCP at 12 h was 58 ± 22 mm^3 and receded to 36 ± 16 mm^3 at 24 h, while V_D of NPCP-CTX at 12 h was 96 ± 37 mm^3 and increased to 121 ± 39 mm^3 at 24 h, indicating a significant difference in V_D between NPCP and NPCP-CTX at 24 h ($p < 0.002$). The ratio of V_D to infused volume (V_D:IV) for NPCP-CTX at 12 and 24 h was 32:1 and 40:1, respectively, which is a 3.4-fold increase compared with NPCP at 24 h. The V_D for NPCP and NPCP-CTX were further evaluated using a syngeneic glioma model comprised of C57Bl/6 mice implanted intracranially with mouse GL261 glioma cells, which have been shown to be targeted

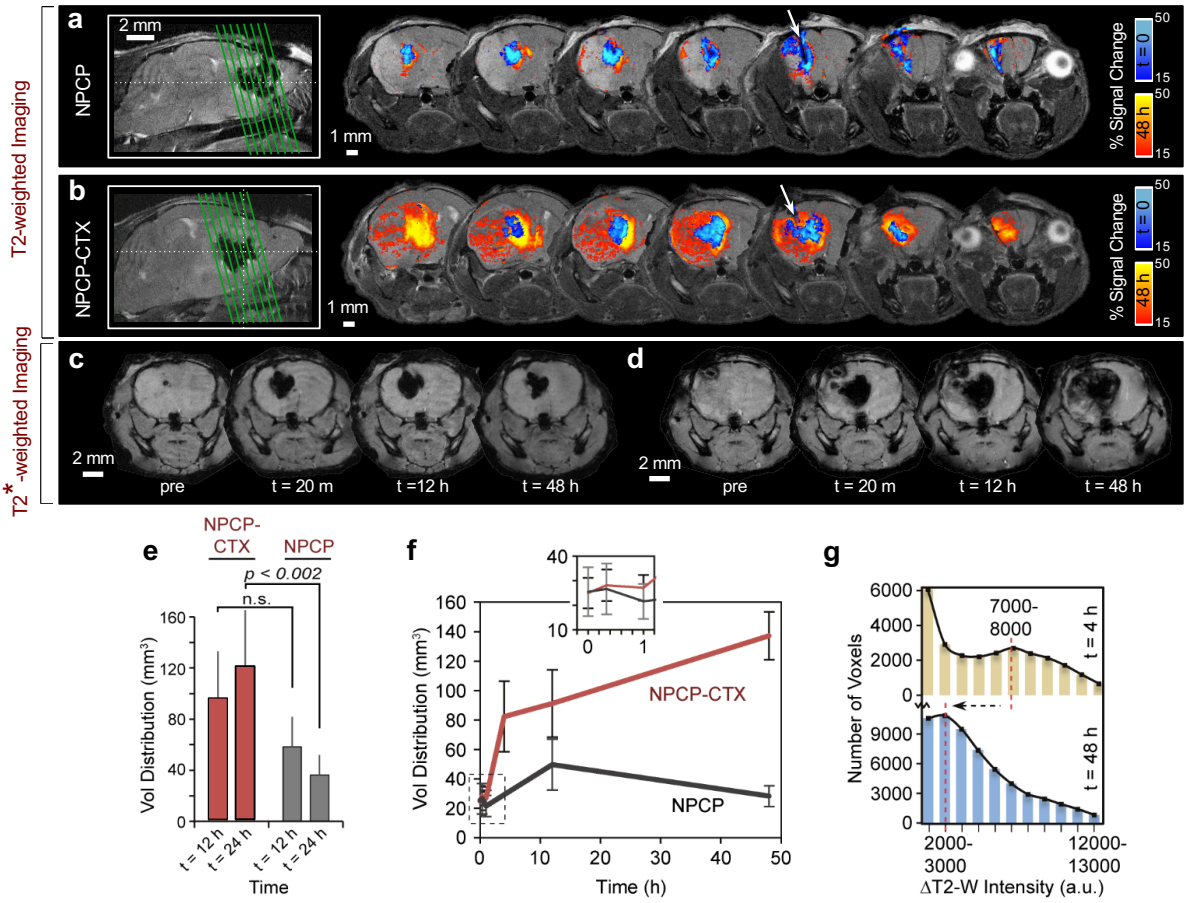

Figure 4.3: T2-weighted and T2*-weighted MRI for determination of V_D. Representative T2-weighted transverse images from 7 adjacent slices through the tumor region for (a) NPCP- and (b) NPCP-CTX-treated mice. The green lines in the sagittal images on the left side indicate the locations of the 7 transverse slices, and the white arrows indicate cannula insertion tracts. Highly sensitive T2*-weighted images of (c) NPCP- and (d) NPCP-CTX-treated mice acquired pre- and post-CED. (e) V_D comparison for NPCP-CTX- (red) and NPCP- (black) treated mice. Error bars represent s. d. from 3D volume determination in multiple mice for NPCP-CTX ($n = 5$) and NPCP ($n = 4$). (f) 3D V_D for NPCP-CTX (red) and NPCP (black) as a function of time from an individual mouse elucidating early time point differences in V_D. Error bars were determined by recalculation of V_D with $\pm 5\%$ change in threshold parameters ($10\% - 20\%$). The inset at the top of the graph shows an expanded view of the ROI marked by the dashed box. (g) Histogram of all voxels passing a 15% threshold at $t = 4$ h (tan) and $t = 48$ h (blue) for NPCP-CTX. The relative shift from a small local maximum at 7,000−8,000 ($t = 4$ h) to a peak at 3,000−4,000 ($t = 48$ h) indicates a transition from a relatively low volume (number of voxels), high concentration NP distribution to a relatively high volume, low concentration NP distribution, confirming progressive dispersion of NPCP-CTX over 48 h.

by CTX.[87] Figure 4.3f shows the V_D calculated from a single animal both for NPCP and NPCP-CTX with closely spaced early time points. NPCP-CTX V_D increased dramatically from 1 h to 4 h followed by a less dramatic, but continued progression in V_D to 48 h. NPCP V_D, in contrast, increased from 1 h reaching a maximum at 12 h before diminishing. To evaluate the variability in NPCP-CTX concentration within the V_D, change in T2-weighted intensity between pre-CED and 4 h or 48 h post-CED (ΔT2-weighted) was determined. Changes in T2-weighted intensity correlates to NP concentration and was used to produce a histogram of all voxels passing the 15% threshold at 4 h and 48 h for NPCP-CTX (Figure 4.3g). The relative shift from a small local maximum at 7,000$-$8,000 of ΔT2-weighted intensity to a peak at 2,000$-$3,000 of ΔT2-weighted intensity from 4 h to 48 h indicates NPCP-CTX dispersion from a relatively high concentration in a small volume (number of voxels) to a relatively low concentration spread over a greater volume (number of voxels).

Figure 4.4a provides a detailed look at positive (blue) and negative (green) signal change over specified time intervals in T2-weighted transverse images from two adjacent slices centered around the cannula insertion tract. The two slices presented for each time span were chosen as representative images of the entire tumor space. Signal changes are defined as the signal intensity at the end of a time period minus the signal intensity at the beginning of the same time period. A negative contrast change (i.e., the initial signal intensity is greater than the ending signal intensity of a time period), which indicates increased NP concentration, is highlighted by the green color map while a positive contrast change (i.e., the initial signal intensity is smaller than the ending signal intensity of a time period), indicating a reduction in NP concentration, is highlighted by the blue color map. The color maps indicate the percent change in T2-weighted signal between the time intervals specified above each pair of transverse slice images. NPCP-CTX displays modest dispersion over the first 60 min post-CED, followed by significant dispersion from 60 min to 4 h and 12 h to 48 h, indicating a complex dispersion/absorption process (left, Figure 4.4a). Between 4 and 12 h, positive contrast changes were primarily observed in the central region of the tumor, indicating a reduction in NPCP-CTX concentration. In comparison, a minimal change in NPCP dispersion is observed over the entire 48 h of post-CED monitoring (right, Figure 4.4a).

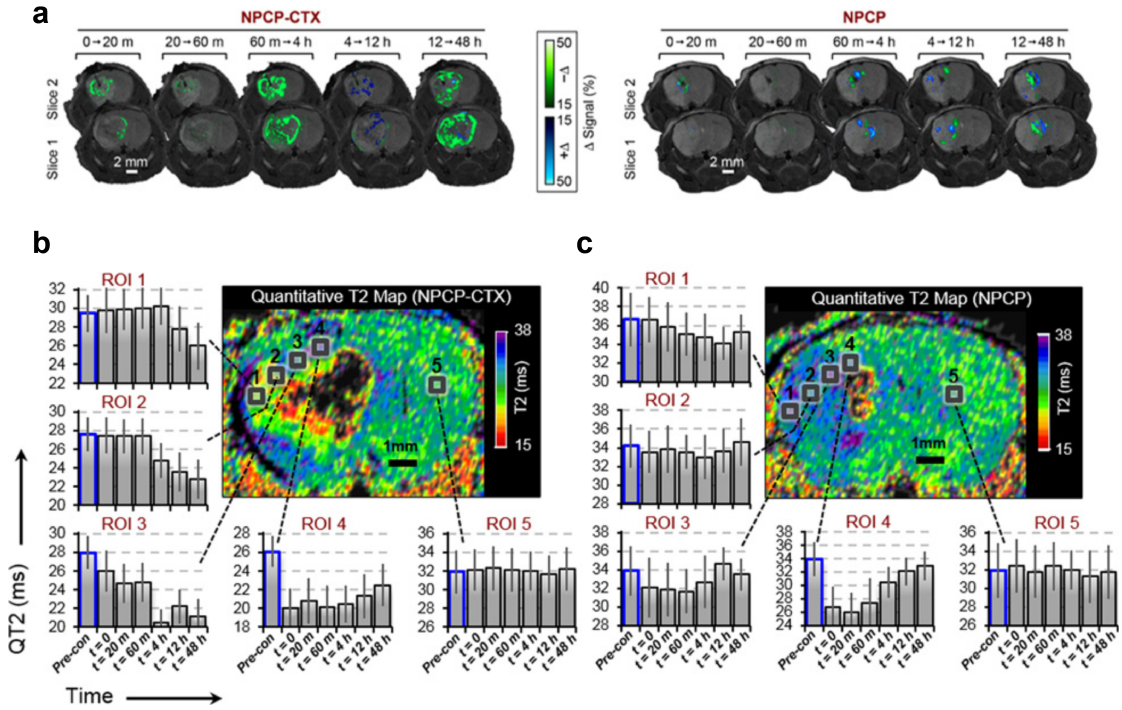

Figure 4.4: NP distribution as a function of time. (a) Change in T2-weighted signal over the specified time periods of two adjacent slices for NPCP-CTX (left) and NPCP (right) delineating the loss of NP contrast (blue color map, $+\Delta$) and increase in NP contrast (green color map, $-\Delta$). Time-dependent QT2 signal variations for 5 ROIs within tumor from the periphery to the injection site (ROIs $1-4$) and in healthy brain (ROI 5) for (b) NPCP-CTX- and (c) NPCP-treated mice.

QT2 imaging was used to quantitate the time-dependent distributions of NP throughout the tumor (Figure 4.4b and c) from preadministration to 48 h post-CED. To avoid quantitation issues associated with NP saturation and corresponding signal loss, ROIs were selected where complete loss of signal due to NP saturation had not occurred. For example, ROIs 3 and 4 approach the point source of the NP infusion, but do not fall within the narrow region surrounding the point source that contains the highest NP concentration and attendant complete loss of signal. For NPCP-CTX, regions close to the cannula tip (ROIs 4 and 3) show an immediate reduction in QT2 signal (i.e., increased NP accumulation) with ROI 4 displaying a drastic reduction in QT2 signal followed by a modest signal increase as NPs gradually disperse to outer regions of the tumor over time (Figure 4.4b). ROIs 2 and 1, near the periphery of the tumor, display no reduction in QT2 signal until 4 h and 12 h, respectively. By 48 h, NPCP-CTX is dispersed relatively evenly throughout

the tumor mass as indicated by similar reductions in QT2 signal for ROIs $1-4$ as compared with baseline signal (bars outlined in blue). ROI 5, located within healthy brain tissue, shows no change in signal over the 48-h period. The QT2 map of the nontargeted NPCP-treated animal shows a reduction in QT2 signal immediately after CED near the cannula tip (ROIs 3 and 4); however, the initial drop in QT2 signal is transient and returned to near baseline within hours (Figure 4.4c). The QT2 signal change for ROIs 1 and 2 on the periphery of the tumor show no significant change, indicating minimal dispersion of NPCP to the periphery of the tumor.

The specificity of NPs towards GBM was evaluated by flow cytometry analysis of immunofluorescence CD44 staining of tumors treated with NPCP-Cy5 or NPCP-Cy5-CTX (Figure 4.5). CD44 is a well-studied marker for GBM and its elevated expression correlates with more severe tumor types.[86] Twenty-four h post-CED of NPs, tumors were excised, disassociated, and passed through a 70 μm cell strainer to acquire single-cell suspensions, followed by staining with anti-CD44-PE. A representative scatter plot assessing PE and Cy5 fluorescence intensity is shown in Figure 4.5a. A significant increase in PE fluorescent signal for a large fraction of tumor cells stained with anti–CD44-PE confirmed the cells are of GBM origin (Figure 4.5b). The percentage of cells staining positive for CD44 were $84.9 \pm 6.5\%$, $74.7 \pm 9.4\%$, and $81.9 \pm 10.5\%$ for untreated mice, mice treated with NPCP-Cy5, or NPCP-Cy5-CTX, respectively. A comparison of Cy5 mean fluorescence intensity for samples treated with NPCP-Cy5 to untreated samples indicate a small number of GBM cells positive for the nontargeted NPs (Figure 4.5c). Comparatively, tumors treated with NPCP-Cy5-CTX show a large population shift in Cy5 signal intensity, indicating specific targeting of CTX-labeled NP to GBM6 tumor cells.

NPCP and NPCP-CTX cellular localization was examined by histologic evaluation of brain tissue sections including the tumor body, tumor margin, and healthy brain (Figure 4.6a and b). Forty-eight h after CED, brains were fixed (10% formalin), embedded in paraffin, and sectioned. H&E staining revealed the margins between healthy brain and tumor tissue, and indicated that NPCP and NPCP-CTX caused no acute toxicity to brain or tumor tissue. Prussian blue staining provided visualization of NP localization. NPCP (Figure 4.6a) that appears in the Prussian blue–stained sections is observed in the primary tumor body but not at the tumor margin. NPCP-CTX (Figure 4.6b),

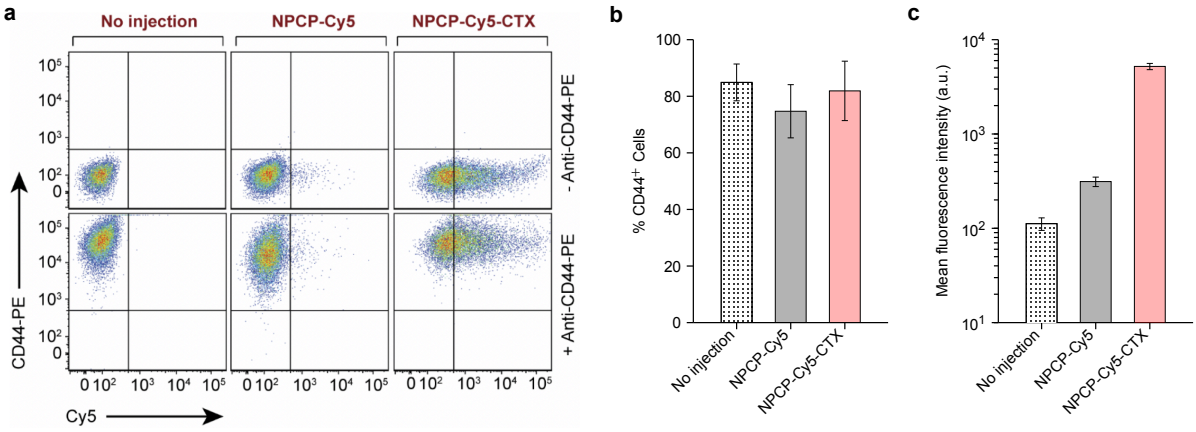

Figure 4.5: Flow cytometry analysis of NPCP-Cy5-CTX specificity to GBM. (a) Representative scatter plots of excised tumor tissue from untreated mice and mice administered NPCP-Cy5 and NPCP-Cy5-CTX stained with anti-CD44-PE. (b) Percent of cells stained positive for CD44 indicating GBM origin. (c) Mean fluorescence intensity of Cy5 signal for samples collected from untreated mice and mice administered NPCP-Cy5 and NPCP-Cy5-CTX, indicating a significant increase in Cy5 signal for NPCP-Cy5-CTX. Error bars, s. d. with $n = 3$ mice per treatment.

however, is observed in both the tumor body and tumor margin, but not in healthy tissue at 48 h. Tissue sections from mice administered with NPCP-CTX were analyzed by TEM to evaluate intracellular localization of NPs (Figure 4.6c and d). NPCP-CTX was present, appearing as black dots, in vasculature cross-sections in both endothelial cells (EC) and red blood cells (RBC; Figure 4.6c), and were found to be intimately associated with chromatin in GBM tumor cells (Figure 4.6d).

4.4 Discussion

Tissue heterogeneity influences bulk fluid flow in the extracellular space of the brain parenchyma and has a significant effect on distributions of infused agents.[88] The presence of a GBM tumor can further exacerbate tissue heterogeneity and necessitates the direct visualization of infused agents for optimization of CED. A common approach in CED studies is the use of surrogate-imaging tracers that are coinfused with therapeutic agents.[89] However, distributions of tracers can be affected by the delivery system, target tissue, and molecular properties of the infused agents, resulting in inaccurate and unreliable evaluation of distributions when monitoring CED.[90] NPs with imaging

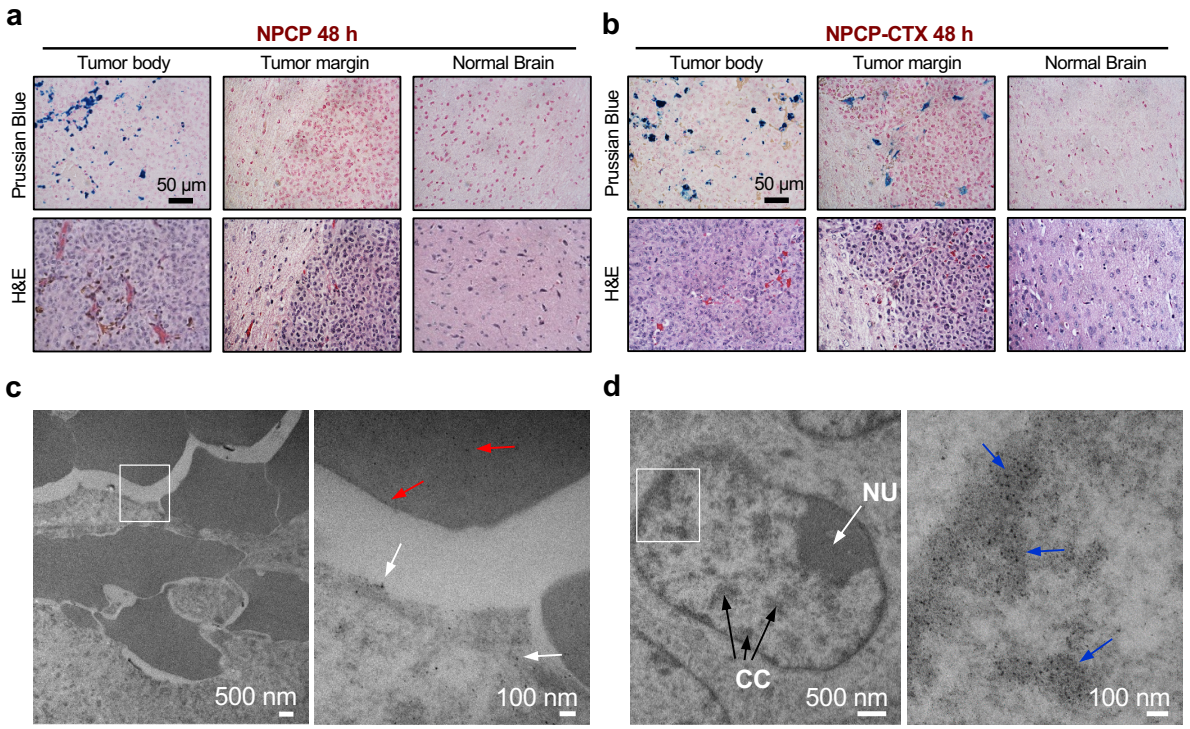

Figure 4.6: Histologic evaluation of NP localization. Prussian blue (top row) and H&E-stained (bottom row) slices of mouse brain 48 h after CED of (a) NPCP and (b) NPCP-CTX. H&E staining provides clear delineation of the tumor margin. Prussian blue staining indicates the location of NPs (blue stain). (c) TEM image of an intratumoral vessel cross-section denoting RBCs and ECs with an ROI (marked with a white frame, left image) showing NPCP-CTX in ECs (white arrows) and RBCs (red arrows) in the expanded view (right). (d) TEM images of a GBM cell nucleus denoting nucleolus (NU, white arrow) and condensed chromatin (CC, black arrows) with an ROI (marked by a white frame, left) showing NPCP-CTX localized to chromatin (blue arrows) in the expanded view (right).

contrast capability can be used to deliver therapeutics while being visualized by an associated imaging modality, eliminating the need for surrogate imaging tracers and improving evaluation of time-dependent distribution of infusate. The base NP platform used in this work served only as a contrast agent, but we have previously extended this platform to combine its MRI capabilities with therapeutic functionality.[91,92] In this study, we utilized iron oxide NPs that are superparamagnetic and serve as a contrast agent for MRI to facilitate real-time imaging of the CED process. Iron oxide NPs are biodegradable and biocompatible and have been used clinically to provide T2 contrast in MRI, and many therapeutic formulations of iron oxide NPs are currently under preclinical evalua-

tion.[11,93] NP diffusion through brain parenchyma is effected by several physicochemical properties including hydrodynamic size, zeta potential, and viscosity.[77] The hydrodynamic size (∼55 nm) and zeta potential (near neutral) of the NPs utilized in this study were optimal for mitigating NP interactions with the extracellular matrix to minimize NP retention at the injection site and maximize V_D.[77] Several studies have shown that increased viscosity of infusate provides greater V_D by minimizing infusate backflow and increasing pressure at slow infusion rates.[94,95] Because of concerns that differences in viscosity would inhibit direct comparison between NP constructs, all NPs were supplemented with 2.5% 600 MW PEG (w/w) and 2.5% dextrose (w/w) to normalize viscosity of infused solutions. In addition to hydrodynamic size, zeta potential, and viscosity, the MRI relaxivity of NPCP and NPCP-CTX were nearly identical allowing NPCP to serve as an excellent control NP to evaluate the effects of CTX modification.

The MRI evaluation of V_D demonstrated that NPCP-CTX produced a 3.4-fold increase in V_D over NPCP and greater than a 10-fold increase in V_D:IV over values typically reported for NPs or NP-sized infusates (25–110 nm) under similar conditions.[74,80,81,96–99] Reported values of V_D:IV of NP and NP-sized infusate such as viral vectors are generally 2 to 3-fold less than those reported for small molecules due to size limitations in the extracellular space of the brain. However, NPCP-CTX demonstrated a V_D:IV more than 4-fold greater than previously reported values for small molecules.[100–102] The combined results from MRI evaluation show that NPCP behaved as a typical infusate administered by CED where infusates are dispersed during infusion as positive pressure gradients facilitate convection, followed by minimal diffusion and clearance. Conversely, NPCP-CTX displays behavior that cannot be driven by CED alone. The dramatic increase in V_D and the complex time-dependent absorption/dispersion profile observed in Figure 4.4a post-CED when convective forces are absent suggest that CTX facilitates increased diffusion and/or active transport in addition to the convective forces of CED. The presence of NPCP-CTX in ECs and RBCs further supports a mechanism other than simple bulk diffusion or convection in the parenchyma. It should be noted that the atypical behavior of NPCP-CTX would not have been observed if coinfused imaging tracers were employed because imaging tracers lacking CTX functionality behave as typical infusates and their distribution is driven solely by the convective forces of CED and diffu-

sion. These findings highlight the primary advantage of using infusates with endogenous imaging capabilities.

Overexpressed matrix metalloproteinase-2 (MMP-2) and Annexin A2 cell surface receptors have been implicated as CTX targets in a range of cancers.[103,104] Annexin A2 is reported to play a role in the ability of CTX to bind and internalize in noncancerous proliferating human vasculature ECs providing a potential mechanism for NPCP-CTX to move from the brain parenchyma into tumor vasculature, facilitating the dispersion of NPCP-CTX through the tumor mass. Recent evidence for the existence of a cerebral venous lymphatic system provides a potential alternate (or complementary) mechanism for the broad distributions observed in CED of NPCP-CTX.[105,106] CTX is a peptide toxin found in the venom of the death stalker scorpion (*Leiurus quinquestriatus*). Studies have shown that toxins can be absorbed through the lymphatics.[107] Toxins absorbed in the lymph pool act as a depository providing sustained release of toxin back into the blood stream yielding a complex absorption process.[108]

The chitosan-PEG polymer shell likely contributes significantly to the localization of NPCP-CTX to the nuclei of GBM cells. Chitosan, a biocompatible natural polymer, and its derivatives have been used to condense and deliver DNA in gene therapy applications,[109] and chitosan NPs have been reported to localize to nuclei of fibroblast cells.[110] Nuclear localization of chitosan is likely due to the abundant amines along the chitosan backbone that facilitate electrostatic interaction with the negatively charged DNA phosphate backbone. These interactions have significant implications in GBM chemo-, radio-, and gene-therapy. Nuclear localization of therapeutics administered via CED would facilitate increased efficacy of chemotherapeutics that damage DNA or inhibit DNA repair pathways as their main mechanism for cell death. The efficacy of iron oxide NPs as radiosensitizers may be improved by maximizing their effects on nuclei, and in gene therapy applications the extensive nuclear localization of NPCP-CTX could facilitate improved gene expression.

4.5 Conclusions

In summary, time-resolved MRI was utilized to investigate the kinetics of CED processes of both targeted (NPCP-CTX) and nontargeted (NPCP) iron oxide NPs with CTX as a targeting ligand. T2 contrast provided by the iron oxide core facilitated real-time MRI evaluation of infusate distribution. NPCP-CTX showed a 3.4-fold increase in V_D 24 h post-CED over NPCP, a 10-fold increase over previously reported V_D in similar systems, and exhibited sustained expansion within tumor volumes over the observed 48 h. The significant expansion in NPCP-CTX V_D suggests the action of a possible active transport mechanism in addition to CED, which was further supported by localization of NP in ECs and RBCs. NPCP-CTX targeting was shown to be specific to GBM cells and the NPs preferentially localized in nuclei where they associated with chromatin. The ability of CTX-functionalized NPs administered via CED to broadly cover GBM tumors, localize to nuclei, and provide means for real-time monitoring of infusate distribution has significant implications for GBM treatment. These results warrant continued investigation to fully realize the potential of CTX-mediated CED applications in a range of nanomedicine-based delivery platforms.

Chapter 5

IRON OXIDE NANOPARTICLE-MEDIATED RADIOENHANCEMENT IN GLIOBLASTOMA

Radiotherapy is a major component comprising the standard of care in cancer treatment. Notwithstanding the promising therapeutic efficacy of radiotherapy, improvements such as increasing the probability of eliminating a maximum amount of cancerous tissue and minimizing off-target destruction may prove to be supremely effective in ameliorating the prognosis of cancers. Here we report on the enhancement of radiotherapy mediated by iron oxide nanoparticles (NPs) as demonstrated in mice using a glioma tumor model, which is a form of cancer that exhibits an especially recalcitrant response to radiotherapy. Iron oxide core NPs were coated with different polymers and exposed to ionizing radiation in the form of γ-rays; the resultant formation of reactive oxygen species (ROS) was then measured to determine which NP formulation had the greatest potential for enhancing radiotherapy, as ROS are known to cause damage to vital cell structures and DNA. The most promising NP consisted of an iron oxide core coated with a biocompatible chitosan-polyethylene glycol (PEG) copolymer. This NP was further modified through covalent bonding of chlorotoxin (CTX), a tumor-targeting peptide, to increase the ability of the NP to cross the blood-brain barrier (BBB) and infiltrate the tumor site. In vivo studies of mice bearing orthotopic human primary glioblastoma (GBM) xenografts demonstrated that γ-ray irradiation treatment accompanied by intravenous NP administration significantly reduced tumor growth rate and increased overall survival time compared to sole treatment with either γ-ray radiotherapy or NP injection. These studies show that iron oxide NPs act as radiosensitizers that could improve treatment outcomes and warrant further investigation into their applicability in radiotherapy.

5.1 Introduction

Along with surgical resection and chemotherapy, the application of ionizing radiation is an essential part of the treatment arsenal in the fight against oncological disease, as more than half of all patients with cancer undergo radiotherapy.[111,112] However, radiotherapy has attendant drawbacks, such as its toxicity to healthy tissue; furthermore, not all forms of cancer have the same response to high-energy irradiation. In particular, large, late-stage tumors and GBMs are characteristically resistant to radiotherapy.[113–115] Given its widespread use, efforts to increase the efficacy of radiotherapy by reducing off-target toxicity while enhancing tumor cell killing ability would be highly advantageous towards improving clinical results in cancer therapy.

The prospect of using materials composed of atoms with high atomic numbers (Z) to enhance the effect of the radiation dose applied during radiotherapy has been under study for decades.[116] Compared to the soft tissue of the body, the energy absorption coefficients of high-Z atoms are much greater (e.g., iron, iodine, and gold). Thus, upon exposure to ionizing radiation, electron-dense atoms are much more likely to absorb photons, initiating a cascade of events that ultimately results in the ejection of inner shell electrons (i.e., the photoelectric effect or Auger emission) followed by the creation of ROS, which in turn cause damage to DNA and cellular structures in their immediate vicinity (Figure 5.1a).[117,118] Recently, metal NPs have been exploited for their large energy absorption coefficients for application as radiosensitizers in so-called NP-mediated deposition of radiation (NMDR). NPs with components including silver,[119,120] gadolinium,[121,122] and hafnium[123] have demonstrated their ability to serve as radiosensitizers, but by far the most used materials in this regard have been gold NPs.[124]

Despite the relatively large pool of research supporting the efficacy of gold NPs and other heavy metal NP formulations as radiosensitizers, there has been scant investigation into the similar use of iron oxide NPs. One publication focused on in vitro studies using iron oxide NPs as radiosensitizers,[125] and another used both iron oxide NPs and gold NPs to assess their ability for radiosensitization in murine colon carcinoma located in the flank.[126] NP formulations based on iron oxides are attractive due to their biodegradability and inherent superparamagnetism which

enables contrast enhancement in magnetic resonance imaging (MRI). Furthermore, several iron oxide NPs have been approved by the United States Food and Drug Administration (FDA) for clinical use (e.g., Resovist, Ferrisat, Venofer, Feraheme, and others), whereas gold NPs have not moved beyond clinical trials.[127] We envision that iron oxide NPs may be fast-tracked into clinical use as radiosensitizers based on their pre-existing FDA approval and significant ability to promote radioenhancement.

Here, we report on the preclinical evaluation of the use of iron oxide NPs as radiosensitizers. We investigated different iron oxide NP formulations for their potential to generate ROS upon exposure to γ-irradiation. The best performing NP was chosen for further use in both cellular and animal models. In vitro cell killing efficiency was demonstrated to be substantially increased in cells incubated with NPs and irradiated with γ-rays compared to cells receiving only γ-irradiation. MRI was used to monitor tumor progression in mice bearing human orthotopic primary GBM xenograft tumors. Mice treated with both NPs and a 10 Gy γ-irradiation dose showed a 2-fold increase in median survival time as well as a 3-fold decrease in tumor growth rate compared to mice receiving radiotherapy only. This study indicates that iron oxide NPs are viable candidates to serve as radiosensitizers, offering the potential to leverage their favorable position in active clinical use into faster translation of this technique into widespread medical practice.

5.2 Results

5.2.1 NP Characterization

The NP-mediated generation of Auger photoelectrons, and subsequent treatment of surrounding tumor by NMDR effects, depends on the chemical composition and size of the metal NP core, as well as on the architecture of the surrounding polymer shell.[117,125,128] The ability to allow water and biomolecules in close proximity to the active core will vary, based on shell conformation, hydrophobicity, and surface charge. Thus, we synthesized multiple NPs with different iron oxide core size, redox state and polymer coating, as well as different hydrodynamic size (Figure 5.1b-c). We evaluated their potential to produce ROS upon exposure to clinical doses of γ -irradiation. The

NPs chosen for this study were all constructed in house, with an iron oxide core. Variable coatings included (i) silanized PEG monolayer (IOSPM), (ii) chitosan-PEG (CP) copolymer (NPCP), (iii) CP copolymer modified with catechol (IOCCP) and (iv) amphiphilic phospholipid-grafted PEG (IOPLP). A fifth NP was constructed with equivalent surface composition to NPCP, but with a maghemite rather than a magnetite core (MCP). Figure 5.1c demonstrates the variation in hydrodynamic size among these NP formulations, while Figure 5.1d displays TEM imaging that highlights core size and morphology of each species. Physicochemical properties for each NP type are listed in Table 5.1.

Table 5.1: Physicochemical properties of NPs evaluated for NMDR

NP	Core size (nm)	Core morphology	Core composition	Capping agent	Polymer coating
IOSPM	12.6 ± 0.9	Spherical	Fe_3O_4	Anhydride silane	PEG
IOCCP	4.9 ± 0.8	Rough spherical	Fe_3O_4	Catechol	Chitosan-PEG
NPCP	4.4 ± 1.3	Rough spherical	Fe_3O_4	Chitosan	Chitosan-PEG
MCP	3.8 ± 0.7	Rough spherical	Fe_2O_3	Chitosan	Chitosan-PEG
IOPLP	12.8 ± 0.8	Spherical	Fe_3O_4	Oleic acid	Phospholipid-PEG

5.2.2 ROS Generation in Buffered Aqueous Solution

To evaluate the propensity of each NP formulation to generate ROS during radiotherapy, ROS yields were measured in buffered aqueous solution containing NPs and the ROS indicator, 2′,7′-dichloro-dihydro-fluorescein (DCFH). We performed γ-radiotherapy fluorometric assays, while systematically varying the NP concentration (Figure 5.2a). These results were compared to identical experiments, designed with an oxidative chemical stimulus (H_2O_2) substituted for radiation. An ideal NP would generate ROS when exposed to γ radiation and would not potentiate ROS production under chemical conditions that mimic intracellular oxidation. While ROS with radiation is the desired outcome, enhanced ROS with H_2O_2 would lead us to anticipate cytotoxicity of the NP itself under resting conditions. The H_2O_2 control provides reassurance that admixture of the NP with the indicator molecule (i.e., fluorescence quenching) is not responsible for the observed effects.

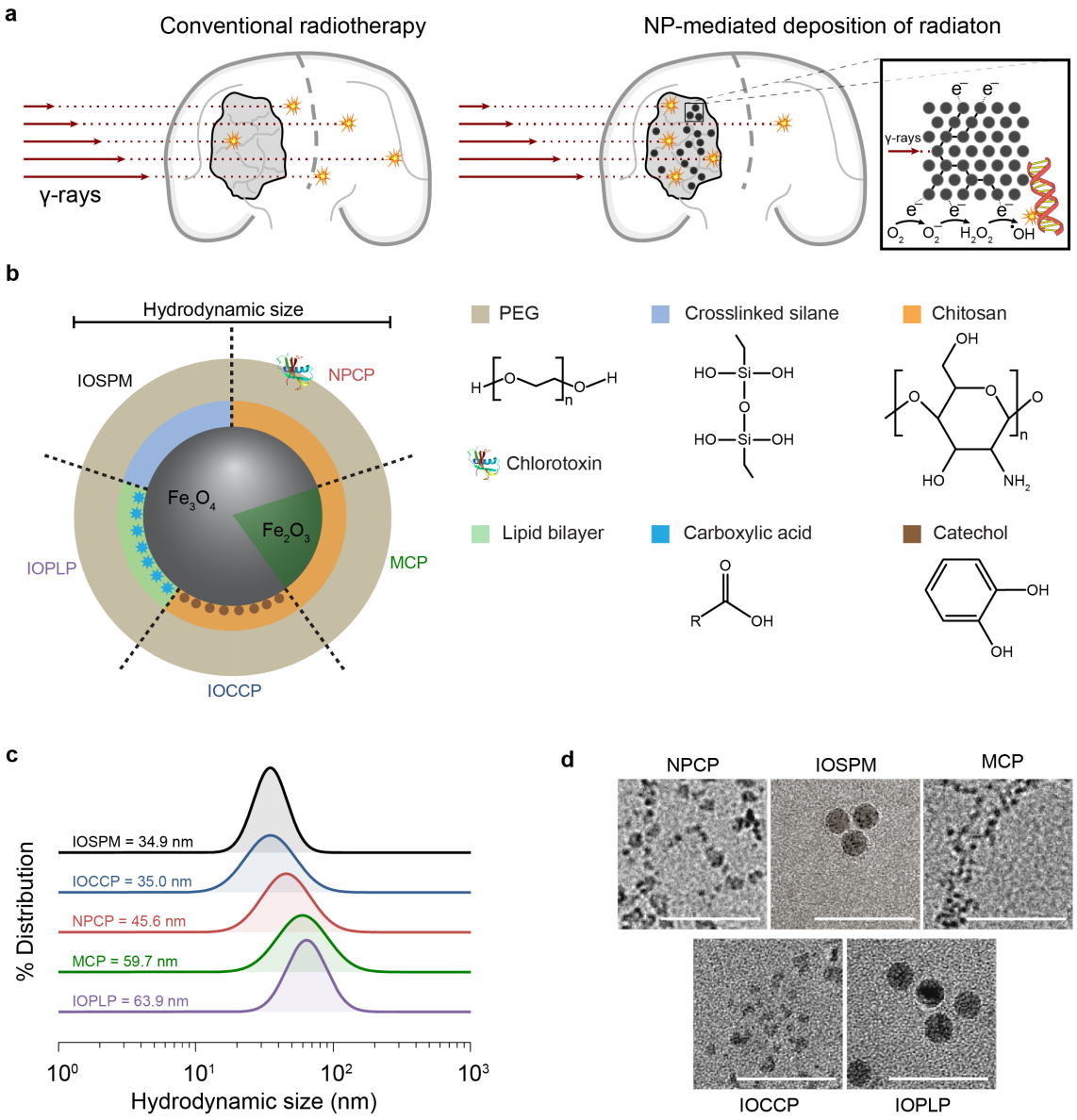

Figure 5.1: NP-mediated radiosensitization and NP size characterization. (a) Schematic illustration emphasizing the increased focusing of energy deposition in tumor regions due to the absorption of ionizing radiation by metal NPs causing radiosensitization as compared to highly scattered energy deposition characterizing conventional radiotherapy. (b) Illustrative representation of the five polymer-coated iron oxide core NPs under evaluation. (c) Intensity-based hydrodynamic size distribution for the suite of synthesized NPs obtained by dynamic light scattering. (d) Transmission electron microscopy images of each NP (scale bars = 50 nm).

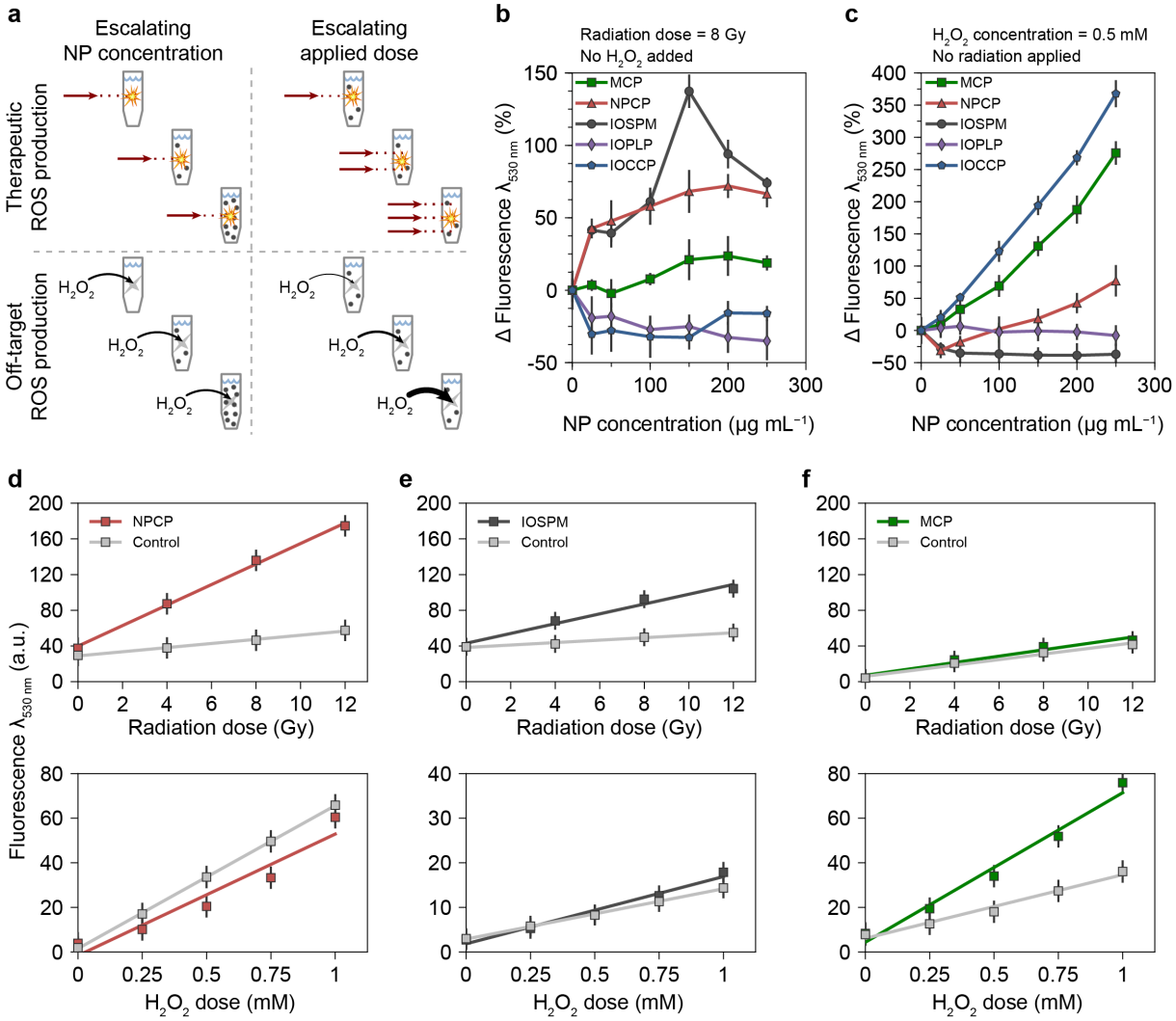

Figure 5.2: NP-enhanced ROS generation. (a) Schematic illustration of the four conditions considered in determining the best NP candidate for radiosensitization. (b) Measurement of therapeutic ROS generation as a function of NP concentration using the DCFH fluorescence assay; NPs were exposed to an 8 Gy dose of γ-irradiation at each concentration investigated. Results are expressed as percent change in fluorescence compared to post-radiation fluorescence of equivalent composition solution bearing 0 mM NPs. (c) Evaluation of off-target ROS production for each NP formulation using the DCFH fluorescence assay with added H_2O_2 (no radiation applied). (d-f) Generation of therapeutic ROS as a function of radiation dose (top) or H_2O_2 dose (bottom) for (d) NPCP, (e) IOSPM, and (f) MCP using deionized water as a control (gray). In each plot, a control curve demonstrates the fluorescence response of DCFH alone upon γ-radiation exposure. The difference in slope of the two lines is theorized to be proportional to the potency of the NMDR response. In (b-f) all experiments were performed in triplicate ($n = 3$ independent experiments) and data are shown as mean $\pm$ s. d.

Figure 5.2b shows the result of applying 8 Gy γ-irradiation to five different NPs, while varying NP concentration from 0 to 250 μg mL^{-1}. The ROS indicator was present at equal concentration in each reaction tube, and all experiments were performed in triplicate. The experiment shows that the conversion of DCFH to fluorescent 2′,7′-dichlorofluorescein (DCF) (i.e., ROS production) is greatest when NPCP and IOSPM are present. MCP, identical in shell configuration to NPCP, yields a comparatively low DCFH conversion, only apparent at higher NP concentrations ($\geq$ 150 μg mL^{-1}). Unlike other NP species, IOPLP and IOCCP do not potentiate the conversion of DCFH to DCF in the presence of γ-irradiation, but instead inhibit this conversion at all concentrations, indicating these are not candidate species for biological NMDR.

Figure 5.2c provides data after substitution of 0.5 mM H_2O_2 as the oxidizing stimulus, once again allowing the concentration of each NP species to vary. Within physiologically relevant concentrations ($<$ 100 μg mL^{-1}), NPCP exhibited little potentiation of oxidative free radical production. IOSPM had a mild ROS-scavenging effect. The enhanced conversion of DCFH to DCF caused by IOCCP and MCP in an oxidizing environment suggests that oxidative damage in vitro or in vivo might occur from these NP systems, which could cause toxicity. The disparity between results of the H_2O_2 experiment (Figure 5.2c) and the γ-radiation experiment (Figure 5.2b) suggests that the γ-irradiation results cannot be explained by natural oxidative processes, fluorescence quenching, or some unknown effect from the admixture of NP and DCFH. These results suggest that the variable of γ-irradiation itself is responsible for the potentiation of ROS by NPCP and IOSPM.

A set of additional experiments was performed on NP formulations that yielded ROS potentiation in the presence of γ-irradiation as shown above: NPCP, IOSPM, and MCP. The applied radiation dose was varied from 0–12 Gy, while maintaining NP concentration at 25 μg mL^{-1} (Figure 5.2d–f, top row). With escalating radiation dose, NPCP (Figure 5.2d, red) and IOSPM (Figure 5.2e, black) influenced a conversion of DCFH to fluorescent DCF that was significantly greater than ROS production during concurrent control radiation experiments where NP was absent (gray). The difference in slope between NP and control curves indicates that radiation-derived ROS production is amplified at higher radiation doses. In each case, the difference in control and NP slopes

effectively conveys the relative potency of the NMDR response for a given particle. As an additional control, each of these experiments was repeated using an escalating dose of H_2O_2 to initiate ROS production. Accompanying results in Figure 5.2d–f (bottom row) show that conversion of DCFH to DCF from 25 μg mL^{-1} NP in oxidizing conditions remains less than, or nearly equivalent to, that produced by H_2O_2 alone, regardless of oxidizing agent concentration. The exception to these results remains MCP. MCP differs from NPCP only in the Fe_2O_3 core composition, and the altered redox state of the maghemite core is associated with a very small difference in slope between NP and no-NP conditions (Figure 5.2f, top). In agreement with our prior results (Figure 5.2c), the action of MCP in non-radiative oxidizing conditions is to generate additional ROS compared to a condition where no particle is present (Figure 5.2f, bottom).

The production of ROS by iron oxide NMDR was highly dependent on core composition, capping agent, and polymer coating. IOCCP and NPCP were both produced by a co-precipitation synthesis process, have similar core composition, size and morphology, and an outer shell of chitosan-PEG; however, the addition of electron withdrawing catechol groups along the chitosan backbone as a capping agent on IOCCP drastically reduced ROS production of IOCCP induced by γ-irradiation. Similarly, IOSPM and IOPLP were both produced by a thermal decomposition synthesis process, share the same core composition, size and morphology, and an outer shell of PEG, yet IOPLP contains an added hydrophobic lipid bilayer between the iron oxide core and outer PEG shell, displacing water from the iron oxide surface. This change in surface configuration of IOPLP may be responsible for the low radiation-induced DCFH conversion rate, as surrounding H_2O is excluded from the region adjacent to the NP core.

Our results do not show a clear correlation between core size or hydrodynamic size and NMDR efficiency, although evaluation of NPs with a greater range of core and hydrodynamic sizes may be required to reveal a true trend. These results highlight a crucial missing link in the understanding of the mechanism of high-Z-species-mediated ROS production. The choice of capping agent, polymer coating and core composition can yield unique surface energy and bond structures along the metal-polymer interface of NPs. It is well known that perturbation of these parameters leads to great differences in magnetic properties of iron oxide NPs due to changes in electronic configuration

of atoms at the iron oxide surface.[129–131] In this case, we observe that such structural changes can impact the communication of Auger photoelectrons to surrounding water molecules and ROS-indicator species.

Based on the composite data from ROS generation in buffered aqueous solution, we conclude that a magnetite core is essential to achieving NMDR effects from an iron oxide NP, and the incorporation of maghemite is counterproductive. NPCP proved to have the greatest relative increase in ROS production for a given increase in γ-radiation dose. Given the known biocompatibility and BBB transport properties of NPCP,[84] it was chosen as the system for continued use in the remainder of this work.

5.2.3 In Vitro Iron Oxide NMDR

The NMDR effect of NPCP was tested on GBM cells in vitro, using assays of proliferative survival and metabolic activity. Figure 5.3a shows the effect of NMDR on relative clonogenic survival in the SF767 GBM cell line; cells were incubated in solution containing NPCP for 12 h at two separate doses. Cells then received variable dose γ-radiation. The plating efficiencies of NPCP-treated and NPCP-untreated cells were similar (Figure 5.4a) indicating that NPCP alone did not induce a measurable effect on clonogenic survival. The amount of iron oxide loaded into cells at the two doses was assessed using an iron quantification assay and was shown to be roughly double at treatments of 100 μg mL^{-1} compared to 25 μg mL^{-1} (Figure 5.4b). The fractional decrease in tumor cell survival roughly doubled with treatments of 100 μg mL^{-1} compared to 25 μg mL^{-1} (Figure 5.3b) for all radiation doses. The proportion of tumor cells killed with combined NP/radiation, compared to radiation alone, increased with escalating radiation dose, from $18 \pm 16\%$ (2 Gy) to $34 \pm 16\%$ (6 Gy) using 25 μg mL^{-1} NPCP and from $47 \pm 10\%$ (2 Gy) to $57 \pm 9\%$ (6 Gy) using 100 μg mL^{-1} NPCP.

To support the findings from clonogenic assay, an alamar blue assay for tumor cell metabolic activity and viability was performed using GBM6 cells exposed to variable doses of γ-radiation (Figure 5.3c). Unlike the clonogenic assay, alamar blue did not require cell replication in culture after treatment. GBM6 cells were loaded for 12 h with 50 μg mL^{-1} NPCP, followed by γ-radiation

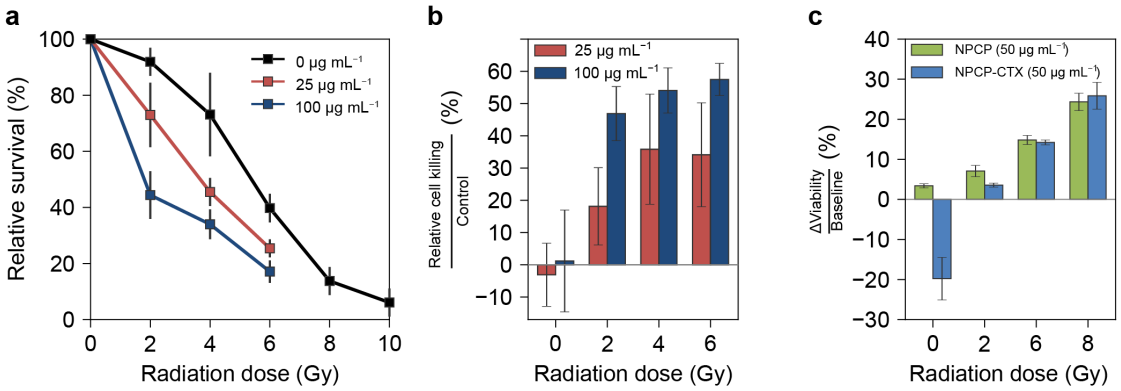

Figure 5.3: In vitro evaluation of NPCP-mediated radiosensitization. (a) Clonogenic survival as a function of radiation dose for SF767 cells incubated for 12 h with NPCP at concentrations of 0 (black), 25 (red), or 100 μg Fe mL^{-1} (blue). (b) Fractional decrease in the number of cell colonies at a given radiation dose induced by incubation with NPCP at concentrations of 25 μg Fe mL^{-1} (red) or 100 μg Fe mL^{-1} (blue) referred to the control case (cells not incubated with NPCP). (c) Alamar blue assay using 50 μg Fe mL^{-1} of NPCP (green) or NPCP-CTX (blue) as a function of γ-irradiation dose. The viability of cells exposed to NPs was normalized by viability of cells receiving no exposure to NPs, measured for each radiation dose. All experiments were performed in sextuplicate ($n = 6$ independent experiments), and data are shown as the mean ± s. d.

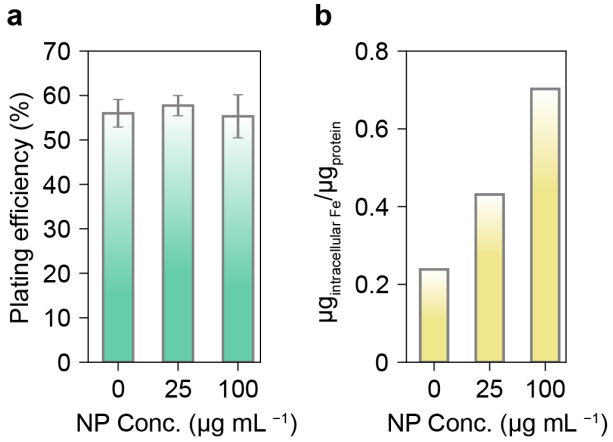

Figure 5.4: In vitro control experiments for NPCP characterization. (a) Plating efficiency of SF767 cells after 24 h of incubation with NPCP at concentrations of 0, 25, and 100 μg mL^{-1}. (b) Quantification of iron internalized by SF767 cells at NPCP concentrations of 25 and 100 μg mL^{-1} compared to the control case (0 μg mL^{-1} NPCP). All experiments were performed in triplicate ($n = 3$ independent experiments), and data are shown as mean ± s. d.

and subsequent incubation for an additional three days. The relative decrease in viability after combined radiation/NPCP compared to radiation alone ranged from –$7.1 \pm 1.3\%$ after 2 Gy/NPCP to $-24 \pm 2.3\%$ after 8 Gy/NPCP. The viability of non-radiated cells incubated with NPCP was similar to that of entirely untreated cells ($3.4 \pm 0.1\%$ change). To increase the amount of NPCP delivered to orthotopic GBM tumors in planned in vivo experiments, we conjugated the tumor-targeting peptide CTX to NPCP. We performed a direct comparison of CTX-conjugated and non-conjugated NPCP in Figure 5.3c to ensure that effects of CTX on the tumor cell (e.g., radiosensitization) do not account for any potential therapeutic results we observe in vivo. Figure 5.3c includes a comparison of data from NPCP-CTX at each radiation dose. The relative change in cell viability was roughly similar for NPCP and NPCP-CTX at radiation doses of 6 and 8 Gy indicating that the conjugation of CTX to NPCP did not significantly alter the NMDR efficacy of NPCP. Radiosensitization by CTX is therefore not expected to influence in vivo results.

5.2.4 In Vivo Iron Oxide NMDR

The superparamagnetic behavior of iron oxide NPCP allowed visualization of particles via MRI in vivo immediately after injection. Tracking of the NPs assists in selecting an acceptable time for delivery of γ-radiation after NP injection. Sequential T2*-weighted imaging was performed before and after tail vein injection of NPCP-CTX and NPCP at a total body dose of 8.5 mg kg^{-1} iron oxide. Representative T2*-weighted images displaying orthotopic primary GBM6 xenograft tumors 1 h after injection are shown for NPCP-CTX (Figure 5.5a) and NPCP (Figure 5.5b), with relative signal change in tumor and contralateral brain parenchyma shown in Figure 5.5c and 5.5d for NPCP-CTX and NPCP, respectively. Greater T2*-weighted signal change is observed in tumor compared to normal brain tissue, and a greater signal change is observed using NPCP-CTX rather than NPCP. Prior investigation has suggested that CTX-conjugation yields improved NPCP uptake past the BBB.[84] The MRI technique does not discriminate between intravascular and extravascular NP. Relative T2*-weighted signal change within the blood was determined by monitoring the external jugular vein and is shown in Figure 5.5e. We observe a linear clearance profile of NPCP-CTX from the blood, similar to that observed in prior work (see Chapter 3). A plateau appears

in tumor tissue before NP elimination; such a difference in the pharmacokinetics of NPCP-CTX between blood and tumor tissue indicates the extravasation of NPCP-CTX from the blood into the tumor region at which point NPCP-CTX is retained for a period before washout occurs. Although prior research has suggested that intracellular NPs may persist for 5 days,[84] we chose to deliver γ-radiation 1 h after tail vein injection when the greatest concentration of overall NPs was present in the bulk tumor as indicated by our time-resolved MRI. Figure 5.5f illustrates the planned course of treatment and monitoring. MRI of mice was performed weekly, and magnetic resonance spectroscopy (MRS) was obtained 1.5 weeks after treatment.

NPCP-CTX with concurrent 10 Gy single dose γ-radiation was delivered to mice bearing orthotopic GBM6 xenograft tumors, with examination of tumor size and survival. Control groups included untreated mice, mice receiving only NPCP-CTX, and mice receiving only γ-irradiation. Three mice in each group were designated to serial MRI study, receiving weekly scans. Representative T2-weighted images of tumor development in each of the experimental categories are provided in Figure 5.6a. Average volumetric tumor size is displayed in Figure 5.6b. Tumor growth profiles of the untreated and NPCP-CTX-treated groups were not significantly different. Treatment with a single 10 Gy dose of γ-irradiation showed an expected reduction in tumor growth rate. The group treated with NPCP-CTX + 10 Gy γ-irradiation group demonstrated a greater reduction in tumor growth rate. Linear regression analysis performed on the 10 Gy only and NPCP-CTX + 10 Gy tumor growth curves showed that the NPCP-CTX + 10 Gy group exhibited a 3-fold decrease in tumor growth rate compared to the 10 Gy only group from weeks 4 through 6.

Kaplan-Meier survival curves are shown in Figure 5.6c, with log rank statistical analysis of median survival supplied in Figure 5.6d. Animals treated with NPCP-CTX concomitantly with a 10 Gy dose of γ-irradiation showed a 2-fold increase in median survival as compared to animals receiving only γ-irradiation, with a median survival time of 61 days in comparison to 30 days for γ-irradiation alone, 29 days for NPCP-CTX control, and 28 days for untreated animals. The log rank statistic for comparison between the NPCP-CTX + 10 Gy group and the 10 Gy-only group showed a statistically significant difference ($p = 0.003$). These results suggest that the combined effect of targeted NPCP-CTX and γ-irradiation confers a survival advantage to mice bearing GBM6 brain

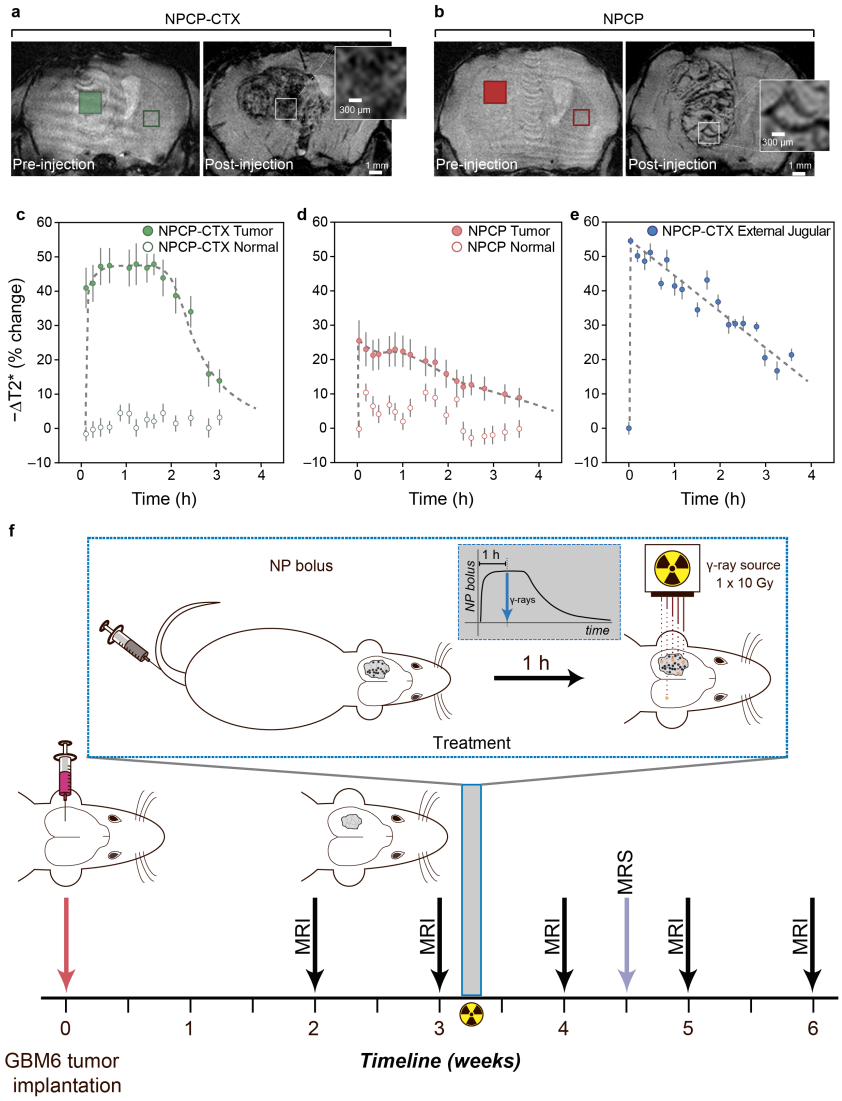

Figure 5.5: Preferential NPCP-CTX uptake in tumor regions compared to NPCP without CTX. (a) Pre- (left) and post-injection (right) MRI T2*-weighted scans showing uptake of NPCP-CTX in tumor tissue. (b) Pre- (left) and post-injection (right) T2*-weighted images showing NPCPs in tumor tissue. (c) T2*-weighted signal change from pre-injection baseline (expressed as a percentage) in tumor regions of interest (filled circles) and healthy brain regions of interest (unfilled circles) for a mouse injected with NPCP-CTX (green) and (d) a mouse injected with NPCP (red). The data are shown as mean ± s. d. from the average of experiments performed in triplicate ($n = 3$ independent experiments) where 100-voxel regions of interest were used to determine T2*-weighted signal intensity normalized to the intensity of a water phantom. (e) T2*-weighted signal change from pre-injection baseline (expressed as a percentage) in the external jugular vein. (f) Tumor inoculation and treatment timeline. Radiotherapy was performed 1 h after NPCP-CTX administration.

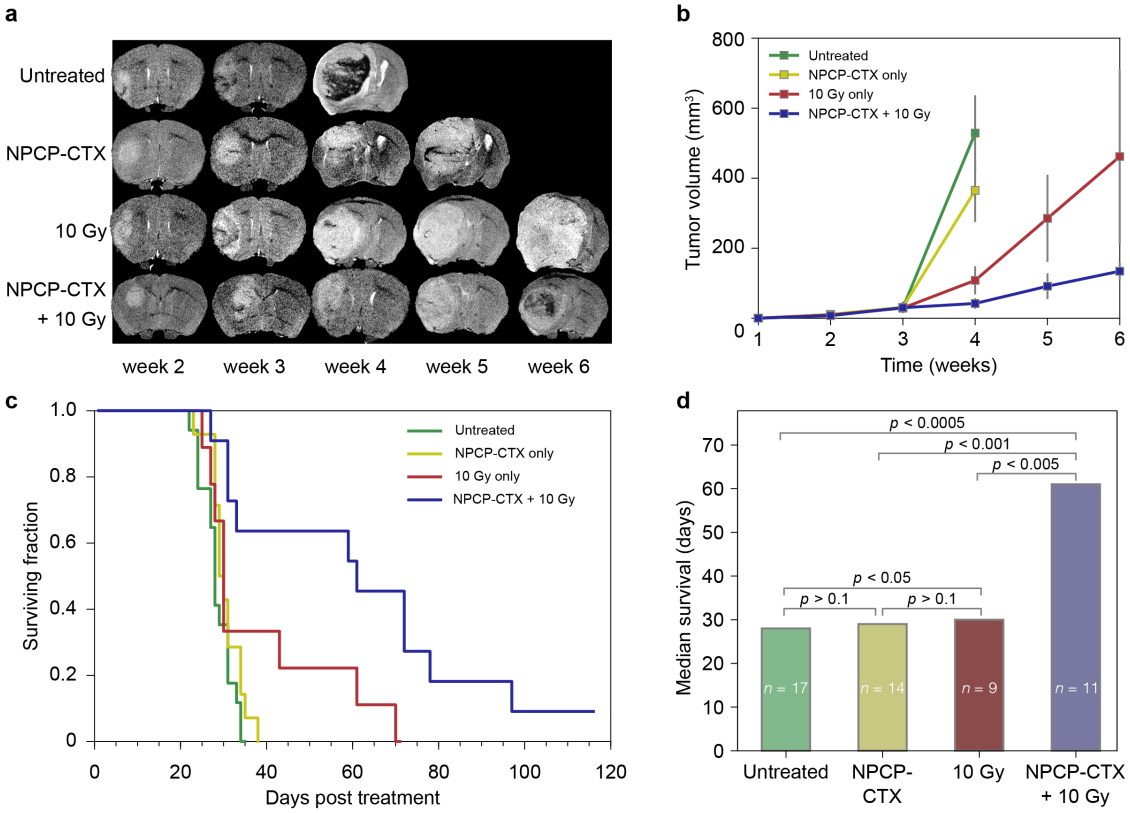

Figure 5.6: Increased survival by administration of NPCP-CTX and γ-irradation. (a) Representative T2-weighted MRI scans emphasizing the size progression of tumors for each treatment group. (b) Graph of mean tumor volume versus time for each treatment group ($n = 3$ mice per group). Data are shown as mean $\pm$ s. d. (c) Kaplan-Meier survival curve. (d) Median survival for each treatment group. Statistical analysis was performed using the log rank test. In (c) and (d), $n = 17$, 14, 9, and 12 for the untreated control, NPCP-CTX control, 10 Gy γ-irradiation control, and combined NPCP + 10 Gy γ-irradiation treatment groups, respectively.

tumors. While a single radiation dose (10 Gy) was used in the current study, fractionation protocols may be investigated in future work.

In vivo MRS was performed to reveal potential in vivo neurochemical effects of our treatment modality. Distinct benefits of MRS include (i) the examination of living tissue, (ii) the ability to observe results that may only be evident shortly after treatment and while mice remain alive for survival studies, and (iii) to test all animals at an equivalent time point, rather than at variable times upon sacrifice. MRS data were collected from 2 mice from each of the 4 groups (8 mice total), 1.5 weeks after treatment. This intermediate time delay was selected as it was short enough

to ensure that at least 2 surviving mice were present in each imaging group and long enough to provide maximal elimination of any NPCP-CTX accumulated in tumor tissue. Furthermore, the time delay provided results that measured a durable effect on tissue properties, rather than a transient effect that could occur immediately after treatment. Figure 5.7a displays spectra measured for one mouse in each cohort and Figure 5.7b shows the spectra from a second cohort. Chemical shifts for key metabolites are designated on the first spectrum, including creatine (Cr), myoinositol (Myo), choline (Cho), glutamate and glutamine (Glx), N-acetylaspartate (NAA), and lipid/lactate. Our data demonstrate a marked increase in concentration of lactate in tumor tissue of the NPCP-CTX + 10 Gy group compared to all other treatment groups. The sharp spike in lactate signifies necrosis and ischemia of tumor tissue.[132–134] Since the chosen region of evaluation for MRS consisted of homogeneous tumor tissue and avoided any gross central tumor necrosis, the results suggest a boost in the local damage caused by radiation.[132] Since all tumors were formed from the same group of GBM6 cells, these results cannot be explained by a difference in tumor type. The increase in lipid/lactate was present within the tumor, and not present in contralateral brain, despite the whole-brain coverage of radiation. The combined results show that enhanced tumor cell killing only occurs in the region where NPs are preferentially targeted by CTX. Other metabolites identified in the spectra remained relatively constant across all treatment groups. To quantify the increase in lipid/lactate for the NMDR treatment group relative to other groups, the average integral of the lactate peak was calculated for each spectrum (Figure 5.7c). Furthermore, the ratio of the lactate to Cr peak was computed as a reference for peak normalization (Figure 5.7d), since Cr is relatively stable in the brain and is thus used for calculating metabolite ratios.[135] As expected for neoplastic tissue in the brain, the Cho:Cr ratio is greater than 1:1 for all tumor spectra, and less than 1:1 for all contralateral brain tissue spectra, with NAA peaks that are greater in normal brain than those in tumor.[133] In future work, serial in vivo MRS may be useful to monitor the temporal changes before and after treatment.

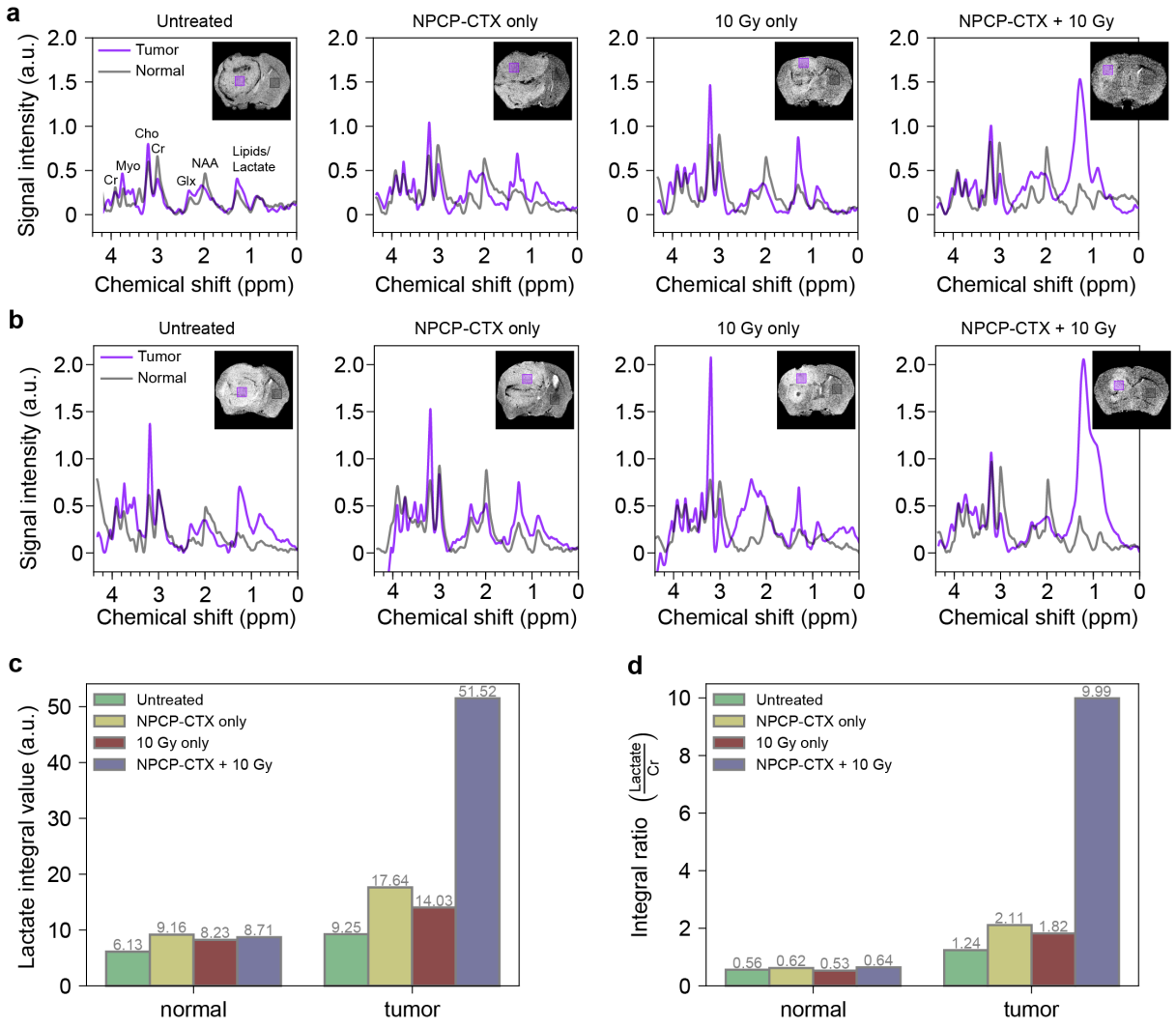

Figure 5.7: Magnetic resonance spectroscopy of normal and tumor tissue. (a) and (b) Magnetic resonance spectra acquired in healthy and tumorous regions of interest. Inset images presented show choice of region of interest in tumor and contralateral brain. (c) and (d) Results from the integration of the lactate peaks and the ratio of the integration of lactate-to-creatine peaks for the spectra shown in (a), respectively.

5.3 Materials and Methods

5.3.1 Materials

All chemicals were purchased from Sigma-Aldrich (St. Louis, MO) unless otherwise stated. Cell culture reagents including Dulbecco's Modified Eagle Medium (DMEM) and antibiotic-antimycotic

were purchased from Invitrogen (Carlsbad, CA). Fetal bovine serum (FBS) was purchased from Atlanta Biologicals (Lawrenceville, GA). 3-(Triethoxysilyl)propylsuccinic anhydride (SATES) was purchased from Gelest (Arlington, VA).

5.3.2 NP Synthesis

Maghemite NP

Uncoated iron oxide NPs were synthesized via co-precipitation, mixing 570 mg of Fe^{3+} iron chloride in 18 mL of degassed deionized (DI) water. This solution was then passed through a 0.2 μm cellulose acetate filter. Next, the solution was placed in a sonicated water bath heated to 40°C. Ammonium hydroxide (14.5 M) was slowly titrated into the solution over a period of 45 min until a final pH of 10.5 was reached, ensuring complete NP nucleation.

NPCP and NPCP-CTX

Iron oxide NPs were synthesized and coated with PEG grafted onto depolymerized chitosan by a co-precipitation method described previously.[83,136] CTX (Alamone Laboratories, Jerusalem, Israel) was conjugated to NPCPs as reported previously.[92]

IOSPM

Oleic aid coated iron oxide NPs (IOOA) were synthesized as previously reported.[48] To confer water solubility, a ligand exchange process was used to provide a hydrophilic PEG coating. 50 mg of IOOA was suspended in 43 mL of anhydrous toluene followed by addition of 50 μL of triethylamine in a 3 neck round-bottom flask fitted with a Graham condenser. The flask was sealed with rubber septa and purged with nitrogen. The solution was heated to 100°C and 0.10 mL of SATES was added to the flask. 187.5 mg of mPEG2K-NH_2 was dissolved in 7 mL of anhydrous toluene and the resultant solution was added to the flask 15 min after the addition of SATES. An additional 50 μL of SATES was injected 1 h after the mPEG2K-NH_2 injection, and the solution was reacted for a further 6 h and 45 min. The solution was transferred to a single neck round-bottom flask and

NPs were precipitated with hexane. The NP precipitate was dispersed in tetrahydrofuran (THF), sonicated for 10 min and precipitated with hexane. The resulting NP pellet was suspended in 10 mL anhydrous THF and sonicated for 10 min. 62.5 mg of mPEG2K-NH_2 and 187.5 mg of 2000 MW bis(amine) functionalized PEG (PEG2K-bis(amine)) was dissolved in 12 mL of anhydrous THF and added to the NP solution. The flask was then sealed with a septum and purged with nitrogen. 12.5 mg of N,N^1-dicyclohexylcarbodiimide was dissolved in 2 mL of anhydrous THF and added to the flask, and the reaction solution was placed in a sonication bath at 25°C and allowed to react for 16 h. Fully PEGylated NPs were precipitated with hexane, re-dispersed in 20 mL ethanol, sonicated for 10 min and precipitated again with hexane. The pellet was fully dried and dispersed in PBS with sonication for 10 min.

IOPLP

IOOA (1 mg) was mixed with 1 mL of acetone and sonicated for 10 min to remove free oleic acid. The mixture was placed on a magnet to separate IOOA from the solution. Acetone was decanted and IOOA was dried with nitrogen flow. IOOA and 20 mg of 18:0 PEG2000 PE (Avanti Polar Lipids, Inc., Alabaster, AL) was dispersed in 1 mL chloroform. 4 mL of dimethyl sulfoxide (DMSO) was added drop wise with constant stirring, followed by rocking at room temperature for 30 min. Chloroform was removed by vacuum and 16 mL of DI water was added drop wise with constant stirring. The mixture was then concentrated and purified using an Amicon Ultra centrifugal filter (EMD Millipore, Billerica, MA) following the manufacturer's instructions. Once concentrated to 1 mL, the mixture was washed with 2 mL of DI water three times to remove residual DMSO.

IOCCP

Iron oxide NPs coated with a catechol modified chitosan-PEG copolymer (IOCCP) were synthesized per established methods.

5.3.3 NP Size Characterization

The hydrodynamic size of NPs was determined by dynamic light scattering at 100 μg mL^{-1} in 20 mM HEPES buffer (pH 7.4) using a Zetasizer Nano (Malvern Instruments, Worcestershire, UK). Transmission electron microscopy (TEM) images were acquired with an FEI TECNAI F20 TEM (Hillsboro, OR) operating at 200 kV.

5.3.4 Radiation Delivery

Cells in culture and tumor-bearing animals were exposed to ionizing radiation at room temperature using a calibrated Mark I ^{137}Cs γ-irradiator (J. L. Shepherd and Associates, Glendale, CA). The dose rate for irradiation was 1.1 Gy min^{-1}. For in vivo experiments, the anesthetized mouse was positioned below an overhead radiation source, with the region from caudal skull base to the feet surrounded with continuous 50 mm thickness lead to shield off-target radiation.

5.3.5 ROS Measurement

Evaluation of ROS production by NPs in aqueous solution were performed using the 2′,7′-dichloro-dihydro-fluorescein diacetate (DCFH-DA) assay. Appropriate NP volumes were added to PBS buffer, resulting in final volumes of 200 μL held in 96-well plates. All experimental mixtures were prepared in dark conditions to prevent autoconversion of DCFH-DA by ambient light. Each well was loaded with 100 μM DCFH-DA. For ROS production, either ^{137}Cs-γ-rays or H_2O_2 was delivered at the stated dose. For H_2O_2 experiments, equal volume was maintained across experimental and control solutions by addition of either H_2O_2 or PBS, respectively. ROS generation was monitored by conversion of non-fluorescent DCFH into fluorescent DCF (SpectraMax i3 microplate reader; Molecular Devices, Sunnyvale, CA). Excitation and emission wavelengths were 480 nm and 530 nm, respectively.

5.3.6 Cell Culture

Human GBM cells from the SF767 line were obtained from the tissue bank of the Brain Tumor Research Center (University of California–San Francisco, San Francisco, CA) and maintained in DMEM supplemented with 10% FBS and 1% antibiotic-antimycotic. GBM6 cells were obtained from Mayo clinic and maintained as flank tumors in nude mice. Cultures were held at 37°C in a humidified incubator with 5% CO_2.[85]

5.3.7 Clonogenic Survival Assay

SF767 cells were assessed via clonogenic assay for proliferative survival after incubation with variable NPCP concentration and delivery of variable radiation dose. Full details of clonogenic method were previously described.[83] Briefly, NPCP concentrations of 0, 25, and 100 μg Fe mL^{-1} in DMEM were added to 6-well plates containing 250 cells per well. Cells were incubated for 12 h at 37°C in air containing 5% CO_2, followed by 2× washing with PBS, and returned to DMEM. Plates were then exposed to variable γ-irradiation doses of 0, 2, 4, 6, 8, and 10 Gy. Incubation was resumed for 8 days, and during this time, colonies were counted by light microscopy, and only colonies with 50 or more cells were counted. Survival (mean ± s. d.) is expressed as the ratio of colonies formed by treated cells to that of untreated cells (i.e., no γ-irradiation). All clonogenic survival studies were performed in sextuplicate. Plating efficiency was determined at all NP incubation concentrations to ensure that NP delivery did not alter the number of viable cells. Separate culture wells were used for cell ferrozine assay[136] and performed in triplicate to determine the amount of intracellular iron resulting from NP incubation at variable concentration.

5.3.8 Alamar Blue Assay

GBM6 cells were incubated for 12 h on 12-well culture plates at 37°C in a 50 μg mL^{-1} solution of NPCP or NPCP-CTX. After 2× washing with PBS, cells were counted and vials of equivalent cell number were exposed to γ-irradiation doses of 0, 2, 6, or 8 Gy. Cultures were allowed to incubate after treatment for 3 additional days. Cells were detached and resuspended in 1 mL of DMEM

containing 10% alamar blue reagent. After 90 min additional incubation, 300 μg of supernatant was removed and added to black 96-well microplates designed for fluorescence assay. Conversion of resazurin to resorufin was measured using excitation and emission wavelengths of 560 nm and 590 nm, respectively.

5.3.9 In Vivo Survival Study

All animal studies were conducted in accordance with approved protocols from the University of Washington's Institute of Animal Care and Use Committee and federal guidelines. Female, nude athymic mice were used in all animal studies. Human-derived GBM6 cells were thawed and maintained through 2 passage cycles as a flank tumor, prior to sterile intracranial implantation as described previously.[83] Tumor growth was monitored with MRI for 12 mice, with 23 days between implantation and treatment, allowing for tumors to grow to approximately 30 mm^3 in size. At the third week, tumors were reliably visible in all 12 imaged mice. Mice were randomized to groups for no treatment, NP injection only, γ-irradiation only, combination NP and γ treatment, with a post-randomization check to ensure that starting tumor size was similar across groups.

Control and treatment groups for the survival study are listed as follows: (i) untreated control group ($n = 17$), (ii) NPCP-CTX control group ($n = 14$; this treatment group received a total body iron oxide dose of 8.5 mg kg^{-1}, with an iron oxide concentration of injected solution of $\sim$0.8 mg Fe mL^{-1} and a total injection volume of $\sim$200 μL, and the final injection volume was adjusted based on exact animal weight), (iii) 10 Gy γ-irradiation control group ($n = 9$) and (iv) combined NPCP-CTX + 10 Gy treatment group ($n = 12$). In group iv, radiation was delivered 1 h after NPCP-CTX injection, with equivalent NP and radiation doses compared to control groups ii and iii, respectively. All injected solutions were prepared and conjugated to CTX on the day of injection. Injections were performed via tail vein puncture. Mice were monitored daily and euthanized when they became moribund. Survival was monitored and analyzed using a Kaplan-Meier plot. Statistical analysis was performed using the log rank test.

5.3.10 Magnetic Resonance Imaging

MRI was performed on a 14 T (600 MHz) Bruker Avance III vertical-bore spectrometer. Isoflurane (Piramal Healthcare) in oxygen was supplied through a coil-integrated respiratory monitoring system (SA Instruments), with bite bar and ear bar restraints to maintain fixed head position. Respiratory rate was monitored to control depth of anesthesia, and a circulating water control bath maintained constant temperature.

Four h of sequential T2*-weighted imaging was performed to measure intracranial presence of NPCP and NPCP-CTX in healthy and tumor tissue. T2*-weighted images were acquired every 10 min with a fast low angle shot (FLASH) pulse sequence in the coronal plane (TE= 6.0 ms, TR = 1000 ms, in-plane resolution 78×78 μm^2, slice thickness 0.5 mm). Scan duration was approximately 4 min. Analysis of images was accomplished using the Paravision 5.1 analysis package (Bruker) and Osirix (Pixmeo).[137] To account for inherent signal intensity changes due to inter-scan drift in gain, power, shim and tuning, all images were normalized based on the intensity of a water phantom located adjacent to the mouse head. Magnetic susceptibilities of NPCP and NPCP-CTX were tested in aqueous solution and were found to be identical.

Using groups of three mice from each experimental group (12 total), in vivo MRI of mice was performed once a week from the time of tumor implantation to monitor the growth of the implanted GBM tumors (6 weeks total scanning). Whole-head coronal orientation T2-weighted images were acquired using the rapid acquisition with refocused echoes (RARE) pulse sequence (TE = 6.78 ms, TR = 4000 ms, in-plane resolution 78×52 μm^2, slice thickness 0.5 mm). Scan duration was approximately 4 min. 3D tumor volumes were calculated using Paravision 5.1 analysis software over the complete set of slices encompassing each tumor. Volumetric analysis was based on the T2 signal intensity change between the tumor margin and normal brain. Volume was measured independently by three separate observers and averaged to account for human error in boundary estimation.

5.3.11 Magnetic Resonance Spectroscopy

MRS was performed on mice from each of the treatment groups defined previously. A ^{1}H point resolved spectroscopy (PRESS) scan sequence was used with water suppression (TR = 2.5 s, TE = 30 ms, SW = 50 kHz, NA = 480). For tumor MRS, the single 10 mm^3 voxel was prescribed at the outer boundary of the tumor, maintaining the entirety of the voxel within tumor tissue, and avoiding the potentially necrotic central tumor region. For non-tumor MRS, the voxel was prescribed within contralateral cortical brain tissue, at a distance of 2–3 mm from the primary tumor. Duration of each scan was approximately 20 min. Phase correction and apodization were carried out with the Paravision 5.1 analysis package. Spectral peak integrals were calculated using Gaussian/Lorentzian curve fitting software programs developed in MATLAB (The Mathworks, Inc).

5.4 Conclusions

In this study, an innovation on classic whole-brain radiotherapy is explored using biocompatible targeted iron oxide NPs to facilitate production of Auger photoelectrons. We find that NP-mediated deposition of radiation does not occur equally with all NP preparations. Chemical experiments were performed on a suite of iron oxide NPs, and demonstrated a dependence of radiation-induced ROS production on the redox state of the iron oxide core, the capping agent and the polymer coating. Magnetite particles produced a high NMDR effect while maghemite particles did not; the inclusion of electron withdrawing catechol groups as a capping agent diminished ROS yield; the sequestration of water from the magnetite core by incorporation of a lipid layer significantly reduced ROS production. Furthermore, NPs synthesized with a maghemite core or an electron-withdrawing catechol capping agent led to undesirable production of ROS under oxidizing conditions. After screening for a highly functional and biocompatible NP formulation (NPCP), we tested this resulting particle in culture with two GBM cell lines (SF767 and GBM6). The combined γ-radiation plus NPCP treatment was found to yield enhanced cell killing, compared to radiation alone, or NP delivery alone. We investigated the conjugation of NPCP to the tumor-targeting peptide CTX, which

has been demonstrated to be biocompatible, with the ability to cross the BBB[84] and accumulate in GBM tumor.[138–140] Using time-resolved T2*-weighted MRI, we studied the optimal timing for delivery of NP and γ-radiation in tandem to mice bearing GBM6 tumors. Treatment with NPCP-CTX combined with γ-radiation was performed in vivo. We show 2-fold improvement in survival and 3-fold suppression of tumor growth rates, compared to mice receiving radiation alone. This result occurs in the setting of a known rapidly lethal GBM6 tumor, and the substantial growth of tumors allowed at 3 weeks, prior to initiation of therapy. These results are supplemented by in vivo MRS, 1.5 weeks after therapy, using mice from each treatment group. Spectra reveal that the combined therapy generates a large increase in lactate within tumor, that is not observed in normal brain.

In modern tumor radiotherapy, the goal to focus radiation on a cell-specific level remains of paramount importance. Especially relevant in GBM where distant cellular spread is known to occur, an NP agent can be designed to home to tumor cells and increase the extent of radiation deposition in those areas. We investigate this phenomena using an iron oxide NP that has known low toxicity, good visibility as an MRI contrast agent, and high potential for clinical approval. Our results suggest that NMDR may be a useful and low-risk adjunct to modern combined chemoradiotherapy.

Chapter 6

BORON-DOPED GRAPHENE QUANTUM DOTS AS METAL-FREE MRI CONTRAST AGENTS

Gadolinium (Gd) chelates are used as clinical T1 contrast agents for magnetic resonance imaging (MRI) due to their demonstrated high sensitivity and positive contrast enhancement capability. However, there has been an increasing safety concern with respect to their use in medicine because of the toxicity of the metal Gd ions released from these contrast agents when used in vivo. Although significant effort has been expended towards developing metal-free MRI contrast agents, none existing have matched the magnetic properties achieved by the gold standard clinical contrast agent, Gd diethylene penta-acetic acid (Gd-DTPA). We have developed a single-layer, boron-doped graphene quantum dot (termed SL-BGQD) that demonstrates better T1 contrast enhancement than Gd-DTPA. The SL-BGQD is shown to provide significantly higher positive contrast enhancement than the Gd-DTPA contrast agent in imaging vital organs, including kidney, liver, spleen, and blood vasculature. Further, our results show that SL-BGQDs are able to bypass the blood-brain barrier (BBB) and allow sustained imaging for at least one hour with a single injection. Hematological and histopathological analyses show that the SL-BGQD demonstrates a non-toxic profile in wild-type mice and may, therefore, serve as an improved, safer alternative to currently available clinical MRI contrast agents.

6.1 Introduction

A variety of imaging technologies have been developed for disease diagnosis and its early detection and are used in the clinic, including magnetic resonance (MR) imaging, optical fluorescence imaging, X-ray computed tomography, positron-emission tomography, and ultrasound imaging.[141,142] Among these imaging technologies, MR imaging is one of the most powerful non-invasive diag-

nostic modalities for the determination of locations and extents of diseased tissues. In MR imaging, contrast arises from the difference in the MR relaxivity of hydrogen nuclei in water molecules between different tissues; these disparities are caused by the unique local magnetic field properties in which the hydrogen nuclei reside.[143] Although the diagnosis of major diseases by MR imaging has achieved significant progress, the ability to differentiate diseased tissue from healthy tissue remains to be improved, especially at the early stages of disease.[144] The introduction of contrast agents to MR imaging has become increasingly important to the improvement of diagnostic imaging. More than half of MR imaging studies performed nowadays involve the use of contrast agents.[145] Contrast enhancement is achieved by increasing the rate of transverse relaxation, R2, in T2-weighted imaging or by accelerating the recovery of the longitudinal relaxation rate, R1, in T1-weighted imaging.[146] Contrast agents used for T1-weighted imaging produce hyperintense contrast; that is, images appear brighter due to the presence of the contrast agents. However, clinical T1-weighted contrast agents, primarily Gd-based chelates or complexes, have their limitations including (i) low vascular permeation, (ii) poor sensitivity limiting their diagnostic efficacy, (iii) rapid renal clearance, (iv) the potential risk of causing nephrogenic systemic fibrosis in patients with declining renal function,[147,148] and (v) potential harmful effects on the brain due to long-term Gd retention in neurological tissue.[149,150]

Use of nanomaterials to develop T1 contrast agents may overcome the limitations of current Gd-based contrast agents.[151–154] Paramagnetic metal-based nanoparticles (NPs) have been found to produce MR sensitivities greater than Gd-based complexes.[155–159] However, the potential of metal leaching associated with these NPs poses safety concerns and leads to particle aggregation, therefore, hindering their use in long-term in vivo imaging applications. Although surface coating of metal-NP contrast agents may temporarily reduce the risk of toxicity by suppressing the release of metal atoms into the body, the eventual degradation of the nanomaterial, which is an intentional design consideration for most nanomaterials used for in vivo applications, would lead to the release of metal atoms.[160,161] Additionally, the surface coating may hamper the diffusion of water molecules towards paramagnetic sites within the NPs, thus weakening the observed MR signal enhancement.[160] Furthermore, the increased hydrodynamic size ($>$ 100 nm) due to the coating

may compromise the NP's ability to cross the BBB, thereby limiting their use in neurological MR imaging.[162] These limitations prompt the incentive to develop small-size, metal-free MR contrast agents with minimal biological toxicity and higher imaging sensitivity.

Graphene quantum dots (GQDs) have attracted much attention in medicine due to their biologically benign properties demonstrated both in vitro and in vivo.[163] By doping GQDs with a non-metallic element (e.g., boron or fluorine), the non-magnetic GQDs become magnetic and are able to serve as contrast agents in T1-weighted MR imaging.[164,165] The ability of a contrast agent to enhance the T1-weighted signal in an MR image is correlated to its longitudinal relaxivity, r_1, value and the ratio of the transverse relaxivity, r_2, to the longitudinal relaxivity (i.e., r_2/r_1). The greater the r_1, the greater the observed T1-weighted signal enhancement; meanwhile, the r_2 of the agent should be limited; otherwise, a large r_2 would overshadow the agent's effect on the longitudinal MR properties.[166] Practically, a T1 contrast agent is required to have $r_1 > 5$ mM^{-1} s^{-1} and $r_2/r_1 < 5$ for contrast enhancement.[155,167] The GQD-based contrast agents reported thus far have yet to achieve the requisite low r_2/r_1 ratio; in other words, they have not demonstrated a T1 contrast enhancement ability comparable to that exhibited by clinically used Gd-based contrast agents. One possible factor that leads to the observed limited performance of these agents is their multi-layered structure (e.g., a GQD composed of many stacked sheets of graphene held together by electrostatic forces). The multi-layer structure inhibits the diffusion of water towards paramagnetic sites created by dopants or vacancy defects, which may weaken the contrast enhancement ability of the material. Metal-free NPs have less active paramagnetic centers than Gd complexes and thus have lower r_1 values (i.e., low T1 contrast enhancement).

Here, we demonstrate the production of single-layer, boron-doped GQDs (SL-BGQDs) that circumvent the limitations discussed above and substantially improve MR contrast enhancement capabilities. The high MR T1 contrast enhancement is achieved by the creation of a large number of paramagnetic centers within the graphene lattice through boron doping that creates defects and by maximizing the interaction between water molecules and paramagnetic centers on both sides of the single-layer material. SL-BGQDs are shown to have a higher longitudinal relaxivity ($r_1 = 8.5$ mM^{-1} s^{-1}) and a slightly lower r_2/r_1 ratio ($= 1.08$), as compared to the clinical T1

contrast agent Gd-DTPA with $r_1 = 4.3\ \mathrm{mM}^{-1}\ \mathrm{s}^{-1}$ and $r_2/r_1 = 1.17$ at a magnetic field strength of 14 T. Significantly, SL-BGQDs exhibit no cytotoxicity to cells and tissues while Gd-DTPA was found to be toxic. T1-weighted MR images of mice intravenously injected with either SL-BGQDs or Gd-DTPA showed that the injection of SL-BGQDs demonstrated greater contrast enhancement than the injection of Gd-DTPA in vital organs including kidney, liver, spleen, and vasculatures. Finally, confocal microscopy images of brain tissues acquired from wild-type mice after intravenous administration of SL-BGQDs revealed SL-BGQDs' ability to cross the BBB.

6.2 Results and Discussion

To synthesize boron-doped GQDs of only a single layer, we modified a one-step solvothermal process we established previously for the synthesis of multi-layered, boron-doped GQDs.[165] The same precursors, 4-vinylphenylboronic acid (VPBA) and boric acid, and solution (acetone/hydrogen peroxide), were used here. The amount of hydrogen peroxide was doubled to create a larger liquid-gas interface upon which to decompose VPBA molecules, and thus form GQDs with a smaller size, a narrower size distribution, and fewer layers. The transmission electron microscopy (TEM) image in Figure 6.1a shows that SL-BGQDs are well dispersed and have an average size of 4.6 ± 1.4 nm (Figure B.1 of Appendix B). The high-resolution TEM (HR-TEM) image in Figure 6.1b reveals that SL-BGQDs have a superlattice structure with an interplanar distance of $\sim$0.237 nm, corresponding to the (100) lattice planes of graphite.[168] Vacancy defects in SL-BGQDs are also identifiable in Figure 6.1b (red circles). The thickness of the SL-BGQDs was characterized by atomic force microscopy (AFM) to be around 0.8 nm (Figure 6.1c and d), indicating a single-layer structure of SL-BGQDs.[169] The single-layer structure eliminates the possibility of spin pairing of boron in adjacent graphene layers as occurs in multi-layer boron-doped GQD architectures and facilitates the bidirectional interaction of water molecules with the boron atoms in SL-BGQDs, which improves their magnetic properties and their ability for contrast enhancement in MR imaging.

Powder X-ray diffraction (XRD) and Raman spectroscopy were used to obtain further crystallographic structure and phase purity information, respectively, of SL-BGQDs (Figures B.2 and B.3 of Appendix B). The characteristic peak at $\sim 20^\circ$ in the XRD pattern (Figure B.2 of Appendix B)

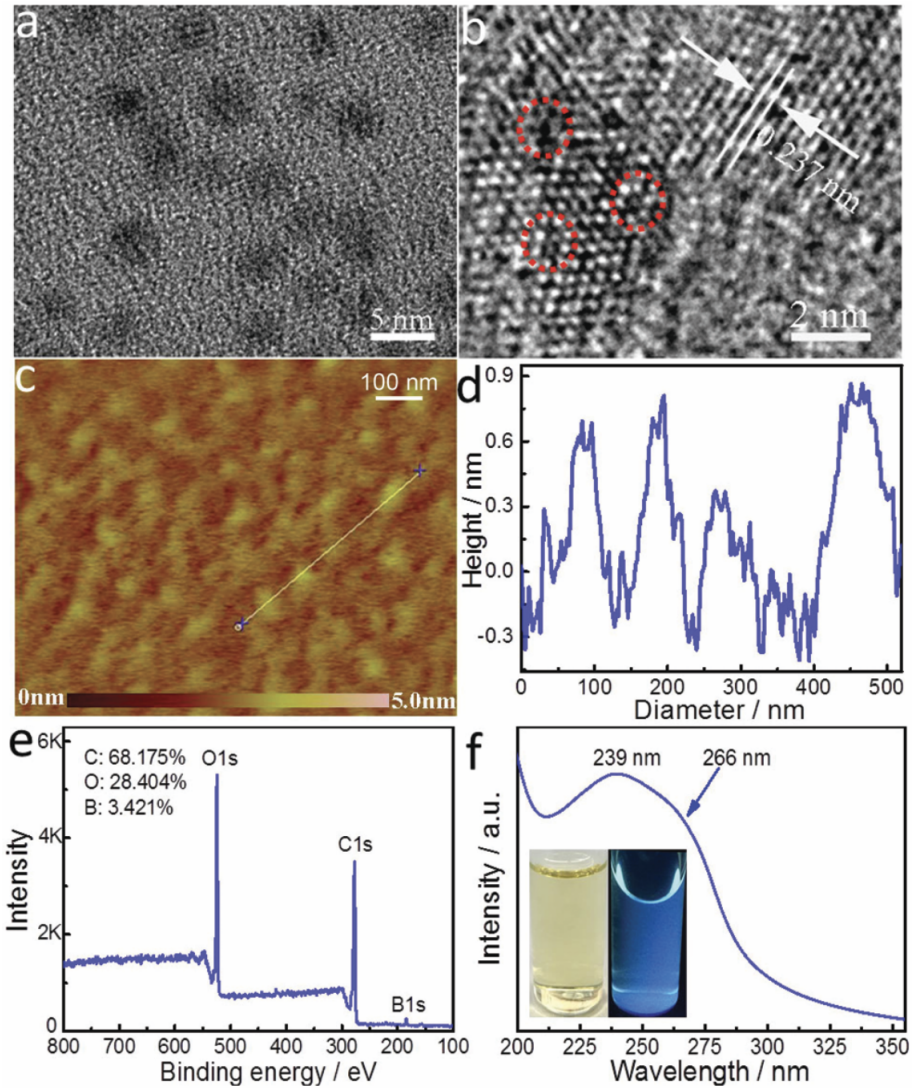

Figure 6.1: Physicochemical properties of SL-BGQDs. (a) TEM and (b) HR-TEM images of SL-BGQDs. The red circles in (b) mark the locations of vacancy defects in SL-BGQDs. (c) AFM image and (d) the height profile corresponding to the white line segment shown in (c). (e) XPS and (f) UV absorption spectra of SL-BGQDs. The inset in (f) shows photographs of the aqueous dispersion of SL-BGQDs with (right bottle) and without (left bottle) UV light radiation (365 nm).

can be indexed to bulk graphite.[170] SL-BGQDs exhibited a large Raman peak at 1574 cm^{-1} (G band) (Figure B.3 of Appendix B). The intensity ratio of the G to D bands was determined to be 1.1, indicating a high degree of graphitization since the signal of the ordered G band is similar to or slightly greater than the signal of the disordered D band.[171] A large number of defects are

also present in SL-BGQDs as evidenced by the Raman spectrum peak at 1345 cm^{-1} (D band); here the D band is activated by the destruction of the sp^2 hybridized graphene network due to sp^3 hybridized C atoms bonded to boron.[172]

An analysis of the surface elemental characteristics of SL-BGQDs by X-ray photoelectron spectroscopy (XPS) shows that carbon (68.175%), oxygen (28.404%), and boron (3.421%) are present on the surface of SL-BGQDs (Figure 6.1e). The XPS spectrum does not indicate the presence of any metal impurities, further confirming the metal-free nature of SL-BGQDs. In the expanded high-resolution XPS spectra (Figure B.4 of Appendix B), the C 1s peaks at 284.7, 286.2, and 288.6 eV are assigned to carbon atoms in the form of C−C (sp^3)/C=C (sp^2), C−O (sp^3), and O−C=O (sp^2), respectively.[173] The O 1s peaks at 532.1, 532.5, and 532.8 eV are associated with C=O quinone-type groups, C−OH phenol groups, and C−O−C ether groups, respectively.[174] The B 1s peaks at 191.2 and 191.6 eV are attributed to sp^2 C=B bonds.[175,176] In addition, the B 1s peak at 192.4 eV is associated with B−O bonds.[177] The peaks at 191.2 and 191.6 eV further provide the evidence of boron doping in SL-BGQDs.

The UV absorption spectrum (Figure 6.1f) of SL-BGQDs shows an absorption peak at ∼239 nm resulting from the $\pi-\pi^*$ transition of aromatic domains in SL-BGQDs.[178] A shoulder peak at 266 nm is also observed, which is attributed to the $n-\pi^*$ transition of carbonyl groups (C=O bonds) and the characteristic absorption peak of GQDs, which confirms the presence of functional groups.[179] When aqueous dispersions of SL-BGQDs were exposed to UV light (365 nm), blue light was emitted from the dispersions (inset in Figure 6.1f). The excitation wavelength-tunable, upconverted fluorescence (Figure B.5 of Appendix B) from SL-BGQDs confirms their quantum confinement effect.[180] Fourier transform infrared (FT-IR) spectroscopy was used to evaluate additional surface properties of SL-BGQDs (Figure B.6 of Appendix B). FT-IR absorption peaks at 3416 cm^{-1} and 1714 cm^{-1} correspond to −OH and C=O stretching modes, respectively; these peaks indicate the presence of hydroxyl and carboxyl groups on SL-BGQDs, which endows them with good water-solubility.[181]

Magnetic properties of SL-BGQDs were assessed with a superconducting quantum interference device. Figure 6.2a shows the magnetization hysteresis loop for SL-BGQDs measured at

a temperature of 6 K in the field range of -10 kOe $< H < +10$ kOe, from which the saturation of magnetization is identified at $M_s = 0.121$ emu g^{-1} after subtracting the diamagnetic background. The saturation of magnetization at 300 K for SL-BGQDs was similarly identified to be $M_s = 0.197$ emu g^{-1} (Figure 6.2b), which also indicates that SL-BGQDs have a very weak ferromagnetic ordering at room temperature. The magnetic properties of SL-BGQDs result from the breaking of π-bonds in boron-doped GQDs due to missing C atoms, which induces unpaired electrons and partial spin polarization in SL-BGQDs.[182] Importantly, the boron atoms in SL-BGQDs provide paramagnetic centers for T1-weighted MR imaging since localized doping produces local magnetic moments and spins of dangling bonds (B$-$C bond).

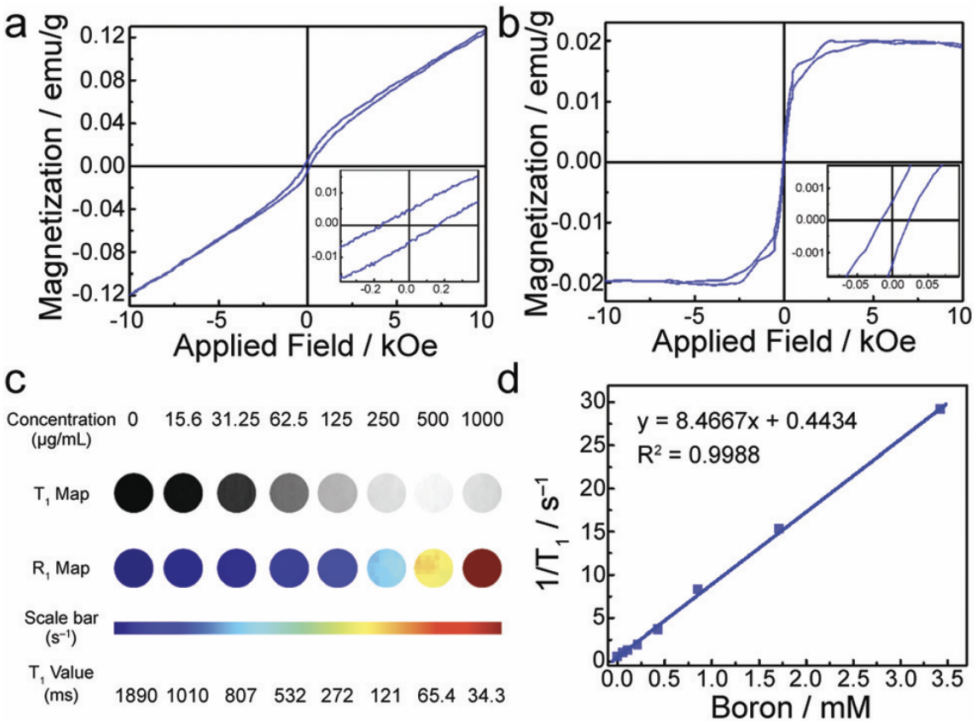

Figure 6.2: Magnetic properties and in vitro MR imaging of SL-BGQDs. (a and b) Magnetization hysteresis loops of SL-BGQDs at (a) 6 K and (b) 300 K in the range of -10 kOe $< H < +10$ kOe. The insets in (a) and (b) are the magnetization hysteresis loops expanded around 0 applied field. (c) T1-weighted MR images and quantitative R1 maps of SL-BGQDs at different SL-BGQD concentrations. (d) Plot of $^1/_{T_1}$ (R1) as a function of the boron concentration in SL-BGQDs. The slope of the curve is defined as the longitudinal relaxivity, r_1.

To evaluate the applicability of using SL-BGQDs as contrast agents for MR imaging, quantitative T1 and T1-weighted MR imaging scan sequences were acquired of SL-BGQD samples in phosphate buffered saline (PBS) at a magnetic field strength of 14 T. As shown in Figure 6.2c, the T1-weighted signal intensity increases with increasing SL-BGQD concentration (i.e., an increase in boron concentration). Next, $^1/_{T1}$ was plotted against the boron molar concentration in SL-BGQDs (Figure 6.2d). The relaxation rate R1 ($= {}^1/_{T1}$) exhibits a linear relationship with boron molar concentration, and the longitudinal relaxivity, r_1 (the slope of the best fit line in this linear relation) of SL-BGQDs was evaluated to be 8.5 mM^{-1} s^{-1} (Figure 6.2d). A concentration-dependent negative signal enhancement effect was clearly observed for a T2-weighted MR scan sequence (Figure B.7 of Appendix B), and the r_2 value of SL-BGQDs was determined to be 9.2 mM^{-1} s^{-1} based on the linear relation between the transverse relaxation and boron molar concentrations (Figure B.8 of Appendix B).

Two design principles regulate the development of T1 contrast agents: (i) r_1 should be large ($r_1 > 5$ mM^{-1} s^{-1}) and (ii) the ratio of r_2 to r_1 should be small $^{r_2}/_{r_1} < 5$).[155,167,183,184] Throughout the development of SL-BGQDs as T1 contrast agents, we compared the relaxivity values and qualitative in vitro MR imaging results to the gold standard clinical T1 contrast agent: Gd-DTPA. As shown in Figure B.9 of Appendix B, the r_1 and r_2 relaxivities of Gd-DTPA were measured to be 4.3 mM^{-1} s^{-1} and 5.03 mM^{-1} s^{-1}, respectively, which yields $^{r_2}/_{r_1} = 1.17$. The r_1 of SL-BGQDS (Figure 6.2)d is $r_1 = 8.5$ mM^{-1} s^{-1}, about two times greater than that of Gd-DTPA, and the $^{r_2}/_{r_1}$ ratio of SL-BGQDs is 1.08, slightly smaller (i.e., better) than that of Gd-DTPA.

The ability of SL-BGQDs to serve as T1 contrast agents was assessed in vivo with a 14 T MR imaging system using a C57Bl/6 wild-type mouse model. 200 μL of SL-BGQDs (1 mg mL^{-1}) dispersed in PBS solution was administered via intravenous injection. As a reference, MR images were also acquired from mice similarly treated with Gd-DTPA (200 μL, 1 mg mL^{-1}). T1-weighted MR images of the cross-sectional views of mice centered within the abdomen were acquired before and after contrast agent injection. As shown in Figure 6.3a (showing the posterior abdomen) and Figure B.10 of Appendix B, showing the anterior abdomen), both SL-BGQDs and Gd-DTPA demonstrated a substantial signal enhancement in renal cortex (RC), renal pelvis (RP), and gall

bladder (GB) as evidenced by comparing their pre-injection and post-injection images. In addition, SL-BGQDs demonstrated slightly better signal enhancement in the liver and spleen compared to Gd-DTPA. The contrast enhancement provided by Gd-DTPA peaked within the first 10 min post-injection, but rapidly declined between the 20 and 30 min post-injection imaging time points, and the observed contrast enhancement completely faded out 60 min after injection. SL-BGQDs demonstrated greater T1-weighted contrast enhancement (i.e., brighter post-injection regions of interest) as well as a prolonged hyperintensive T1-weighted signal in most of the organs analyzed (e.g., kidneys, liver, and spleen). These qualitative observations were corroborated by quantitative analysis of the measured MR signal strength pre- and post-injection (Figure 6.3b and c). The change in T1-weighted signal between pre- and post-injection images in the liver and spleen of mice treated with SL-BQGDs at 60 min post-injection increased by 232.8% and 207.6%, respectively. In contrast, no T1-weighted signal increase was detected in any organ in mice injected with Gd-DTPA at 60 min post-injection as compared to pre-injection signals.

To further evaluate the efficacy of SL-BGQDs as an in vivo T1 contrast agent, we performed cranial MR imaging to acquire a map of the neurovasculature of a mouse. Images of the entire head were acquired using a T1-weighted MR scan sequence prior to and 10 min after injection of 200 μL, 5 mg mL^{-1} of either SL-BGQDs or Gd-DTPA. Figure 6.4 shows the maximum intensity projections of representative pre- and post-injection images from mice receiving SL-BGQD (Figure 6.4a and b) or Gd-DTPA (Figure 6.4c and d). Cranial blood vessels could hardly be identified in pre-injection images for either group. Conversely, the vascular structures were clearly seen after SL-BGQD administration; the great cerebral vein was seen in the post-injection sagittal view (yellow arrow) and the superior sagittal sinus was evident in the post-injection coronal view (red arrow). Mice receiving Gd-DTPA with a dose identical to that of SL-BGQD showed no apparent change in contrast between pre- and post-injection images. The great positive contrast enhancement provided by SL-BGQDs is attributed to their high r_1 value.

To evaluate the BBB permeability of SL-BGQDs, a property that is essential for neurological imaging, wild-type mice were intravenously injected with SL-BGQDs. Brain sections of the mice were histologically analyzed 1 h post-injection. Tissue sections were stained with anti-CD31 an-

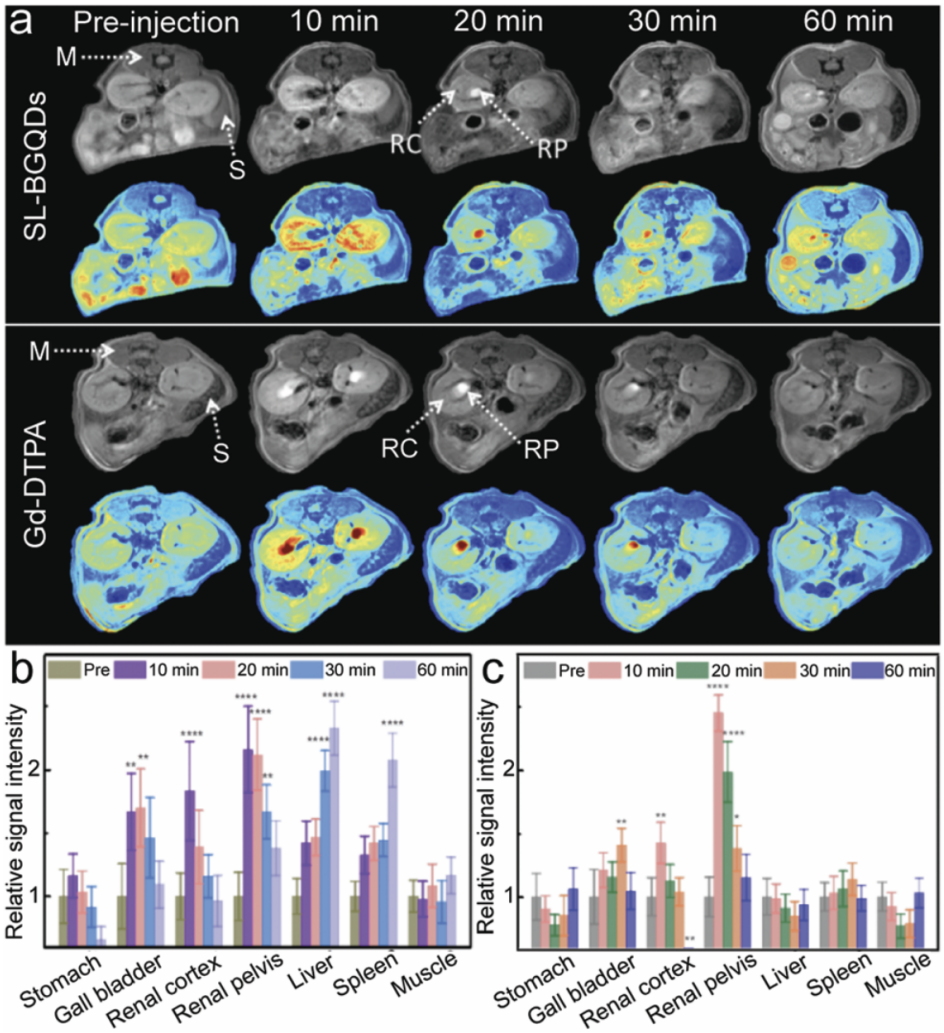

Figure 6.3: In vivo abdominal MR imaging of mice intravenously administered with SL-BGQDs or Gd-DTPA. (a) T1-weighted MR images of the cross-sections of mice receiving SL-BGQDs (upper panel) or Gd-DTPA (lower panel) treatments acquired using dynamic time-resolved MR imaging at various time points post-injection. Both grayscale and colorized images are displayed for experimental groups. The arrows point to various organs: muscle (M), spleen (S), renal cortex (RC), and renal pelvis (RP). (b and c) Relative T1-weighted signal intensity in mice injected intravenously with (b) SL-BGQDs or (c) Gd-DTPA, acquired with dynamic time-resolved MR imaging of organs of interest before and at different time points after the administration of contrast agents. One-way and two-way analyses of variance followed by Tukey's or Sidak's post hoc multiple comparison tests were used for comparison of multiple groups. ($^{*}p < 0.05$, $^{**}p < 0.01$, $^{***}p < 0.001$, $^{****}p < 0.0001$).

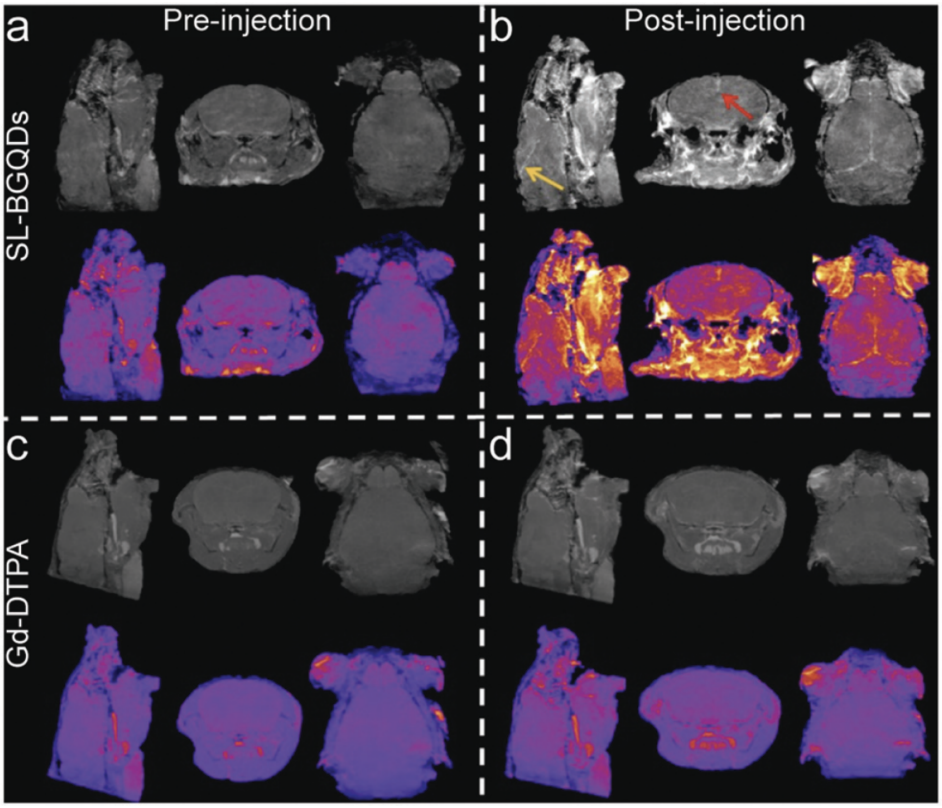

Figure 6.4: In vivo cranial MRI. T1-weighted MR images of the cross-sections of mice receiving either SL-BGQD (a and b) or Gd-DTPA (c and d) treatment prior to (left panels) and 10 min after (right panels) intravenous injection of contrast agent. The yellow arrow denotes the great cerebral vein, and the red arrow denotes the superior sagittal sinus.

tibody for visualization of endothelial blood vessels and with DAPI for cell nuclei visualization. Brain tissues from PBS-treated mice as a control showed no fluorescence signal 1 h post injection (Figure 6.5a−d). In contrast, brain tissues of mice intravenously injected with SL-BGQDs exhibited red fluorescence 1 h post-injection (Figure 6.5e−h), confirming that SL-BGQDs bypassed the BBB and accumulated in the brain tissues of live mice. We speculate that the nanoparticle-induced endothelial leakiness (NanoEL) effect[19,185] may be the primary mechanism by which SL-BGQDs penetrated the BBB.

To assess the cytotoxicity of SL-BGQDs, three tumor cell lines (4T1, SF763, and B16F10) were treated with either SL-BGQD or Gd-DTPA for 72 h, and cell viability was assessed using the Alamar Blue assay. Cells treated with PBS were used as a control. No cytotoxicity of SL-BGQDs

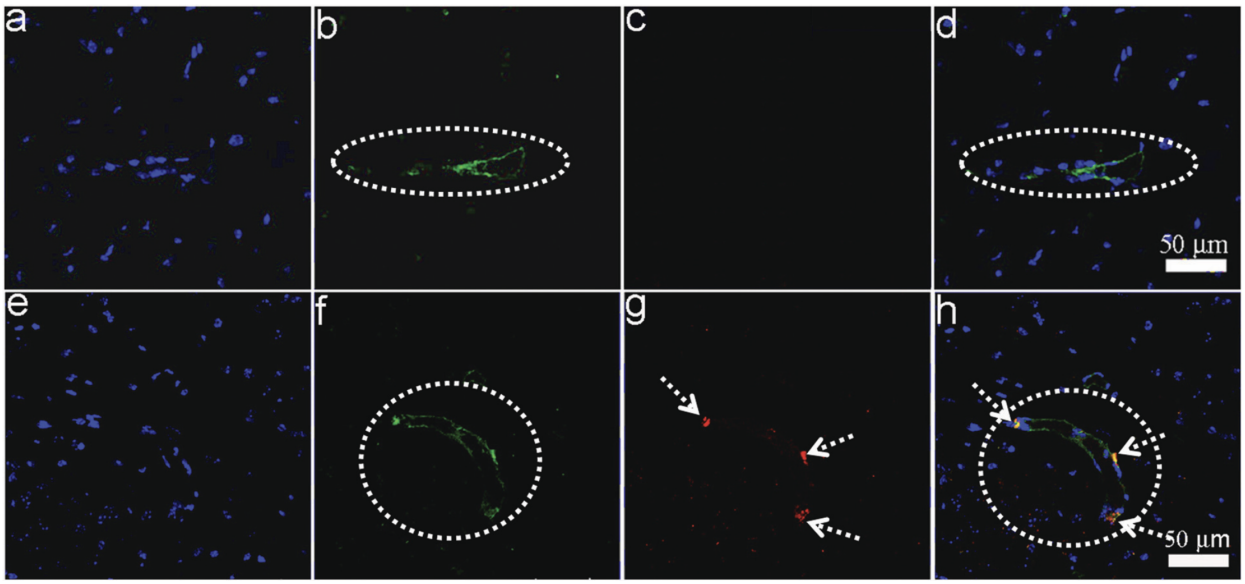

Figure 6.5: SL-BGQDs traversing the BBB. Confocal fluorescence microscopy of mouse brain tissue sections acquired 1 h after mice received injection of PBS (a-d) and SL-BGQDs (e-h). (a and e) Cell nuclei stained with DAPI (blue); (b and f) endothelial cells stained with anti-CD31 antibody (green); (c and g) SL-BGQDs fluoresce red (indicated with white arrows) when excited with a 650 nm laser; (d and h) overlaid images of mouse brain tissues from a-c and e-g, respectively. Blood vessels are encircled with white dashed lines.

or Gd-DTPA were found in any of the three tumor cell lines (Figure B.11 of Appendix B); more than 87% of cells from all cell lines survived 72 h after being treated with either SL-BGQDs or Gd-DTPA at concentrations up to 200 µg mL^{-1}. These results were normalized as a percentage of cells incubated with PBS for 72 h (control) to determine cell viability.

Tissue compatibility of SL-BGQDs was evaluated in vivo by histological analysis in wild-type mice. Various tissues (liver, spleen, lungs, and kidneys) were harvested from mice treated by intravascular injection of either SL-BGQDs, Gd-DTPA, or PBS solution (control) 72 h post-treatment and stained with hematoxylin and eosin (H&E) (Figure B.12 of Appendix B). The study found no sign of a toxicity response in mice treated with either SL-BGQDs or Gd-DTPA agents, as healthy cell morphology was retained after treatment in all organs of interest and in all experimental groups. Further, tissue sections from the same organs were stained with DAPI and examined by fluorescence microscopy (Figure B.13 of Appendix B), and no abnormality in nuclear morphology was found for any of these experimental groups. These results confirm that both SL-BGQDs and

Gd-DTPA have no acute toxicity to the organs and tissues examined.

Hematological toxicity was assessed for both SL-BGQDs and Gd-DTPA with PBS as a non-toxic reference control. As shown in Figure 6.6a, the white blood cell (WBC) count of Gd-DTPA-treated mice was significantly lower than those from PBS-treated (control) and SL-BGQD-treated animals and are outside of the typical range for mice (reference range $= 2-10 \times 10^3$ cells per μL);[186] the drop in WBC count in Gd-DTPA-treated mice is indicative of a stress-induced immune response.[186] Two key liver enzymes associated with hepatoxicity, aspartate transaminase (AST) and alanine aminotransferase (ALT), were monitored in these mice (Figure 6.6b). Only the Gd-DTPA-treated mice exhibited a marked increase in ALT-to-AST ratio, which is indicative of hepatic injury.[187] In addition to histological staining and hematological analysis, quantitative reverse transcription polymerase chain reaction was used to detect alterations in transcription levels for genes associated with the endoplasmic reticulum stress response (bip, chop, IL-b, TNF-a, and xbp). Figure 6.6c and d compare mRNA expression in the kidneys and liver between mice treated with SL-BGQDs and those treated with Gd-DTPA assessed 24 h post-treatment; the gene expression levels were compared with gene expressions from mice injected with PBS. Gene expression levels were observed to be normal in mice treated with SL-BGQDs in the kidneys and liver. Conversely, mice treated with Gd-DTPA expressed abnormally high levels of bip in the kidneys and liver, and abnormally low levels of chop, TNF-a, and xbp in the liver. Thus, Gd-DTPA was observed to cause a significant endoplasmic reticulum stress response, while SL-BGQDs were benign in this regard. These results indicate that SL-BGQDs may be a better treatment option than Gd-DTPA in terms of biocompatibility when used as contrast agents in clinical MR imaging applications.

6.3 Materials and Methods

6.3.1 Synthesis of SL-BGQDs

All chemicals were purchased from Sigma-Aldrich (St. Louis, MO, USA). VPBA (0.05 g) and boric acid (0.03 g) were dissolved in 20 mL acetone and 5 mL ethanol. After intense sonication for 30 min, 10.0 mL of H_2O_2 (30%) was slowly added to the solution. The solution was then ultrasoni-

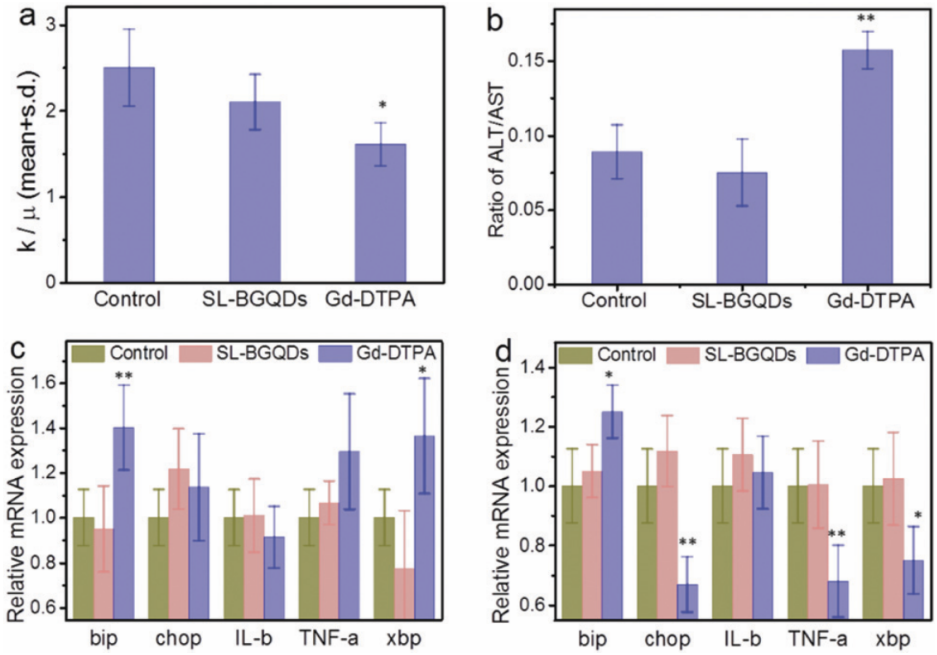

Figure 6.6: Toxicity assessment of SL-BGQDs and Gd-DTPA on key enzymes and genes of the liver and kidneys. (a) WBC counts of mice receiving PBS (control), SL-BGQD, or Gd-DTPA injection, measured 24 h after administration. (b) Liver enzyme ratio of ALT to AST. (c and d) Gene expressions of (c) kidney and (d) liver from mice treated with PBS (control), SL-BGQD, or Gd-DTPA. Data are presented as mean $\pm$ the standard deviation of the mean ($n = 4$ mice per treatment). One-way and two-way analyses of variance followed by Tukey's or Sidak's post hoc multiple comparison tests were used for comparisons of multiple groups. ($^{*}p < 0.05$, $^{**}p < 0.01$).

cated for 10 min and transferred into a 50 mL Teflon-lined, stainless-steel autoclave. This precursor solution was heated to and maintained at 205°C. After 24 h, the solution was cooled naturally to room temperature. The resultant solution was dialyzed for 3 days (Spectra/Per molecular porous membrane tubing, cutoff 14 kDa) at room temperature. The aqueous dispersion of SL-BGQDs was then collected and centrifuged at 14,800 rpm for 30 min with the supernatant discarded.

6.3.2 SL-BGQD Characterization

TEM and HR-TEM images were acquired on a Tecnai G2 F20 electron microscope (FEI, Hillsboro, OR) operating at a voltage of 200 kV. AFM was performed using a Veeco DI Nano-scope Multi-Mode V system. Powder XRD patterns were acquired from lyophilized samples using a D8 Bruker

X-ray diffractometer with Cu Kα radiation. UV-vis absorption spectra were obtained on a UV-vis spectrometer (Agilent Technologies, Santa Clara, CA). Magnetic properties were measured using a superconducting quantum interference device magnetometer (Quantum Design MPMS XL-7). The sample preparation process was performed using a non-metallic container. FT-IR spectra were acquired using a Nicolet 5-DXB FT-IR spectrometer with a resolution of 4 cm^{-1}. Raman spectra were taken on a Renishaw-InVia Raman microscope using a 514.5 nm Ar^{+} laser at room temperature. Photoluminescence spectra were obtained on a JOBIN YVON Co. FluoroMax-3 spectrofluorometer equipped with a Hamamatsu R928P photomultiplier tube. XPS experiments were conducted at the National ESCA and Surface Analysis Center at the University of Washington.

6.3.3 Penetration of the Blood-Brain Barrier by SL-BGQDs

All procedures involving animal models were performed in accordance with University of Washington Institutional Animal Care and Use Committee regulations. C57Bl/6 wild-type mice (Charles River Laboratories, Inc.) were euthanized 1 h post tail-vein injection with SL-BGQDs (dispersed in PBS, 200 µL, 1 mg mL^{-1}) or PBS (200 µL, control), and brain tissues were dissected. Tissues were preserved in 10% formalin for 48 h. Formalin-fixed tissue samples were first transferred from PBS to and maintained in 70% ethanol for 2 h and were then transferred into and maintained in 95% ethanol/5% methanol for an additional 2 h. Next, the samples were transferred to and maintained in absolute ethanol for 1 h and then transferred again into and maintained in 3 consecutive absolute xylene solutions, each for 1 h. After a dehydration step, the samples were placed in 2 consecutive melted paraffin baths, each for 2 h. The paraffin-penetrated samples were then embedded in paraffin blocks, sectioned at 10 µm thickness, and loaded onto microscope slides. The loaded slides were first heated to remove excess paraffin and adhere the samples to the slides. Subsequently, the samples were deparaffinized by a series of xylene, ethanol, and PBS baths. Slides were then rinsed and stained with DAPI and anti-CD31 antibody for 15 min at room temperature. Coverslips were then mounted onto microscope slides using Prolong Gold Antifade Mountant. Images were acquired on a Leica SP8X confocal laser scanning microscope.

6.3.4 Viability of Cells Treated with SL-BGQDs or Gd-DTPA

4T1, SF763, and B16F10 cells were seeded in a 96-well plate and incubated overnight in the Dulbecco's Modified Eagle Medium (DMEM). On the following day, the medium was replaced with a medium containing SL-BGQDs, Gd-DTPA, or with PBS (control). Three concentrations of SL-BGQDs or Gd-DTPA (200, 150, and 100 μg mL^{-1}) were used, and samples at each concentration were ran in sextuplicate. Cells were incubated with SL-BGQDs, Gd-DTPA, or PBS for 72 h. Cell viability was assessed using the Alamar Blue assay. Briefly, medium was replaced with cell culture medium containing the Alamar Blue reagent and incubated for 2 h. Following incubation, a microplate reader (SpectraMax i3, Molecular Devices, Sunnyvale, CA) was used to determine the fluorescence intensity of SL-BGQDs or Gd-DTPA. The fluorescence intensity from SL-BGQD- or Gd-DTPA-treated cells was normalized to the intensity from PBS-treated control cells to determine percent viability.

6.3.5 Histopathological Evaluation and Nucleus Morphology Evaluation of Organs of Mice Treated with SL-BGQDs or Gd-DTPA

Five days after receiving no injection (control) or tail-vein injection of SL-BGQD or Gd-DTPA at a concentration of 5 mg mL^{-1} (dispersed in PBS), the C57Bl/6 wild-type mice (Charles River Laboratories, Inc.) were euthanized and whole organs (kidneys, liver, lung, and spleen) were removed and preserved in 10% formalin for 48 h. Tissues were then embedded in paraffin, sliced into 5 μm sections, and stained with hematoxylin and eosin (H&E). Microscopic images of tissues were acquired using a Nikon ECLIPSE TE2000-S microscope.

Tissue slide samples were prepared in a similar fashion as those for H&E staining. The samples were deparaffinized and then processed with DAPI staining. The samples were then viewed under a microscope to visualize for any abnormal nucleus morphology.

6.3.6 Hematology Assay

Twenty-four h after mice were tail-vein injected with SL-BGQDs or Gd-DTPA at a concentration of 5 mg mL^{-1} (dispersed in PBS), 3mL of blood was drawn from C57Bl/6 wild-type mice ($n = 4$) via the cardiac puncture method after terminal deep anesthesia. Animals receiving PBS injection ($n = 4$) were used as controls. Collected samples were sent to the Laboratory Medicine Research Testing Service at the University of Washington for chemical and phlebotomy analyses.

6.3.7 RT-PCR Assay

Twenty-four h after mice were tail-vein injected with SL-BGQDs or Gd-DTPA at a concentration of 5 mg mL^{-1} (dispersed in PBS), 20 mg of each harvested tissue from each contrast agent-treated mouse was flash-frozen using liquid nitrogen and ground into a fine powder. The powders were then transferred into microfuge tubes and treated with RNeasy Plus Mini kit (Qiagen, Germany) for the extraction of mRNA. RT-PCR was carried out following the mRNA extraction process using the following primer sets:

Target genes	Forward primer	Reverse primer
xbp-1s	5′-TGCTGAGTCCGCAGCAGGTG-3′	5′-GACTAGCAGACTCTGGGGAAGG-3′
chop	5′-CATACACCACCACACCTGAAAG-3′	5′-CCGTTTCCTAGTTCTTCCTTGC-3′
bip	5′-GAAAGGATGGTTATGATGCTGAG-3′	5′-GTCTTCAATGTCCGCATCCTG-3′
IL-1B	5′-ATGGCAACTGTTCCTGAACTCAAC-3′	5′-CAGGACAGGTATAGATTCTTTCC-3′
TNF-a	5′-ACGTGGAACTGGCAGAAGAG-3′	5′-CTCCTCCACTTGGTGGTTTG-3′
Gapdh	5′-GACTTCAACAGCAACTCCCAC-3′	5′-TCCACCACCCTGTTGCTGTA-3′

The expression of genes was then quantified relative to the expression level of Gapdh.

6.3.8 In Vitro MR Imaging

T1- and T2-weighted imaging and quantitative T1 and T2 MR imaging scan sequences were used to investigate the contrast enhancing capabilities of SL-BGQDs. MR imaging was conducted on a Bruker Avance III 600 MHz, 14 T vertical-bore spectrometer. Either SL-BGQDs or Gd-DTPA

samples in PBS were pipetted into glass vials (3.25 mm I. D., 5 mm O. D., 200 μL volume). The vials were fixed in place inside a water reservoir; the water served as a homogeneous background signal to minimize magnetic susceptibility variations near samples. The secured vials were placed in a 25 mm single-channel ^{1}H radiofrequency receive coil (PB Micro 2.5). Relaxation properties of SL-BGQDs and Gd-DTPA were evaluated with a quantitative T1 rapid imaging with refocused echoes and variable repetition time (RARE-VTR) pulse sequence with an echo time (TE) of 12.0 ms, TR = 80 ms, 400 ms, 800 ms, 1600 ms, 3000 ms, 6000 ms, 8000 ms, and 12000 ms, 180×180 μm^2 in-plane resolution, and 5.0 mm slice thickness for one slice. Quantitative T2 values were measured using a multi-spin multi-echo (MSME) pulse sequence with TR = 2500 ms, TE = $6.7 + 6n$ ms ($n = 0 - 16$), and 78×156 μm^2 in-plane resolution with 0.5 mm slice thickness for 14 slices. T1-weighted images were acquired with a RARE pulse sequence with TE = 5.49 ms, TR = 531 ms, 78×52 μm^2 in-plane resolution and 0.5 mm slice thickness for 10 slices. T2-weighted images were acquired with a RARE pulse sequence with TE = 6.78 ms, TR = 4000 ms, and 78×52 μm^2 in-plane resolution with 0.5 mm slice thickness for 14 slices. Analysis of MR imaging data was accomplished with the FMRIB software library (FSL), Paravision 5.1 analysis package (Bruker), and ImageJ (NIH). T1 values were determined within a circular, 100-voxel region of interest.

6.3.9 In Vivo MR Imaging

Ninety min sequential T1-weighted imaging was performed over the abdominal regions of C57Bl/6 wild-type mice prior to and after mice were injected with SL-BGQDs (200 μL, 5 mg mL^{-1}) or Gd-DTPA (200 μL, 5 mg mL^{-1}), using a Bruker Avance III 600 MHz, 14 T vertical-bore imaging system. Similarly, 10 min sequential T1-weighted imaging was performed over the cranial regions of C57Bl/6 wild-type mice prior to and after injection with SL-BGQDs (200 μL, 5 mg mL^{-1}) or Gd-DTPA (200 μL, 5 mg mL^{-1}). Mice were anesthetized with isoflurane (Piramal Healthcare) and secured in a coil-integrated respiratory monitoring system (SA Instruments; MR-compatible small animal monitoring and gating system) with nose-cone for oxygen/anesthetic, ear-bar head holder, circulating temperature control bath, and residual gas extraction. Abdominal scans were acquired using rapid acquisition with refocused echoes (RARE) T1-weighted (TR/TE

= 691/5.5 ms, in-plane resolution 93×62 μm^2, matrix 256×284) sequences with slices placed in the transverse plane with 0.5 mm slice thickness and 0.75 mm interslice gaps allowing for coverage from the liver to the pelvic floor. Cranial scans were acquired over the entire head with a 3-dimensional, T1-weighted fast low angle shot (FLASH) scan sequence (TR/TE = 16.2/2.7 ms, resolution $106 \times 108 \times 152$ μm^3, matrix $284 \times 186 \times 132$). Images presented resulting from this cranial scan sequence were processed using a maximum intensity projection with a 3 mm slab thickness.

6.4 Conclusions

We developed single-layer, metal-free, boron-doped GQDs as contrast agents for T1-weighted MR imaging. Compared to our previous efforts at synthesizing boron-doped GQDs in order to create MR contrast agents,[165] we have made significant improvements in this study with respect to the contrast-enhancing capabilities of GQDs by fine-tuning the synthesis procedure to ensure a single-layered product as opposed to a multi-layered GQD ensemble. The single-layered nature of SL-BGQDs imbues them with improved magnetic properties for T1-weighted MR imaging compared to multi-layered boron-doped GQDs. SL-BGQDs demonstrated an excellent r_2/r_1 ratio (1.08). Furthermore, we have provided a more comprehensive experimental verification of the ability of SL-BGQDs to serve as MR contrast agents in vivo. Significantly, our findings reveal that, at equivalent and relevant doses for MR imaging applications, SL-BGQDs exhibit a more stable safety profile than a clinically used Gd-based T1 contrast agent. Finally, we demonstrated that SL-BGQDs can pass the BBB and have a prolonged imaging time ($\sim$60 min) as compared to Gd-DTPA ($\sim$10 min), enabling the diagnosis of brain tumors and injuries. This well-characterized metal-free SL-BGQD contrast agent may serve as a safer, improved alternative to Gd-based contrast agents for T1-weighted MR imaging in clinical applications.

Chapter 7

SUMMARY OF MAJOR FINDINGS

Nanomedicine, and iron oxide nanoparticles (NPs) in particular, have the potential to improve the lives of those suffering from disease by providing advanced diagnostic capabilities and enhanced therapeutic outcomes. The goal of this thesis was to progress the state of the research space occupied by iron oxide NPs closer to the clinic through carefully designed investigations into their use as contrast agents for magnetic resonance imaging (MRI) and in a therapeutic capacity by enhancing radiotherapy.

A cross-species comparison of the biokinetics of iron oxide NPs coated with a siloxane poly(ethylene glycol) monolayer between mice and nonhuman primates as tracked using MRI was provided in Chapter 3. These NPs were shown to behave similarly between mice and macaques with respect to uptake and washout in the organs of the blood, liver, spleen, and muscle, but differently in the organs of kidney, brain, and bone marrow. The ability of iron oxide NPs to be visualized with MRI was extended to the evaluation of NP diffusion in convection-enhanced delivery (CED) of NPs to mice-bearing orthotopic brain tumors in Chapter 4. Two NP experimental groups were compared, wherein the same base NP formulation was produced in two formats: bare NP and NP conjugated with the tumor-targeting peptide chlorotoxin. Targeted NPs exhibited a 3.4-fold increase in the volume of distribution throughout the tumor 24 h post-CED compared to bare NPs followed by prolonged suffusion throughout the tumor as evidence in the MRI images captured 48 h post-CED.

Chapter 5 presented a novel therapeutic use of iron oxide NPs where the iron cores were exploited for enhanced absorption of incident ionizing radiation for the treatment of mice-bearing glioblastoma. Compared to mice receiving radiotherapy alone, mice injected with iron oxide NPs prior to radiotherapy experienced a 2-fold improvement in median survival and a 3-fold slower tumor growth rate.

Finally, Chapter 6 detailed the design and use of metal-free, boron-doped graphene quantum dots as T1 contrast agents for MRI. These nanomaterials were shown to have similar contrast enhancing abilities compared to the gadolinium-based clinical gold-standard contrast agent, Gd-DTPA, while exhibiting significantly less toxicity.

BIBLIOGRAPHY

[1] C. P. Wild, E. Weiderpass, and B. W. Stewart, Eds., *World Cancer Report: Cancer Research for Cancer Prevention*. Lyon, France: International Agency for Research on Cancer, 2020.

[2] F. Bray, J. Ferlay, I. Soerjomataram, R. L. Siegel, L. A. Torre, and A. Jemal, "Global cancer statistics 2018: Globocan estimates of incidence and mortality worldwide for 36 cancers in 185 countries," *CA: A Cancer Journal for Clinicians*, vol. 68, no. 6, pp. 394–424, 2018.

[3] J. H. Ryu, H. Koo, I.-C. Sun, S. H. Yuk, K. Choi, K. Kim, and I. C. Kwon, "Tumor-targeting multi-functional nanoparticles for theragnosis: New paradigm for cancer therapy," *Advanced Drug Delivery Reviews*, vol. 64, no. 13, pp. 1447–1458, 2012.

[4] V. Sanna, N. Pala, and M. Sechi, "Targeted therapy using nanotechnology: focus on cancer," *International Journal Of Nanomedicine*, vol. 9, no. 1, pp. 467–483, 2014.

[5] O. Veiseh, J. W. Gunn, and M. Zhang, "Design and fabrication of magnetic nanoparticles for targeted drug delivery and imaging," *Advanced Drug Delivery Reviews*, vol. 62, no. 3, pp. 284–304, 2010.

[6] Y. Cheng, R. A. Morshed, B. Auffinger, A. L. Tobias, and M. S. Lesniak, "Multifunctional nanoparticles for brain tumor imaging and therapy," *Advanced Drug Delivery Reviews*, vol. 66, pp. 42–57, 2014.

[7] F. M. Kievit and M. Zhang, "Surface Engineering of Iron Oxide Nanoparticles for Targeted Cancer Therapy," *Accounts of Chemical Research*, vol. 44, no. 10, pp. 853–862, 2011.

[8] C. Sun, K. Du, C. Fang, N. Bhattarai, O. Veiseh, F. Kievit, Z. Stephen, D. Lee, R. G. Ellenbogen, B. Ratner, and M. Zhang, "PEG-mediated synthesis of highly dispersive multifunctional superparamagnetic nanoparticles: their physicochemical properties and function in vivo," *ACS nano*, vol. 4, no. 4, pp. 2402–2410, 2010.

[9] R. Weissleder, D. D. Stark, B. L. Engelstad, B. R. Bacon, C. C. Compton, D. L. White, P. Jacobs, and J. Lewis, "Superparamagnetic iron oxide: pharmacokinetics and toxicity," *American Journal of Roentgenology*, vol. 152, no. 1, pp. 167–173, 1989.

[10] C. Sun, J. S. H. Lee, and M. Zhang, "Magnetic nanoparticles in MR imaging and drug delivery," *Advanced Drug Delivery Reviews*, vol. 60, no. 11, pp. 1252–1265, 2008.

[11] Z. R. Stephen, F. M. Kievit, and M. Zhang, "Magnetite nanoparticles for medical MR imaging," *Materials Today*, vol. 14, no. 7-8, pp. 330–338, 2011.

[12] Y. Gossuin, P. Gillis, A. Hocq, Q. L. Vuong, and A. Roch, "Magnetic resonance relaxation properties of superparamagnetic particles," *WIREs Nanomedicine and Nanobiotechnology*, vol. 1, no. 3, pp. 299–310, 2009.

[13] K. M. Krishnan, "Biomedical Nanomagnetics: A Spin Through Possibilities in Imaging, Diagnostics, and Therapy," *IEEE transactions on magnetics*, vol. 46, no. 7, pp. 2523–2558, 2010.

[14] H. Arami, A. Khandhar, D. Liggitt, and K. M. Krishnan, "In vivo delivery, pharmacokinetics, biodistribution and toxicity of iron oxide nanoparticles," *Chemical Society Reviews*, vol. 44, no. 23, pp. 8576–8607, 2015.

[15] F. M. Kievit, Z. R. Stephen, O. Veiseh, H. Arami, T. Wang, V. P. Lai, J. O. Park, R. G. Ellenbogen, M. L. Disis, and M. Zhang, "Targeting of primary breast cancers and metastases in a transgenic mouse model using rationally designed multifunctional spions," *ACS Nano*, vol. 6, no. 3, pp. 2591–2601, 2012, pMID: 22324543.

[16] H. Maeda, J. Wu, T. Sawa, Y. Matsumura, and K. Hori, "Tumor vascular permeability and the EPR effect in macromolecular therapeutics: a review," *Journal of Controlled Release*, vol. 65, no. 1, pp. 271–284, 2000.

[17] D. Peer, J. M. Karp, S. Hong, O. C. Farokhzad, R. Margalit, and R. Langer, "Nanocarriers as an emerging platform for cancer therapy," *Nature Nanotechnology*, vol. 2, no. 12, pp. 751–760, 2007.

[18] G. Subbiahdoss, S. Sharifi, D. W. Grijpma, S. Laurent, H. C. van der Mei, M. Mahmoudi, and H. J. Busscher, "Magnetic targeting of surface-modified superparamagnetic iron oxide nanoparticles yields antibacterial efficacy against biofilms of gentamicin-resistant staphylococci," *Acta Biomaterialia*, vol. 8, no. 6, pp. 2047–2055, 2012.

[19] F. Peng, M. I. Setyawati, J. K. Tee, X. Ding, J. Wang, M. E. Nga, H. K. Ho, and D. T. Leong, "Nanoparticles promote in vivo breast cancer cell intravasation and extravasation by inducing endothelial leakiness," *Nature Nanotechnology*, vol. 14, no. 3, pp. 279–286, 2019.

[20] K. Astanina, Y. Simon, C. Cavelius, S. Petry, A. Kraegeloh, and A. K. Kiemer, "Superparamagnetic iron oxide nanoparticles impair endothelial integrity and inhibit nitric oxide production," *Acta Biomaterialia*, vol. 10, no. 11, pp. 4896–4911, 2014.

[21] M. I. Setyawati, C. Y. Tay, and D. T. Leong, "The gap between endothelial cells: key to the quick escape of nanomaterials?" *Nanomedicine*, vol. 9, no. 11, pp. 1591–1594, 2014.

[22] C. Y. Tay, M. I. Setyawati, J. Xie, W. J. Parak, and D. T. Leong, "Back to Basics: Exploiting the Innate Physico-chemical Characteristics of Nanomaterials for Biomedical Applications," *Advanced Functional Materials*, vol. 24, no. 38, pp. 5936–5955, 2014.

[23] S. E. Song, B. K. Seo, K. R. Cho, O. H. Woo, G. S. Son, C. Kim, S. B. Cho, and S.-S. Kwon, "Computer-aided detection (CAD) system for breast MRI in assessment of local tumor extent, nodal status, and multifocality of invasive breast cancers: preliminary study," *Cancer imaging : the official publication of the International Cancer Imaging Society*, vol. 15, no. 1, p. 1, 2015.

[24] G. M. Thurber, J.-L. Figueiredo, and R. Weissleder, "Detection limits of intraoperative near infrared imaging for tumor resection," *Journal of Surgical Oncology*, vol. 102, no. 7, pp. 758–764, 2010.

[25] R. Hao, R. Xing, Z. Xu, Y. Hou, S. Gao, and S. Sun, "Synthesis, Functionalization, and Biomedical Applications of Multifunctional Magnetic Nanoparticles," *Advanced Materials*, vol. 22, no. 25, pp. 2729–2742, 2010.

[26] Y.-E. L. Koo, G. R. Reddy, M. Bhojani, R. Schneider, M. A. Philbert, A. Rehemtulla, B. D. Ross, and R. Kopelman, "Brain cancer diagnosis and therapy with nanoplatforms," *Advanced Drug Delivery Reviews*, vol. 58, no. 14, pp. 1556–1577, 2006.

[27] B. A. Ruggeri, F. Camp, and S. Miknyoczki, "Animal models of disease: Pre-clinical animal models of cancer and their applications and utility in drug discovery," *Biochemical Pharmacology*, vol. 87, no. 1, pp. 150–161, 2014.

[28] R. K. Jain and T. Stylianopoulos, "Delivering nanomedicine to solid tumors," *Nature Reviews Clinical Oncology*, vol. 7, no. 11, pp. 653–664, 2010.

[29] M. E. Davis, Z. G. Chen, and D. M. Shin, "Nanoparticle therapeutics: an emerging treatment modality for cancer," *Nature Reviews Drug Discovery*, vol. 7, no. 9, pp. 771–782, 2008.

[30] A. Kroll, M. H. Pillukat, D. Hahn, and J. Schnekenburger, "Current in vitro methods in nanoparticle risk assessment: Limitations and challenges," *European Journal of Pharmaceutics and Biopharmaceutics*, vol. 72, no. 2, pp. 370–377, 2009.

[31] N. Singh, G. J. S. Jenkins, R. Asadi, and S. H. Doak, "Potential toxicity of superparamagnetic iron oxide nanoparticles (SPION)," *Nano Reviews*, vol. 1, no. 1, p. 5358, 2010.

[32] S. Arora, J. M. Rajwade, and K. M. Paknikar, "Nanotoxicology and in vitro studies: The need of the hour," *Toxicology and Applied Pharmacology*, vol. 258, no. 2, pp. 151–165, 2012.

[33] M. Singh, C. Murriel, and L. Johnson, "Genetically Engineered Mouse Models: Closing the Gap between Preclinical Data and Trial Outcomes," *Cancer Research*, vol. 72, no. 11, pp. 2695–2700, 2012.

[34] A. P. Khandhar, R. M. Ferguson, H. Arami, and K. M. Krishnan, "Monodisperse magnetite nanoparticle tracers for in vivo magnetic particle imaging," *Biomaterials*, vol. 34, no. 15, pp. 3837–3845, 2013.

[35] A. C. Faure, S. Dufort, V. Josserand, P. Perriat, J. L. Coll, S. Roux, and O. Tillement, "Control of the in vivo Biodistribution of Hybrid Nanoparticles with Different Poly(ethylene glycol) Coatings," *Small*, vol. 5, no. 22, pp. 2565–2575, 2009.

[36] T. K. Jain, M. K. Reddy, M. A. Morales, D. L. Leslie-Pelecky, and V. Labhasetwar, "Biodistribution, clearance, and biocompatibility of iron oxide magnetic nanoparticles in rats," *Molecular Pharmaceutics*, vol. 5, no. 2, pp. 316–327, 2008.

[37] A. Al Faraj, G. Lacroix, H. Alsaid, D. Elgrabi, V. Stupar, F. Robidel, S. Gaillard, E. Canet-Soulas, and Y. Crémillieux, "Longitudinal 3 He and proton imaging of magnetite biodistribution in a rat model of instilled nanoparticles," *Magnetic Resonance in Medicine*, vol. 59, no. 6, pp. 1298–1303, 2008.

[38] K. Dassler, F. Roohi, J. Lohrke, A. Ide, S. Remmele, J. Hütter, H. Pietsch, U. Pison, and G. Schütz, "Current limitations of molecular magnetic resonance imaging for tumors as evaluated with high-relaxivity CD105-specific iron oxide nanoparticles," *Investigative Radiology*, vol. 47, no. 7, pp. 383–391, 2012.

[39] P.-W. Lee, S.-H. Hsu, J.-J. Wang, J.-S. Tsai, K.-J. Lin, S.-P. Wey, F.-R. Chen, C.-H. Lai, T.-C. Yen, and H.-W. Sung, "The characteristics, biodistribution, magnetic resonance imaging and biodegradability of superparamagnetic core-shell nanoparticles," *Biomaterials*, vol. 31, no. 6, pp. 1316–1324, 2010.

[40] D. Hoffman, M. Sun, L. Yang, P. R. Mcdonagh, F. Corwin, G. Sundaresan, L. Wang, V. Vijayaragavan, C. Thadigiri, N. Lamichhane, and J. Zweit, "Intrinsically radiolabelled (59)Fe-SPIONs for dual MRI/radionuclide detection," *American Journal of Nuclear Medicine and Molecular Imaging*, vol. 4, no. 6, pp. 548–560, 2014.

[41] S. H. Crayton, D. R. Elias, A. Al Zaki, Z. Cheng, and A. Tsourkas, "ICP-MS analysis of lanthanide-doped nanoparticles as a non-radiative, multiplex approach to quantify biodistribution and blood clearance," *Biomaterials*, vol. 33, no. 5, pp. 1509–1519, 2012.

[42] A. Ruiz, Y. Hernandez, C. Cabal, E. Gonzalez, S. Veintemillas-Verdaguer, E. Martinez, and M. P. Morales, "Biodistribution and pharmacokinetics of uniform magnetite nanoparticles chemically modified with polyethylene glycol," *Nanoscale*, vol. 5, no. 23, pp. 11 400–11 408, 2013.

[43] E. K. Schlachter, H. R. Widmer, A. Bregy, T. Lönnfors-Weitzel, I. Vajtai, N. Corazza, V. J. P. Bernau, T. Weitzel, P. Mordasini, J. Slotboom, G. Herrmann, S. Bogni, H. Hofmann, M. Frenz, and M. Reinert, "Metabolic pathway and distribution of superparamagnetic iron oxide nanoparticles: in vivo study," *International Journal of Nanomedicine*, vol. 6, pp. 1793–1800, 2011.

[44] A. Al Faraj, K. Cieslar, G. Lacroix, S. Gaillard, E. Canet-Soulas, and Y. Crémillieux, "In vivo imaging of carbon nanotube biodistribution using magnetic resonance imaging," *Nano Letters*, vol. 9, no. 3, pp. 1023–1027, 2009.

[45] Å. Barrefelt, M. Saghafian, R. Kuiper, F. Ye, G. Egri, M. Klickermann, T. B. Brismar, P. Aspelin, M. Muhammed, L. Dähne, and M. Hassan, "Biodistribution, kinetics, and biological fate of SPION microbubbles in the rat," *International Journal of Nanomedicine*, vol. 8, no. 1, pp. 3241–3254, 2013.

[46] F. Herodin, P. Thullier, D. Garin, and M. Drouet, "Nonhuman primates are relevant models for research in hematology, immunology and virology," *European Cytokine Network*, vol. 16, no. 2, pp. 104–116, 2005.

[47] C. Fang, N. Bhattarai, C. Sun, and M. Zhang, "Functionalized Nanoparticles with Long-Term Stability in Biological Media," *Small*, vol. 5, no. 14, pp. 1637–1641, 2009.

[48] J. Park, K. An, Y. Hwang, J.-G. Park, H.-J. Noh, J.-Y. Kim, J.-H. Park, N.-M. Hwang, and T. Hyeon, "Ultra-large-scale syntheses of monodisperse nanocrystals," *Nature Materials*, vol. 3, no. 12, pp. 891–895, 2004.

[49] A. Prantner and N. Scholler, "Biological Barriers and Current Strategies for Modifying Nanoparticle Bioavailability," *Journal Of Nanoscience And Nanotechnology*, vol. 14, no. 1, pp. 115–125, 2014.

[50] Y.-w. Jun, J.-S. Suh, J. Cheon, Y.-M. Huh, J.-S. Shin, J.-s. Choi, K.-S. Kim, J.-H. Lee, S. Yoon, H.-T. Song, and S. Kim, "Nanoscale size effect of magnetic nanocrystals and their utilization for cancer diagnosis via magnetic resonance imaging," *Journal of the American Chemical Society*, vol. 127, no. 16, pp. 5732–5733, 2005.

[51] M. Longmire and H. Kobayashi, "Clearance properties of nano-sized particles and molecules as imaging agents: considerations and caveats," *Nanomedicine*, vol. 3, no. 5, pp. 703–717, 2008.

[52] C. V. Bowen, X. Zhang, G. Saab, P. J. Gareau, and B. K. Rutt, "Application of the static dephasing regime theory to superparamagnetic iron-oxide loaded cells," *Magnetic Resonance in Medicine*, vol. 48, no. 1, pp. 52–61, 2002.

[53] D. Yablonskiy and E. Haacke, "Theory of NMR singal behavior in magnetically inhomogeneous tissues - the static dephasing regime," *Magnetic Resonance In Medicine*, vol. 32, no. 6, pp. 749–763, 1994.

[54] G. Simon, J. Bauer, O. Saborovski, Y. Fu, C. Corot, M. Wendland, and H. Daldrup-Link, "T1 and T2 relaxivity of intracellular and extracellular USPIO at 1.5T and 3T clinical MR scanning," *European Radiology*, vol. 16, no. 3, pp. 738–745, 2006.

[55] M. J.-E. Lee, O. Veiseh, N. Bhattarai, C. Sun, S. J. Hansen, S. Ditzler, S. Knoblaugh, D. Lee, R. Ellenbogen, M. Zhang, and J. M. Olson, "Rapid Pharmacokinetic and Biodistribution Studies Using Cholorotoxin-Conjugated Iron Oxide Nanoparticles: A Novel Non-Radioactive Method (Rapid PK and Biodistribution)," *PLoS ONE*, vol. 5, no. 3, p. e9536, 2010.

[56] M. Jenkinson, C. F. Beckmann, T. E. J. Behrens, M. W. Woolrich, and S. M. Smith, "FSL," *NeuroImage*, vol. 62, no. 2, pp. 782–790, 2012.

[57] N. Lee and T. Hyeon, "Designed synthesis of uniformly sized iron oxide nanoparticles for efficient magnetic resonance imaging contrast agents," *Chemical Society Reviews*, vol. 41, no. 7, pp. 2575–2589, 2012.

[58] M. D. Hope, T. A. Hope, C. Zhu, F. Faraji, H. Haraldsson, K. Ordovas, and D. Saloner, "Vascular Imaging With Ferumoxytol as a Contrast Agent," *American Journal Of Roentgenology*, vol. 205, no. 3, pp. W366–W373, 2015.

[59] C. Corot, P. Robert, J.-M. Idée, and M. Port, "Recent advances in iron oxide nanocrystal technology for medical imaging," *Advanced Drug Delivery Reviews*, vol. 58, no. 14, pp. 1471–1504, 2006.

[60] K. Wang, F. M. Kievit, J. G. Sham, M. Jeon, Z. R. Stephen, A. Bakthavatsalam, J. O. Park, and M. Zhang, "Iron-Oxide-Based Nanovector for Tumor Targeted siRNA Delivery in an Orthotopic Hepatocellular Carcinoma Xenograft Mouse Model," *Small*, vol. 12, no. 4, pp. 477–487, 2016.

[61] F. M. Kievit and M. Zhang, "Cancer Nanotheranostics: Improving Imaging and Therapy by Targeted Delivery Across Biological Barriers," Weinheim, pp. H217–H247, 2011.

[62] C. Vaure and Y. Liu, "A comparative review of toll-like receptor 4 expression and functionality in different animal species," *Frontiers In Immunology*, vol. 5, p. 316, 2014.

[63] M. Levy, N. Luciani, D. Alloyeau, D. Elgrabli, V. Deveaux, C. Pechoux, S. Chat, G. Wang, N. Vats, F. Gendron, C. Factor, S. Lotersztajn, A. Luciani, C. Wilhelm, and F. Gazeau, "Long term in vivo biotransformation of iron oxide nanoparticles," *Biomaterials*, vol. 32, no. 16, pp. 3988–3999, 2011.

[64] M. Martignoni, G. M. M. Groothuis, and R. de Kanter, "Species differences between mouse, rat, dog, monkey and human CYP-mediated drug metabolism, inhibition and induction," *Expert Opinion on Drug Metabolism & Toxicology*, vol. 2, no. 6, pp. 875–894, 2006.

[65] H. S. Choi, W. Liu, P. Misra, E. Tanaka, J. P. Zimmer, B. I. Ipe, M. G. Bawendi, and J. V. Frangioni, "Renal clearance of quantum dots," *Nature Biotechnology*, vol. 25, no. 10, pp. 1165–1170, 2007.

[66] C. Fleck, "Determination of the glomerular filtration rate (GFR): methodological problems, age-dependence, consequences of various surgical interventions, and the influence of different drugs and toxic substances," *Physiological Research*, vol. 48, no. 4, pp. 267–279, 1999.

[67] C. Donadio, A. Lucchesi, G. Tramonti, and C. Bianchi, "Creatinine clearance predicted from body cell mass is a good indicator of renal function," *Kidney International*, pp. S166–S168, 1997.

[68] R. A. Martin, D. A. Brott, J. C. Zandee, and M. J. Mckeel, "Differential analysis of animal bone marrow by flow cytometry," *Cytometry*, vol. 13, no. 6, pp. 638–643, 1992.

[69] K. Sou, B. Goins, B. O. Oyajobi, B. L. Travi, and W. T. Phillips, "Bone marrow-targeted liposomal carriers," *Expert Opinion on Drug Delivery*, vol. 8, no. 3, pp. 317–328, 2011.

[70] R. A. Petros and J. M. DeSimone, "Strategies in the design of nanoparticles for therapeutic applications," *Nature Reviews Drug Discovery*, vol. 9, no. 8, pp. 615–627, 2010.

[71] A. Deo, F. Theil, and J. Nicolas, "Confounding Parameters in Preclinical Assessment of Blood-Brain Barrier Permeation: An Overview With Emphasis on Species Differences and Effect of Disease States," *Molecular Pharmaceutics*, vol. 10, no. 5, pp. 1581–1595, 2013.

[72] K. Ito, Y. Uchida, S. Ohtsuki, S. Aizawa, H. Kawakami, Y. Katsukura, J. Kamiie, and T. Terasaki, "Quantitative Membrane Protein Expression at the Blood-Brain Barrier of Adult and Younger Cynomolgus Monkeys," *Journal of Pharmaceutical Sciences*, vol. 100, no. 9, pp. 3939–3950, 2011.

[73] Y. Lu, H. A. Barton, L. Leung, L. Zhang, E. Hajos-Korcsok, C. E. Nolan, J. Liu, S. L. Becker, K. M. Wood, A. E. Robshaw, C. K. Taylor, B. T. O'Neill, M. A. Brodney, and D. Riddell, "Cerebrospinal Fluid Beta-Amyloid Turnover in the Mouse, Dog, Monkey and Human Evaluated by Systematic Quantitative Analyses," *Neurodegenerative Diseases*, vol. 12, no. 1, pp. 36–50, 2013.

[74] R. Lonser, M. Sarntinoranont, P. Morrison, and E. Oldfield, "Convection-enhanced delivery to the central nervous system," *Journal Of Neurosurgery*, vol. 122, no. 3, pp. 697–706, 2015.

[75] O. Van Tellingen, B. Yetkin-Arik, M. C. De Gooijer, P. Wesseling, T. Wurdinger, and H. E. De Vries, "Overcoming the blood-brain tumor barrier for effective glioblastoma treatment," *Drug Resistance Updates*, vol. 19, pp. 1–12, 2015.

[76] R. Bobo, D. Laske, A. Akbasak, and P. Morrison, "Convection-enhanced delivery of macromolecules in the brain," *Proceedings of the National Academy of Sciences of the United States of America*, vol. 91, no. 6, pp. 2076–2080, 1994.

[77] E. Allard, C. Passirani, and J.-P. Benoit, "Convection-enhanced delivery of nanocarriers for the treatment of brain tumors," *Biomaterials*, vol. 30, no. 12, pp. 2302–2318, 2009.

[78] M. A. Vogelbaum and M. K. Aghi, "Convection-enhanced delivery for the treatment of glioblastoma," *Neuro-Oncology*, vol. 17, no. suppl2, pp. ii3–ii8, 2015.

[79] P. A. Chiarelli, F. M. Kievit, M. Zhang, and R. G. Ellenbogen, "Bionanotechnology and the future of glioma," *Surgical neurology international*, vol. 6, no. Suppl 1, pp. S45–S58, 2015.

[80] S. Platt, E. Nduom, M. Kent, C. Freeman, R. Machaidze, M. Kaluzova, L. Wang, H. Mao, and C. G. Hadjipanayis, "Canine model of convection-enhanced delivery of cetuximab-conjugated iron-oxide nanoparticles monitored with magnetic resonance imaging," *Clinical Neurosurgery*, vol. 59, no. CN_Suppl_1, pp. 107–113, 2012.

[81] C. G. Hadjipanayis, R. Machaidze, M. Kaluzova, L. Wang, A. J. Schuette, H. Chen, X. Wu, and H. Mao, "EGFRvIII antibody-conjugated iron oxide nanoparticles for magnetic resonance imaging-guided convection-enhanced delivery and targeted therapy of glioblastoma," *Cancer Research*, vol. 70, no. 15, pp. 6303–6312, 2010.

[82] C. S. Schneider, J. G. Perez, E. Cheng, C. Zhang, P. Mastorakos, J. Hanes, J. A. Winkles, G. F. Woodworth, and A. J. Kim, "Minimizing the non-specific binding of nanoparticles to the brain enables active targeting of Fn14-positive glioblastoma cells," *Biomaterials*, vol. 42, pp. 42–51, 2015.

[83] Z. R. Stephen, F. M. Kievit, O. Veiseh, P. A. Chiarelli, C. Fang, K. Wang, S. J. Hatzinger, R. G. Ellenbogen, J. R. Silber, and M. Zhang, "Redox-responsive magnetic nanoparticle for targeted convection-enhanced delivery of O6-benzylguanine to brain tumors," *ACS Nano*, vol. 8, no. 10, pp. 10 383–10 395, 2014.

[84] O. Veiseh, C. Sun, C. Fang, N. Bhattarai, J. Gunn, F. Kievit, K. Du, B. Pullar, D. Lee, R. G. Ellenbogen, J. Olson, and M. Zhang, "Specific targeting of brain tumors with an optical/magnetic resonance imaging nanoprobe across the blood-brain barrier," *Cancer Research*, vol. 69, no. 15, pp. 6200–6207, 2009.

[85] B. L. Carlson, J. L. Pokorny, M. A. Schroeder, and J. N. Sarkaria, "Establishment, maintenance and in vitro and in vivo applications of primary human glioblastoma multiforme (GBM) xenograft models for translational biology studies and drug discovery." *Current Protocols in Pharmacology*, vol. 52, no. 14, pp. 1–14, 2011.

[86] K.-C. Wei, C.-Y. Huang, P.-Y. Chen, L.-Y. Feng, T.-W. E. Wu, S.-M. Chen, H.-C. Tsai, Y.-J. Lu, N.-M. Tsang, C.-K. Tseng, P.-C. Pai, and J.-W. Shin, "Evaluation of the prognostic value of CD44 in glioblastoma multiforme," *Anticancer Research*, vol. 30, no. 1, pp. 253–259, 2010.

[87] P. M. Costa, A. L. Cardoso, L. S. Mendonça, A. Serani, C. Custódia, M. Conceição, S. Simões, J. N. Moreira, L. Pereira de Almeida, and M. C. Pedroso de Lima, "Tumor-targeted Chlorotoxin-coupled Nanoparticles for Nucleic Acid Delivery to Glioblastoma Cells: A Promising System for Glioblastoma Treatment," *Molecular Therapy-Nucleic Acids*, vol. 2, no. 6, p. e100, 2013.

[88] R. K. Oberoi, K. E. Parrish, T. T. Sio, R. K. Mittapalli, W. F. Elmquist, and J. N. Sarkaria, "Strategies to improve delivery of anticancer drugs across the blood-brain barrier to treat glioblastoma," *Neuro-Oncology*, vol. 18, no. 1, pp. 27–36, 2016.

[89] P. A. Hardy, D. Keeley, G. Schorn, E. Forman, Y. Ai, R. Venugopalan, Z. Zhang, and L. H. Bradley, "Convection enhanced delivery of different molecular weight tracers of gadolinium-tagged polylysine," *Journal of Neuroscience Methods*, vol. 219, no. 1, pp. 169–175, 2013.

[90] A. Jahangiri, A. T. Chin, P. M. Flanigan, R. Chen, K. Bankiewicz, and M. K. Aghi, "Convection-enhanced delivery in glioblastoma: a review of preclinical and clinical studies," *Journal of Neurosurgery*, vol. 126, no. 1, pp. 191–200, 2017.

[91] Z. R. Stephen, R. N. Gebhart, M. Jeon, A. A. Blair, R. G. Ellenbogen, J. R. Silber, and M. Zhang, "pH-Sensitive O6-Benzylguanosine Polymer Modified Magnetic Nanoparticles for Treatment of Glioblastomas," *Bioconjugate Chemistry*, vol. 28, no. 1, pp. 194–202, 2017.

[92] F. M. Kievit, O. Veiseh, C. Fang, N. Bhattarai, D. Lee, R. G. Ellenbogen, and M. Zhang, "Chlorotoxin labeled magnetic nanovectors for targeted gene delivery to glioma," *ACS Nano*, vol. 4, no. 8, pp. 4587–4594, 2010.

[93] A. Anselmo and S. Mitragotri, "A Review of Clinical Translation of Inorganic Nanoparticles," *The AAPS Journal*, vol. 17, no. 5, pp. 1041–1054, 2015.

[94] B. Perlstein, Z. Ram, D. Daniels, A. Ocherashvilli, Y. Roth, S. Margel, and Y. Mardor, "Convection-enhanced delivery of maghemite nanoparticles: Increased efficacy and MRI monitoring," *Neuro-oncology*, vol. 10, no. 2, pp. 153–161, 2008.

[95] Y. Mardor, O. Rahav, Y. Zauberman, Z. Lidar, A. Ocherashvilli, D. Daniels, Y. Roth, S. E. Maier, A. Orenstein, and Z. Ram, "Convection-enhanced drug delivery: increased efficacy and magnetic resonance image monitoring," *Cancer Research*, vol. 65, no. 15, pp. 6858–6863, 2005.

[96] S. Idema, V. Caretti, M. L. M. Lamfers, V. W. van Beusechem, D. P. Noske, W. P. Vandertop, and C. M. F. Dirven, "Anatomical Differences Determine Distribution of Adenovirus after Convection-Enhanced Delivery to the Rat Brain (CED of Adenovirus into Rat Brain)," *PLoS ONE*, vol. 6, no. 10, p. e24396, 2011.

[97] G. M. Bernal, M. J. Lariviere, N. Mansour, P. Pytel, K. E. Cahill, D. J. Voce, S. Kang, R. Spretz, U. Welp, S. E. Noriega, L. Nuñez, G. Larsen, R. R. Weichselbaum, and B. Yamini, "Convection-enhanced delivery and in vivo imaging of polymeric nanoparticles for the treatment of malignant glioma," *Nanomedicine: Nanotechnology, Biology, and Medicine*, vol. 10, no. 1, pp. 149–157, 2014.

[98] E. Corem-Salkmon, Z. Ram, D. Daniels, B. Perlstein, D. Last, S. Salomon, G. Tamar, R. Shneor, D. Guez, S. Margel, and Y. Mardor, "Convection-enhanced delivery of methotrexate-loaded maghemite nanoparticles," *International Journal of Nanomedicine*, vol. 6, pp. 1595–1602, 2011.

[99] N. J. Szerlip, S. Walbridge, L. Yang, P. F. Morrison, J. W. Degen, S. T. Jarrell, J. Kouri, P. B. Kerr, R. Kotin, E. H. Oldfield, and R. R. Lonser, "Real-time imaging of convection-enhanced delivery of viruses and virus-sized particles," *Journal of Neurosurgery*, vol. 107, no. 3, pp. 560–567, 2007.

[100] R. R. Lonser, S. Walbridge, K. Garmestani, J. A. Butman, H. A. Walters, A. O. Vortmeyer, P. F. Morrison, M. W. Brechbiel, and E. H. Oldfield, "Successful and safe perfusion of the primate brainstem: in vivo magnetic resonance imaging of macromolecular distribution during infusion," *Journal of Neurosurgery*, vol. 97, no. 4, pp. 905–913, 2002.

[101] G. J. A. Murad, S. Walbridge, P. F. Morrison, N. Szerlip, J. A. Butman, E. H. Oldfield, and R. R. Lonser, "Image-guided convection-enhanced delivery of gemcitabine to the brainstem," *Journal of Neurosurgery*, vol. 106, no. 2, pp. 351–356, 2007.

[102] D. I. Sandberg, M. A. Edgar, and M. M. Souweidane, "Convection-enhanced delivery into the rat brainstem," *Journal of Neurosurgery*, vol. 96, no. 5, pp. 885–891, 2002.

[103] J. Deshane, C. C. Garner, and H. Sontheimer, "Chlorotoxin inhibits glioma cell invasion via matrix metalloproteinase-2," *The Journal of Biological Chemistry*, vol. 278, no. 6, pp. 4135–4144, 2003.

[104] K. Kesavan, J. Ratliff, E. Johnson, W. Dahlberg, J. Asara, P. Misra, J. Frangioni, and D. Jacoby, "Annexin A2 Is a Molecular Target for TM601, a Peptide with Tumor-targeting and Anti-angiogenic Effects," *Journal Of Biological Chemistry*, vol. 285, no. 7, pp. 4366–4374, 2010.

[105] A. Louveau, I. Smirnov, T. J. Keyes, J. D. Eccles, S. J. Rouhani, J. D. Peske, N. C. Derecki, D. Castle, J. W. Mandell, S. L. Kevin, T. H. Harris, and J. Kipnis, "Structural and functional features of central nervous system lymphatics," *Nature*, vol. 523, no. 7560, pp. 337–341, 2015.

[106] A. Aspelund, S. Antila, S. T. Proulx, T. V. Karlsen, S. Karaman, M. Detmar, H. Wiig, and K. Alitalo, "A dural lymphatic vascular system that drains brain interstitial fluid and macromolecules," *The Journal of Experimental Medicine*, vol. 212, no. 7, pp. 991–999, 2015.

[107] D. Paniagua, I. Vergara, L. Boyer, and A. Alagón, "Role of Lymphatic System on Snake Venom Absorption," in *Snake Venoms*, P. Gopalakrishnakone, H. Inagaki, C.-W. Vogel, A. K. Mukherjee, and T. R. Rahmy, Eds. Dordrecht: Springer Netherlands, 2017, pp. 453–474.

[108] D. Paniagua, L. Jiménez, C. Romero, I. Vergara, A. Calderón, M. Benard, M. J. Bernas, H. Rilo, A. de Roodt, G. D' Suze, M. H. Witte, L. Boyer, and A. Alagón, "Lymphatic route of transport and pharmacokinetics of Micrurus fulvius (coral snake) venom in sheep," *Lymphology*, vol. 45, no. 4, pp. 144–153, 2012.

[109] S. Mao, W. Sun, and T. Kissel, "Chitosan-based formulations for delivery of DNA and siRNA," *Advanced Drug Delivery Reviews*, vol. 62, no. 1, pp. 12–27, 2010.

[110] S. Tammam, H. Azzazy, H. Breitinger, and A. Lamprecht, "Chitosan Nanoparticles for Nuclear Targeting: The Effect of Nanoparticle Size and Nuclear Localization Sequence Density," *Molecular Pharmaceutics*, vol. 12, no. 12, pp. 4277–4289, 2015.

[111] M. Orth, K. Lauber, M. Niyazi, A. A. Friedl, M. Li, C. Maihöfer, L. Schüttrumpf, A. Ernst, O. M. Niemöller, and C. Belka, "Current concepts in clinical radiation oncology," *Radiation and Environmental Biophysics*, vol. 53, no. 1, pp. 1–29, 2014.

[112] A. Prasanna, M. M. Ahmed, M. Mohiuddin, and C. N. Coleman, "Exploiting sensitization windows of opportunity in hyper and hypo-fractionated radiation therapy," *Journal of Thoracic Disease*, vol. 6, no. 4, pp. 287–302, 2014.

[113] R. R. Weichselbaum, H. Liang, L. Deng, and Y.-X. Fu, "Radiotherapy and immunotherapy: a beneficial liaison?" *Nature Reviews Clinical Oncology*, vol. 14, no. 6, pp. 365–379, 2017.

[114] F. B. Furnari, T. Fenton, R. M. Bachoo, A. Mukasa, J. M. Stommel, A. Stegh, W. C. Hahn, K. L. Ligon, D. N. Louis, C. Brennan, L. Chin, R. A. DePinho, and W. K. Cavenee, "Malignant astrocytic glioma: Genetics, biology, and paths to treatment," *Genes and Development*, vol. 21, pp. 2683–2710, 2007.

[115] V. Gouazé-Andersson, C. Delmas, M. Taurand, J. Martinez-Gala, S. Evrard, S. Mazoyer, C. Toulas, and E. Cohen-Jonathan-Moyal, "FGFR1 Induces Glioblastoma Radioresistance through the PLCγ/Hif1α Pathway," *Cancer Research*, vol. 76, no. 10, pp. 3036–3044, 2016.

[116] H. Matsudaira, A. M. Ueno, and I. Furuno, "Iodine contrast medium sensitizes cultured mammalian cells to X rays but not to γ rays," *Radiation Research*, vol. 84, no. 1, pp. 144–148, 1980.

[117] K. T. Butterworth, S. J. McMahon, F. J. Currell, and K. M. Prise, "Physical basis and biological mechanisms of gold nanoparticle radiosensitization," *Nanoscale*, vol. 4, no. 16, pp. 4830–4838, 2012.

[118] J. A. Coulter, W. B. Hyland, J. Nicol, and F. J. Currell, "Radiosensitising Nanoparticles as Novel Cancer Therapeutics — Pipe Dream or Realistic Prospect?" *Clinical Oncology*, vol. 25, no. 10, pp. 593–603, 2013.

[119] P. Liu, Z. Huang, Z. Chen, R. Xu, H. Wu, F. Zang, C. Wang, and N. Gu, "Silver nanoparticles: a novel radiation sensitizer for glioma?" *Nanoscale*, vol. 5, no. 23, pp. 11 829–11 836, 2013.

[120] E. Locatelli, M. Naddaka, C. Uboldi, G. Loudos, E. Fragogeorgi, V. Molinari, A. Pucci, T. Tsotakos, D. Psimadas, J. Ponti, and M. C. Franchini, "Targeted delivery of silver nanoparticles and alisertib: in vitro and in vivo synergistic effect against glioblastoma," *Nanomedicine*, vol. 9, no. 6, pp. 839–849, 2014, pMID: 24433240.

[121] A. Detappe, S. Kunjachan, L. Sancey, M. Makrigiorgos, R. Langer, O. Tillement, and R. I. Berbeco, "Gadolinium Nanoparticles for Magnetic Resonance Guided Radiation Therapy," *International Journal of Radiation Oncology * Biology * Physics*, vol. 96, no. 2, pp. S110–S111, 2016.

[122] S. Kotb, A. Detappe, F. Lux, F. Appaix, E. L. Barbier, V.-L. Tran, M. Plissonneau, H. Gehan, F. Lefranc, C. Rodriguez-Lafrasse, C. Verry, R. Berbeco, O. Tillement, and L. Sancey, "Gadolinium-Based Nanoparticles and Radiation Therapy for Multiple Brain Melanoma Metastases: Proof of Concept before Phase I Trial," *Theranostics*, vol. 6, no. 3, pp. 418–427, 2016.

[123] J. Liu, Y. Yang, W. Zhu, X. Yi, Z. Dong, X. Xu, M. Chen, K. Yang, G. Lu, L. Jiang, and Z. Liu, "Nanoscale metal-organic frameworks for combined photodynamic & radiation therapy in cancer treatment," *Biomaterials*, vol. 97, pp. 1–9, 2016.

[124] E. Brun and C. Sicard-Roselli, "Actual questions raised by nanoparticle radiosensitization," *Radiation Physics and Chemistry*, vol. 128, pp. 134–142, 2016.

[125] S. Klein, A. Sommer, L. V. R. Distel, W. Neuhuber, and C. Kryschi, "Superparamagnetic iron oxide nanoparticles as radiosensitizer via enhanced reactive oxygen species formation," *Biochemical and Biophysical Research Communications*, vol. 425, no. 2, pp. 393–397, 2012.

[126] J. K. Kim, S. J. Seo, K. H. Kim, T. J. Kim, M. H. Chung, K. R. Kim, and T. K. Yang, "Therapeutic application of metallic nanoparticles combined with particle-induced x-ray emission effect," *Nanotechnology*, vol. 21, no. 42, p. 425102, 2010.

[127] A. C. Anselmo and S. Mitragotri, "Nanoparticles in the clinic," *Bioengineering & Translational Medicine*, vol. 1, no. 1, pp. 10–29, 2016.

[128] C. Sicard-Roselli, E. Brun, M. Gilles, G. Baldacchino, C. Kelsey, H. McQuaid, C. Polin, N. Wardlow, and F. Currell, "A New Mechanism for Hydroxyl Radical Production in Irradiated Nanoparticle Solutions," *Small*, vol. 10, no. 16, pp. 3338–3346, 2014.

[129] D. K. Nagesha, B. D. Plouffe, M. Phan, L. H. Lewis, S. Sridhar, and S. K. Murthy, "Functionalization-induced improvement in magnetic properties of Fe3O4 nanoparticles for biomedical applications," *Journal of Applied Physics*, vol. 105, no. 7, p. 07B317, 2009.

[130] A. Saraswathy, S. S. Nazeer, M. Jeevan, N. Nimi, S. Arumugam, V. S. Harikrishnan, P. R. H. Varma, and R. S. Jayasree, "Citrate coated iron oxide nanoparticles with enhanced relaxivity for in vivo magnetic resonance imaging of liver fibrosis," *Colloids and Surfaces B: Biointerfaces*, vol. 117, pp. 216–224, 2014.

[131] Z. R. Stephen, C. J. Dayringer, J. J. Lim, R. A. Revia, M. V. Halbert, M. Jeon, A. Bakthavatsalam, R. G. Ellenbogen, and M. Zhang, "Approach to Rapid Synthesis and Functionalization of Iron Oxide Nanoparticles for High Gene Transfection," *ACS Applied Materials & Interfaces*, vol. 8, no. 10, pp. 6320–6328, 2016.

[132] O. Kizu, K. Yamada, and T. Nishimura, "Proton Chemical Shift Imaging in Normal Pressure Hydrocephalus," *American Journal of Neuroradiology*, vol. 22, no. 9, pp. 1659–1664, 2001.

[133] D. P. Soares and M. Law, "Magnetic resonance spectroscopy of the brain: review of metabolites and clinical applications," *Clinical Radiology*, vol. 64, no. 1, pp. 12–21, 2009.

[134] A. Horská and P. B. Barker, "Imaging of brain tumors: MR spectroscopy and metabolic imaging," *Neuroimaging Clinics of North America*, vol. 20, no. 3, pp. 293–310, 2010.

[135] E. R. Danielsen and B. Ross, *Magnetic Resonance Spectroscopy Diagnosis of Neurological Diseases*, 1st ed. Boca Raton: CRC Press, 1999.

[136] F. M. Kievit, O. Veiseh, N. Bhattarai, C. Fang, J. W. Gunn, D. Lee, R. G. Ellenbogen, J. M. Olson, and M. Zhang, "PEI-PEG-Chitosan Copolymer Coated Iron Oxide Nanoparticles for Safe Gene Delivery: synthesis, complexation, and transfection," *Advanced Functional Materialstional materials*, vol. 19, no. 14, pp. 2244–2251, 2009.

[137] A. Rosset, L. Spadola, and O. Ratib, "OsiriX: An open-source software for navigating in multidimensional DICOM images," *Journal of Digital Imaging*, vol. 17, no. 3, pp. 205–216, 2004.

[138] M. Veiseh, P. Gabikian, S.-B. Bahrami, O. Veiseh, M. Zhang, R. C. Hackman, A. C. Ravanpay, M. R. Stroud, Y. Kusuma, S. J. Hansen, D. Kwok, N. M. Munoz, R. W. Sze, W. M. Grady, N. M. Greenberg, R. G. Ellenbogen, and J. M. Olson, "Tumor Paint: A Chlorotoxin:Cy5.5 Bioconjugate for Intraoperative Visualization of Cancer Foci," *Cancer Research*, vol. 67, no. 14, pp. 6882–6888, 2007.

[139] L. Soroceanu, Y. Gillespie, M. B. Khazaeli, and H. Sontheimer, "Use of Chlorotoxin for Targeting of Primary Brain Tumors," *Cancer Research*, vol. 58, no. 21, pp. 4871–4879, 1998.

[140] S. A. Lyons, J. O'Neal, and H. Sontheimer, "Chlorotoxin, a scorpion-derived peptide, specifically binds to gliomas and tumors of neuroectodermal origin," *Glia*, vol. 39, no. 2, pp. 162–173, 2002.

[141] L. Fass, "Imaging and cancer: A review," *Molecular Oncology*, vol. 2, no. 2, pp. 115–152, 2008.

[142] J. P. O'Connor, E. O. Aboagye, J. E. Adams, H. J. Aerts, S. F. Barrington, A. J. Beer, R. Boellaard, S. E. Bohndiek, M. Brady, G. Brown, D. L. Buckley, T. L. Chenevert, L. P. Clarke, S. Collette, G. J. Cook, N. M. Desouza, J. C. Dickson, C. Dive, J. L. Evelhoch, C. Faivre-Finn, F. A. Gallagher, F. J. Gilbert, R. J. Gillies, V. Goh, J. R. Griffiths, A. M. Groves, S. Halligan, A. L. Harris, D. J. Hawkes, O. S. Hoekstra, E. P. Huang, B. F. Hutton, E. F. Jackson, G. C. Jayson, A. Jones, D. M. Koh, D. Lacombe, P. Lambin, N. Lassau, M. O. Leach, T. Y. Lee, E. L. Leen, J. S. Lewis, Y. Liu, M. F. Lythgoe, P. Manoharan, R. J. Maxwell, K. A. Miles, B. Morgan, S. Morris, T. Ng, A. R. Padhani, G. J. Parker, M. Partridge, A. P. Pathak, A. C. Peet, S. Punwani, A. R. Reynolds, S. P. Robinson, L. K. Shankar, R. A. Sharma, D. Soloviev, S. Stroobants, D. C. Sullivan, S. A. Taylor, P. S. Tofts, G. M. Tozer, M. Van Herk, S. Walker-Samuel, J. Wason, K. J. Williams, P. Workman, T. E. Yankeelov, K. M. Brindle, L. M. McShane, A. Jackson, and J. C. Waterton, "Imaging biomarker roadmap for cancer studies," *Nature Reviews Clinical Oncology*, vol. 14, no. 3, pp. 169–186, 2017.

[143] C. Enzinger, F. Barkhof, O. Ciccarelli, M. Filippi, L. Kappos, M. A. Rocca, S. Ropele, À. Rovira, T. Schneider, N. de Stefano, H. Vrenken, C. Wheeler-Kingshott, J. Wuerfel, and F. Fazekas, "Nonconventional MRI and microstructural cerebral changes in multiple sclerosis," *Nature Reviews Neurology*, vol. 11, no. 12, pp. 676–686, 2015.

[144] J. Koikkalainen, H. Rhodius-Meester, A. Tolonen, F. Barkhof, B. Tijms, A. W. Lemstra, T. Tong, R. Guerrero, A. Schuh, C. Ledig, D. Rueckert, H. Soininen, A. M. Remes, G. Waldemar, S. Hasselbalch, P. Mecocci, W. Van Der Flier, and J. Lötjönen, "Differential diagnosis of neurodegenerative diseases using structural MRI data," *NeuroImage: Clinical*, vol. 11, pp. 435–449, 2016.

[145] Y. D. Xiao, R. Paudel, J. Liu, C. Ma, Z. S. Zhang, and S. K. Zhou, "MRI contrast agents: Classification and application (Review)," *International Journal of Molecular Medicine*, vol. 38, no. 5, pp. 1319–1326, 2016.

[146] Z. Gao, T. Ma, E. Zhao, D. Docter, W. Yang, R. H. Stauber, and M. Gao, "Small is Smarter: Nano MRI Contrast Agents - Advantages and Recent Achievements," *Small*, vol. 12, no. 5, pp. 556–576, 2016.

[147] P. Stratta, C. Canavese, and S. Aime, "Gadolinium-Enhanced Magnetic Resonance Imaging, Renal Failure and Nephrogenic Systemic Fibrosis /Nephrogenic Fibrosing Dermopathy," *Current Medicinal Chemistry*, vol. 15, no. 12, pp. 1229–1235, 2008.

[148] H. S. Thomsen, S. K. Morcos, and P. Dawson, "Is there a causal relation between the administration of gadolinium based contrast media and the development of nephrogenic systemic fibrosis (NSF)?" *Clinical Radiology*, vol. 61, no. 11, pp. 905–906, 2006.

[149] M. Le Fur and P. Caravan, "The biological fate of gadolinium-based MRI contrast agents: a call to action for bioinorganic chemists," *Metallomics*, vol. 11, no. 2, pp. 240–254, 2019.

[150] E. Vergauwen, A.-M. Vanbinst, C. Brussaard, P. Janssens, D. De Clerck, M. Van Lint, A. C. Houtman, O. Michel, K. Keymolen, B. Lefevere, S. Bohler, D. Michielsen, A. C. Jansen, V. Van Velthoven, and S. Gläsker, "Central nervous system gadolinium accumulation in patients undergoing periodical contrast MRI screening for hereditary tumor syndromes," *Hereditary Cancer in Clinical Practice*, vol. 16, no. 1, p. 2, 2018.

[151] T. H. Shin, Y. Choi, S. Kim, and J. Cheon, "Recent advances in magnetic nanoparticle-based multi-modal imaging," *Chemical Society Reviews*, vol. 44, no. 14, pp. 4501–4516, 2015.

[152] R. Romero-Aburto, T. N. Narayanan, Y. Nagaoka, T. Hasumura, T. M. Mitcham, T. Fukuda, P. J. Cox, R. R. Bouchard, T. Maekawa, D. S. Kumar, S. V. Torti, S. A. Mani, and P. M. Ajayan, "Fluorinated graphene oxide; A new multimodal material for biological applications," *Advanced Materials*, vol. 25, no. 39, pp. 5632–5637, 2013.

[153] S. H. Lee, B. H. Kim, H. B. Na, and T. Hyeon, "Paramagnetic inorganic nanoparticles as T1 MRI contrast agents," *Wiley Interdisciplinary Reviews: Nanomedicine and Nanobiotechnology*, vol. 6, no. 2, pp. 196–209, 2014.

[154] W. S. Seo, J. H. Lee, X. Sun, Y. Suzuki, D. Mann, Z. Liu, M. Terashima, P. C. Yang, M. V. McConnell, D. G. Nishimura, and H. Dai, "FeCo/graphitic-shell nanocrystals as advanced magnetic-resonance-imaging and near-infrared agents," *Nature Materials*, vol. 5, no. 12, pp. 971–976, 2006.

[155] B. H. Kim, N. Lee, H. Kim, K. An, Y. I. Park, Y. Choi, K. Shin, Y. Lee, S. G. Kwon, H. B. Na, J. G. Park, T. Y. Ahn, Y. W. Kim, W. K. Moon, S. H. Choi, and T. Hyeon, "Large-scale synthesis of uniform and extremely small-sized iron oxide nanoparticles for high-resolution T 1 magnetic resonance imaging contrast agents," *Journal of the American Chemical Society*, vol. 133, no. 32, pp. 12 624–12 631, 2011.

[156] Z. Zhen and J. Xie, "Development of manganese-based nanoparticles as contrast probes for magnetic resonance imaging," *Theranostics*, vol. 2, no. 1, pp. 45–54, 2012.

[157] Z. Shen, A. Wu, and X. Chen, "Iron Oxide Nanoparticle Based Contrast Agents for Magnetic Resonance Imaging," *Molecular Pharmaceutics*, vol. 14, no. 5, pp. 1352–1364, 2017.

[158] Z. Zhou, D. Huang, J. Bao, Q. Chen, G. Liu, Z. Chen, X. Chen, and J. Gao, "A synergistically enhanced T1-T2 dual-modal contrast agent," *Advanced Materials*, vol. 24, no. 46, pp. 6223–6228, 2012.

[159] H. B. Na, J. H. Lee, K. An, Y. I. Park, M. Park, I. S. Lee, D.-H. Nam, S. T. Kim, S.-H. Kim, S.-W. Kim, K.-H. Lim, K.-S. Kim, S.-O. Kim, and T. Hyeon, "Development of aT1 Contrast Agent for Magnetic Resonance Imaging Using MnO Nanoparticles," *Angewandte Chemie*, vol. 119, no. 28, pp. 5493–5497, 2007.

[160] F. Chen, W. Bu, S. Zhang, J. Liu, W. Fan, L. Zhou, W. Peng, and J. Shi, "Gd3+-ion-doped upconversion nanoprobes: Relaxivity mechanism probing and sensitivity optimization," *Advanced Functional Materials*, vol. 23, no. 3, pp. 298–307, 2013.

[161] H. Chen, G. D. Wang, W. Tang, T. Todd, Z. Zhen, C. Tsang, K. Hekmatyar, T. Cowger, R. B. Hubbard, W. Zhang, J. Stickney, B. Shen, and J. Xie, "Gd-encapsulated carbonaceous dots with efficient renal clearance for magnetic resonance imaging," *Advanced Materials*, vol. 26, no. 39, pp. 6761–6766, 2014.

[162] C. Saraiva, C. Praça, R. Ferreira, T. Santos, L. Ferreira, and L. Bernardino, "Nanoparticle-mediated brain drug delivery: Overcoming blood-brain barrier to treat neurodegenerative diseases," *Journal of Controlled Release*, vol. 235, pp. 34–47, 2016.

[163] Y. Chong, Y. Ma, H. Shen, X. Tu, X. Zhou, J. Xu, J. Dai, S. Fan, and Z. Zhang, "The in vitro and in vivo toxicity of graphene quantum dots," *Biomaterials*, vol. 35, no. 19, pp. 5041–5048, 2014.

[164] S. Radhakrishnan, A. Samanta, P. M. Sudeep, K. L. Maldonado, S. A. Mani, G. Acharya, C. S. Tiwary, A. K. Singh, and P. M. Ajayan, "Metal-Free Dual Modal Contrast Agents Based on Fluorographene Quantum Dots," *Particle and Particle Systems Characterization*, vol. 34, no. 1, p. 1600221, 2017.

[165] H. Wang, R. Revia, K. Wang, R. J. Kant, Q. Mu, Z. Gai, K. Hong, and M. Zhang, "Paramagnetic Properties of Metal-Free Boron-Doped Graphene Quantum Dots and Their Application for Safe Magnetic Resonance Imaging," *Advanced Materials*, vol. 29, no. 11, p. 1605416, 2017.

[166] K. E. Kellar, D. K. Fujii, W. H. Gunther, K. Briley-Sæbø, A. Bjørnerud, M. Spiller, and S. H. Koenig, "NC 100150 injection, a preparation of optimized iron oxide nanoparticles for positive-contrast MR angiography," *Journal of Magnetic Resonance Imaging*, vol. 11, no. 5, pp. 488–494, 2000.

[167] J. Gao, H. Gu, and B. Xu, "Multifunctional magnetic nanoparticles: design, synthesis, and biomedical applications," *Accounts of Chemical Research*, vol. 42, no. 8, pp. 1097–1107, 2009.

[168] P. Shen and Y. Xia, "Synthesis-modification integration: One-step fabrication of boronic acid functionalized carbon dots for fluorescent blood sugar sensing," *Analytical Chemistry*, vol. 86, no. 11, pp. 5323–5329, 2014.

[169] M. Matsumoto, Y. Saito, C. Park, T. Fukushima, and T. Aida, "Ultrahigh-throughput exfoliation of graphite into pristine 'single-layer' graphene using microwaves and molecularly engineered ionic liquids," *Nature Chemistry*, vol. 7, no. 9, pp. 730–736, 2015.

[170] X. Wu, F. Tian, W. Wang, J. Chen, M. Wu, and J. X. Zhao, "Fabrication of highly fluorescent graphene quantum dots using L-glutamic acid for in vitro/in vivo imaging and sensing," *Journal of Materials Chemistry C*, vol. 1, no. 31, pp. 4676–4684, 2013.

[171] Y. Hernandez, V. Nicolosi, M. Lotya, F. M. Blighe, Z. Sun, S. De, I. T. McGovern, B. Holland, M. Byrne, Y. K. Gun'ko, J. J. Boland, P. Niraj, G. Duesberg, S. Krishnamurthy, R. Goodhue, J. Hutchison, V. Scardaci, A. C. Ferrari, and J. N. Coleman, "High-yield production of graphene by liquid-phase exfoliation of graphite," *Nature Nanotechnology*, vol. 3, no. 9, pp. 563–568, 2008.

[172] A. Eckmann, A. Felten, A. Mishchenko, L. Britnell, R. Krupke, K. S. Novoselov, and C. Casiraghi, "Probing the nature of defects in graphene by Raman spectroscopy," *Nano Letters*, vol. 12, no. 8, pp. 3925–3930, 2012.

[173] H. Wang, J. Zhuang, D. Velado, Z. Wei, H. Matsui, and S. Zhou, "Near-Infrared- and Visible-Light-Enhanced Metal-Free Catalytic Degradation of Organic Pollutants over Carbon-Dot-Based Carbocatalysts Synthesized from Biomass," *ACS Applied Materials and Interfaces*, vol. 7, no. 50, pp. 27 703–27 712, 2015.

[174] D. Hulicova-Jurcakova, M. Seredych, G. Q. Lu, and T. J. Bandosz, "Combined effect of nitrogen- and oxygen-containing functional groups of microporous activated carbon on its electrochemical performance in supercapacitors," *Advanced Functional Materials*, vol. 19, no. 3, pp. 438–447, 2009.

[175] H. Wang, Y. Zhou, D. Wu, L. Liao, S. Zhao, H. Peng, and Z. Liu, "Synthesis of boron-doped graphene monolayers using the sole solid feedstock by chemical vapor deposition," *Small*, vol. 9, no. 8, pp. 1316–1320, 2013.

[176] S. Dey, A. Govindaraj, K. Biswas, and C. N. Rao, "Luminescence properties of boron and nitrogen doped graphene quantum dots prepared from arc-discharge-generated doped graphene samples," *Chemical Physics Letters*, vol. 595-596, pp. 203–208, 2014.

[177] Z. Zuo, Z. Jiang, and A. Manthiram, "Porous B-doped graphene inspired by Fried-Ice for supercapacitors and metal-free catalysts," *Journal of Materials Chemistry A*, vol. 1, no. 43, pp. 13 476–13 483, 2013.

[178] H. Wang, Y. Sun, J. Yi, J. Fu, J. Di, A. del Carmen Alonso, and S. Zhou, "Fluorescent porous carbon nanocapsules for two-photon imaging, NIR/pH dual-responsive drug carrier, and photothermal therapy," *Biomaterials*, vol. 53, pp. 117–126, 2015.

[179] G. Eda, Y. Y. Lin, C. Mattevi, H. Yamaguchi, H. A. Chen, I. S. Chen, C. W. Chen, and M. Chhowalla, "Blue photoluminescence from chemically derived graphene oxide," *Advanced Materials*, vol. 22, no. 4, pp. 505–509, 2010.

[180] X. Li, M. Rui, J. Song, Z. Shen, and H. Zeng, "Carbon and Graphene Quantum Dots for Optoelectronic and Energy Devices: A Review," *Advanced Functional Materials*, vol. 25, no. 31, pp. 4929–4947, 2015.

[181] H. Wang, K. Wang, Q. Mu, Z. R. Stephen, Y. Yu, S. Zhou, and M. Zhang, "Mesoporous carbon nanoshells for high hydrophobic drug loading, multimodal optical imaging, controlled drug release, and synergistic therapy," *Nanoscale*, vol. 9, no. 4, pp. 1434–1442, 2017.

[182] A. M. Valencia and M. J. Caldas, "Single vacancy defect in graphene: Insights into its magnetic properties from theoretical modeling," *Physical Review B*, vol. 96, no. 12, p. 125431, 2017.

[183] S. Laurent, D. Forge, M. Port, A. Roch, C. Robic, L. Vander Elst, and R. N. Muller, "Magnetic iron oxide nanoparticles: Synthesis, stabilization, vectorization, physicochemical characterizations and biological applications," *Chemical Reviews*, vol. 108, no. 6, pp. 2064–2110, 2008.

[184] J. S. Choi, J. H. Lee, T. H. Shin, H. T. Song, E. Y. Kim, and J. Cheon, "Self-confirming "aND" logic nanoparticles for fault-free MRI," *Journal of the American Chemical Society*, vol. 132, no. 32, pp. 11 015–11 017, 2010.

[185] J. Wang, L. Zhang, F. Peng, X. Shi, and D. T. Leong, "Targeting Endothelial Cell Junctions with Negatively Charged Gold Nanoparticles," *Chemistry of Materials*, vol. 30, no. 11, pp. 3759–3767, 2018.

[186] K. E. O'Connell, A. M. Mikkola, A. M. Stepanek, A. Vernet, C. D. Hall, C. C. Sun, E. Yildirim, J. F. Staropoli, J. T. Lee, and D. E. Brown, "Practical murine hematopathology: A comparative review and implications for research," *Comparative Medicine*, vol. 65, no. 2, pp. 96–113, 2015.

[187] J. Wang, G. Zhou, C. Chen, H. Yu, T. Wang, Y. Ma, G. Jia, Y. Gao, B. Li, J. Sun, Y. Li, F. Jiao, Y. Zhao, and Z. Chai, "Acute toxicity and biodistribution of different sized titanium dioxide particles in mice after oral administration," *Toxicology Letters*, vol. 168, no. 2, pp. 176–185, 2007.

[188] R. Kuhlpeter, H. Dahnke, L. Matuszewski, T. Persigehl, A. von Wallbrunn, T. Allkemper, W. L. Heindel, T. Schaeffter, and C. Bremer, "R2 and R2* mapping for sensing cell-bound superparamagnetic nanoparticles: *in vitro* and murine *in vivo* testing," *Radiology*, vol. 245, no. 2, pp. 449–457, 2007, pMID: 17848680.

[189] Y. Y. Marchenko, B. P. Nikolaev, A. N. Shishkin, and L. Y. Yakovleva, "An NMR-relaxation study of the effect of albumin on aggregation of magnetic iron oxide nanoparticles," *Colloid Journal*, vol. 75, no. 2, pp. 185–190, 2013.

Appendix A

SUPPORTING INFORMATION TO CHAPTER 3

A.1 Practical Exploration of Bulk Magnetic Susceptibility Effects

A biophysical influence on T2 behavior arises from microscopic nanoparticle (NP) compartmentalization as NPs travel through the body and into cells. A number of studies have investigated the relationship between static dephasing regime theory and the transverse relaxation parameters T2 and T2*.[52,53] Theoretical and experimental work with cells has suggested that spatially confined superparamagnetic NPs (e.g., NPs clustered in vesicles) will display altered magnetic decay properties; at close proximity the NPs begin to act as a bulk magnetic material, rather than as discrete magnetic domains.[54] The end result of clustering increases the local field inhomogeneities generated by the NPs, with the T2* parameter especially affected. Through this phenomenon, the parameter T2′ (T2′ = T2* − T2) has been explored for its potential proportionality to the intracellular uptake of NPs.[188] Given our technique of interleaved QT2 and QT2* imaging, we were able to acquire T2* data over the full 4 h time course, and calculate R2′ (= 1/T2′) for various organ compartments (Figure A.1). It is prudent to consider that NP aggregation in vivo can be far different from that observed in cell culture. For instance, physical clustering of NPs in vivo can occur when NPs bind to extracellular matrix proteins in the interstitium, as well as albumin in the blood.[189] Furthermore, NP uptake within white or red blood cells will induce NP clustering, leading to partial volume artifacts from the enhanced T2* of blood that masquerade as uptake into cells of the target organ. Given that cellular experiments found a minimal impact of clustering on the T2 parameter,[52] and realizing the multiple factors confounding the in vivo interpretation of R2′, we primarily rely on QT2 trends to make qualitative assessments of NP trafficking, and inspect T2* and T2′ as supplementary points of interest.

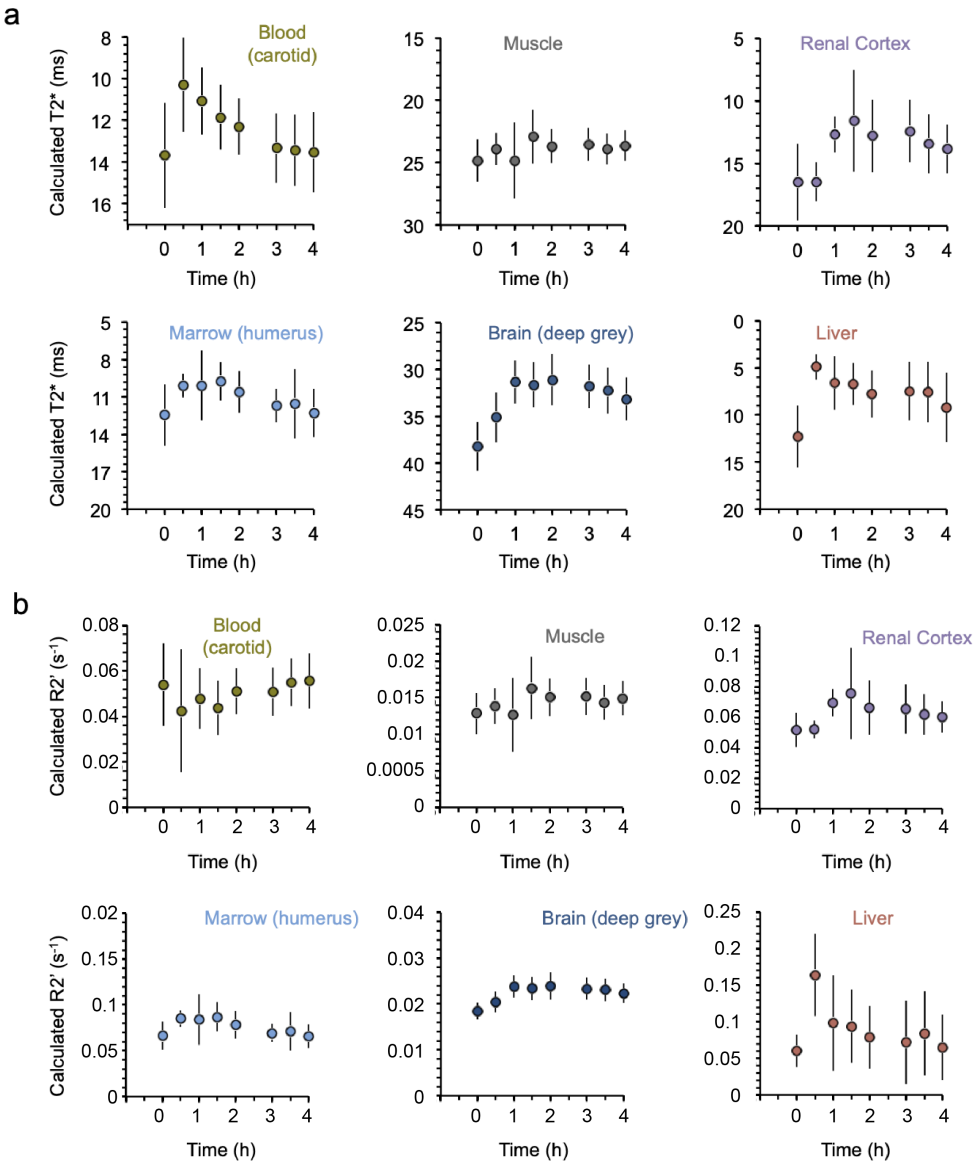

Figure A.1: T2*-W and R2′ values for macaque. (a) T2*-W values for one macaque versus time in various organs of interest. (b) Calculated R2′ versus time in one macaque where $R2' = R2^* - R2$, $R2^* = 1/T2^*$, and $R2 = 1/T2$.

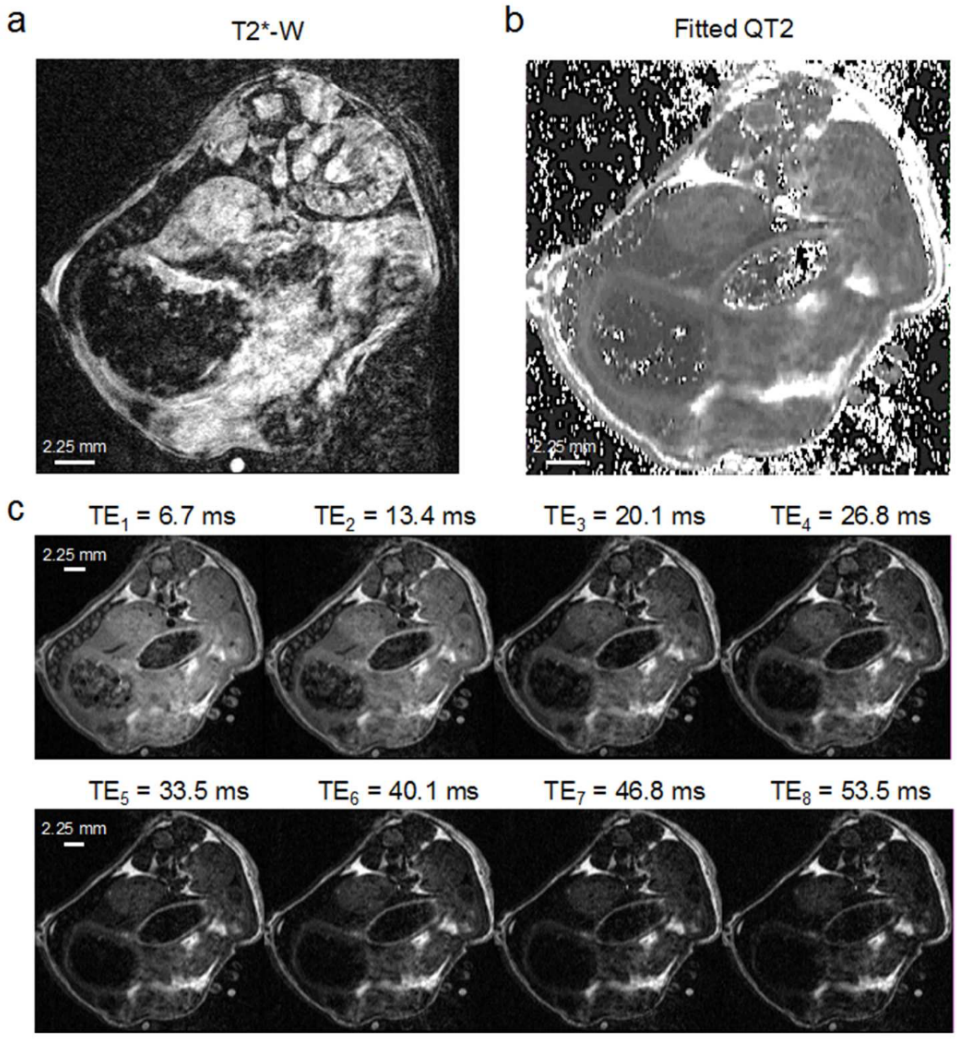

Figure A.2: Representative transverse raw MRI images of the mouse abdomen. (a) T2*-W image, and (b) QT2 map calculated by automated curve fitting. (c) Spin-echo images obtained during scanning and used to calculate QT2 maps. The first eight raw spin echo images are shown as an example, although 16 echoes were acquired during each scan.

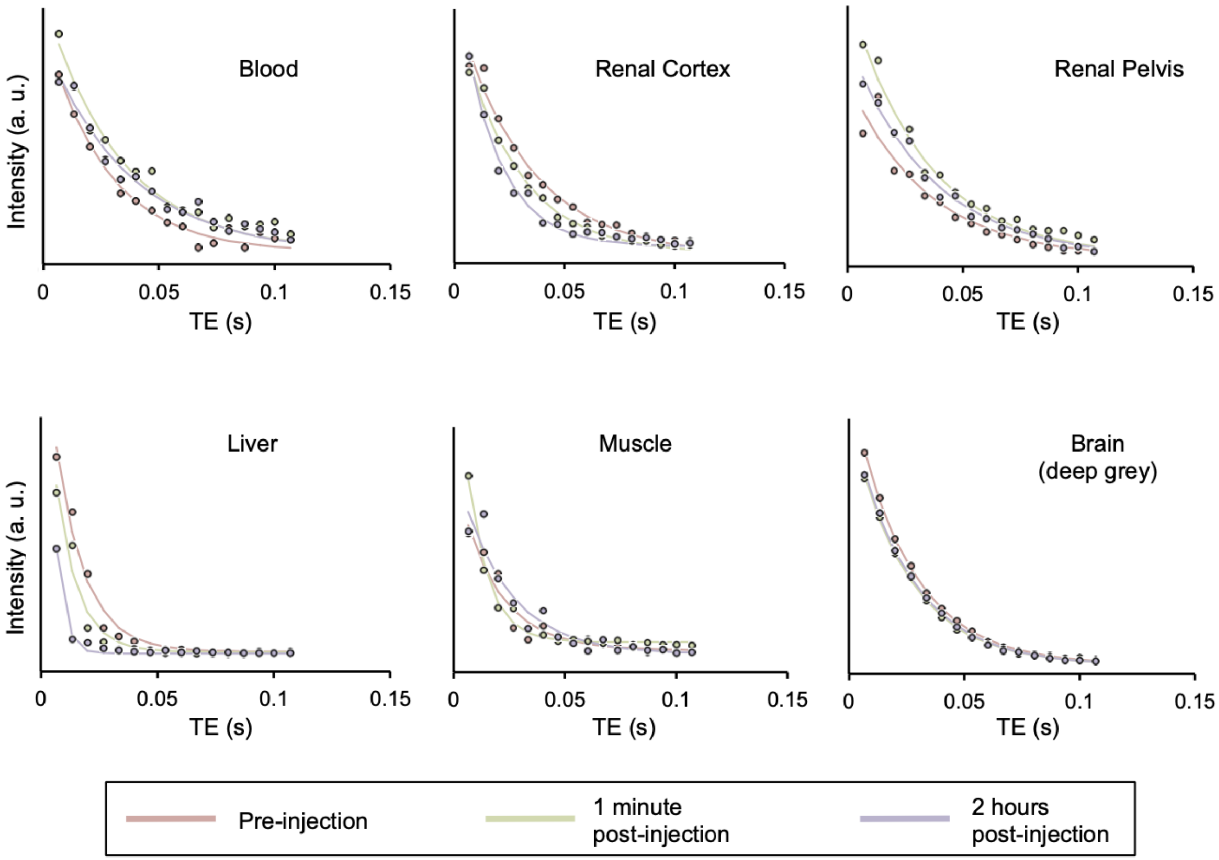

Figure A.3: Nonlinear least squares estimation of T2 decay profiles. T2 decay profiles in multiple organs pre- and post-NP injection. Anatomical ROI-averaged signal intensity over 16 sequential spin-echoes of an MSME sequence is used for nonlinear curve fitting and calculation of T2. Data points in red were obtained prior to NP injection, green data points were acquired 1 min after injection, and purple data points were acquired 2 h after injection. Trend lines demonstrate the accuracy of nonlinear least squares curve fitting, using the function $y = A\exp^{(-1/\mathrm{T2})t}$.

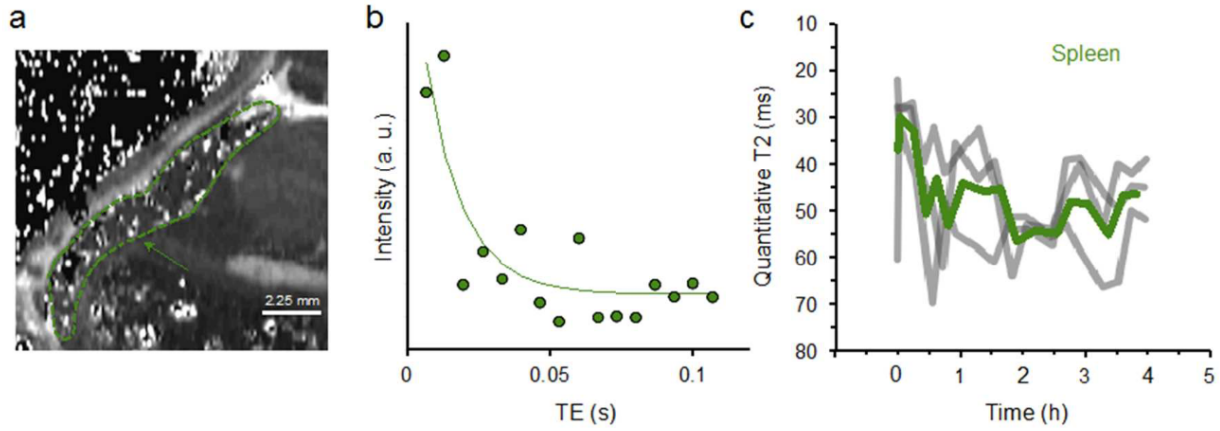

Figure A.4: High variability in splenic mouse QT2 data. (a) Fitted QT2 scan with a dashed green outline highlighting the splenic border. Numerous bright and dark voxels within the spleen represent areas of poor fit from estimating T2 by linearizing the exponential decay data and using ordinary least squares estimation. (b) Representative T2 decay curve from the spleen, with T2-W signal plotted over 16 sequential spin-echoes. Raw data contains a high degree of noise, contributing to error in exponential curve fits. (c) Individual QT2 time courses in the spleens of three mice are shown in gray with the average signal superimposed in green. The variation between sequential calculated values over time is substantially greater than that seen in all other organ compartments.

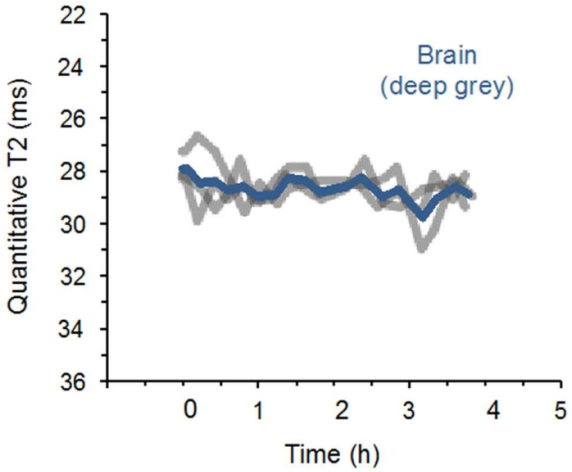

Figure A.5: Calculated T2 values over time in the mouse brain. QT2 traces from the brains of individual mice are shown in gray, while the average is displayed in blue.

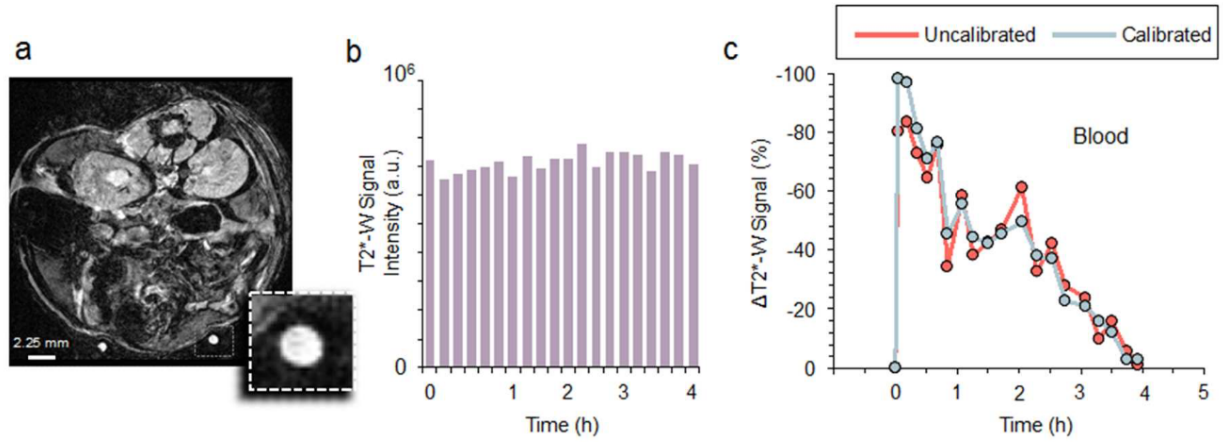

Figure A.6: Water phantom calibration for T2*-W data. (a) Representative T2*-W image of the mouse abdomen is shown, highlighting the location of dual water tube phantoms used for signal calibration. (b) T2*-W signal intensity averaged over the two water tubes, from each sequential scan during a 4 h time course. Fluctuations in T2*-W signal within the water phantom are assumed proportional to fluctuations over the entire image and occur due to differences in automated gain settings, pulse power, and sensitivity changes in scanner hardware over time. (c) Examples of the change in T2*-W time course provided by water phantom correction. ROI-averaged T2*-W signal in the external jugular vein prior to correction (red curve) and after correction (blue curve). Since the signal in the water tubes is relatively stable throughout the imaging time course, the change between the uncalibrated and calibrated trends is not dramatic; however, the uncalibrated signal does make larger departures from a linear fit than the calibrated plot indicating a reduction in noise after calibration to the water signal.

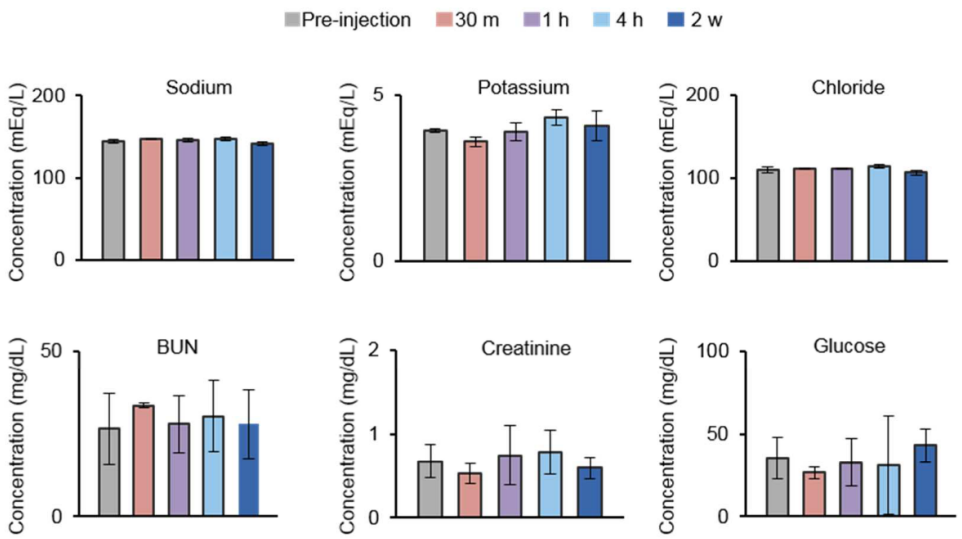

Figure A.7: Macaque laboratory blood chemistry values before and after IOSPM NP injection. Electrolyte balance was maintained after IOSPM NP injection and normal levels of creatine (Cr) and blood urea nitrogen (BUN)/Cr ratios were observed, indicating normal kidney function. Averages and standard deviation were determined from values from four macaques.

Table A.1: Average number of MRI voxels and average area included within anatomical ROIs for the macaque and mouse

	Macaque		Mouse	
	Voxels (#)	Area (mm^2)	Voxels (#)	Area (mm^2)
Blood	34	30	15	0.3
Muscle	227	200	105	2.0
Renal cortex	170	150	98	1.9
Renal pelvis	49	43	40	0.8
Spleen	193	170	82	1.6
Marrow	41	36	58	1.1
Brain	136	120	160	3.0
Liver	170	150	340	6.4

Appendix B

SUPPORTING INFORMATION TO CHAPTER 6

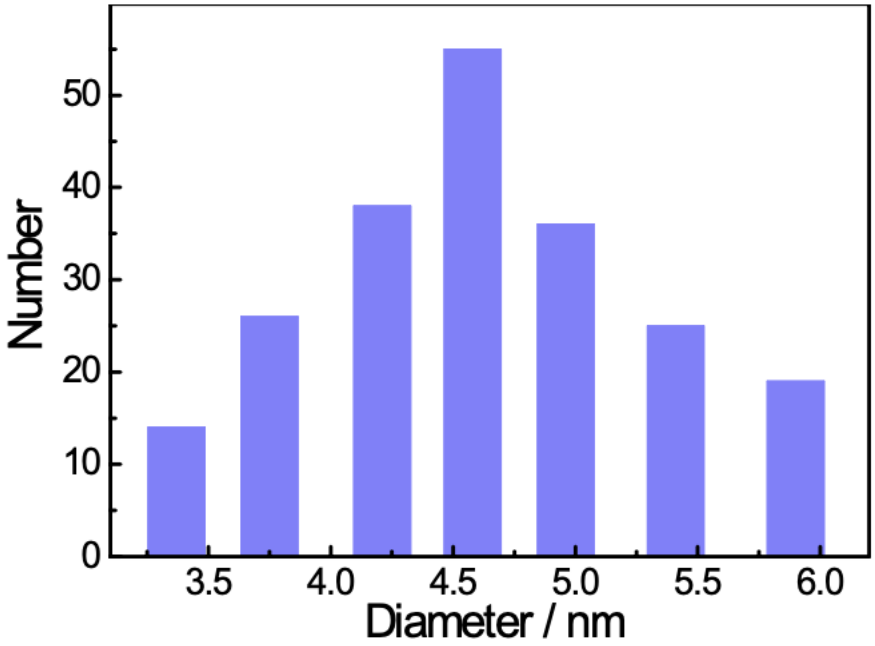

Figure B.1: Size distribution of SL-BGQDs. Histogram of measured diameters of approximately 200 SL-BGQDs determined from TEM images.

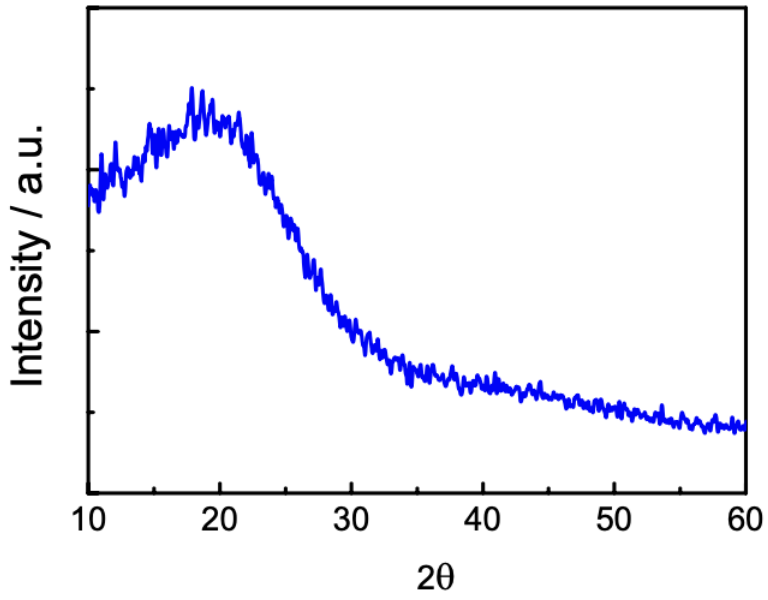

Figure B.2: X-ray diffraction pattern of SL-BGQDs.

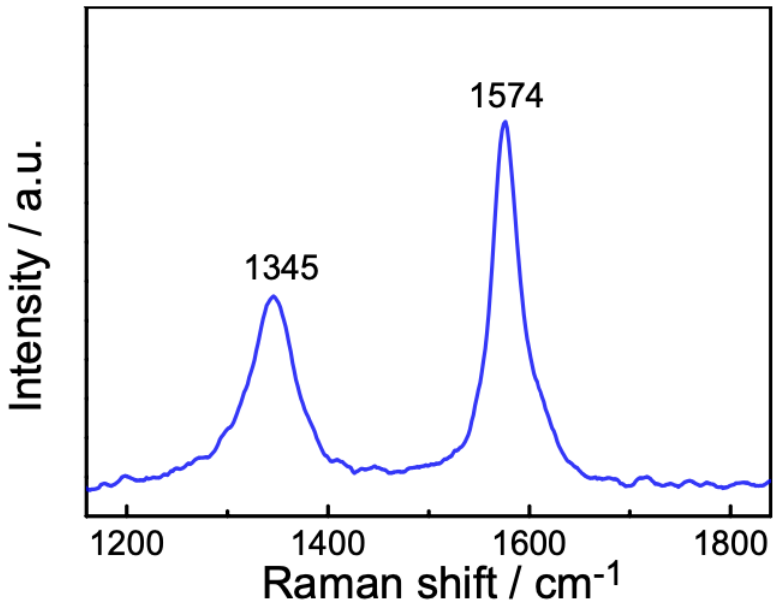

Figure B.3: Raman spectrum of SL-BGQDs.

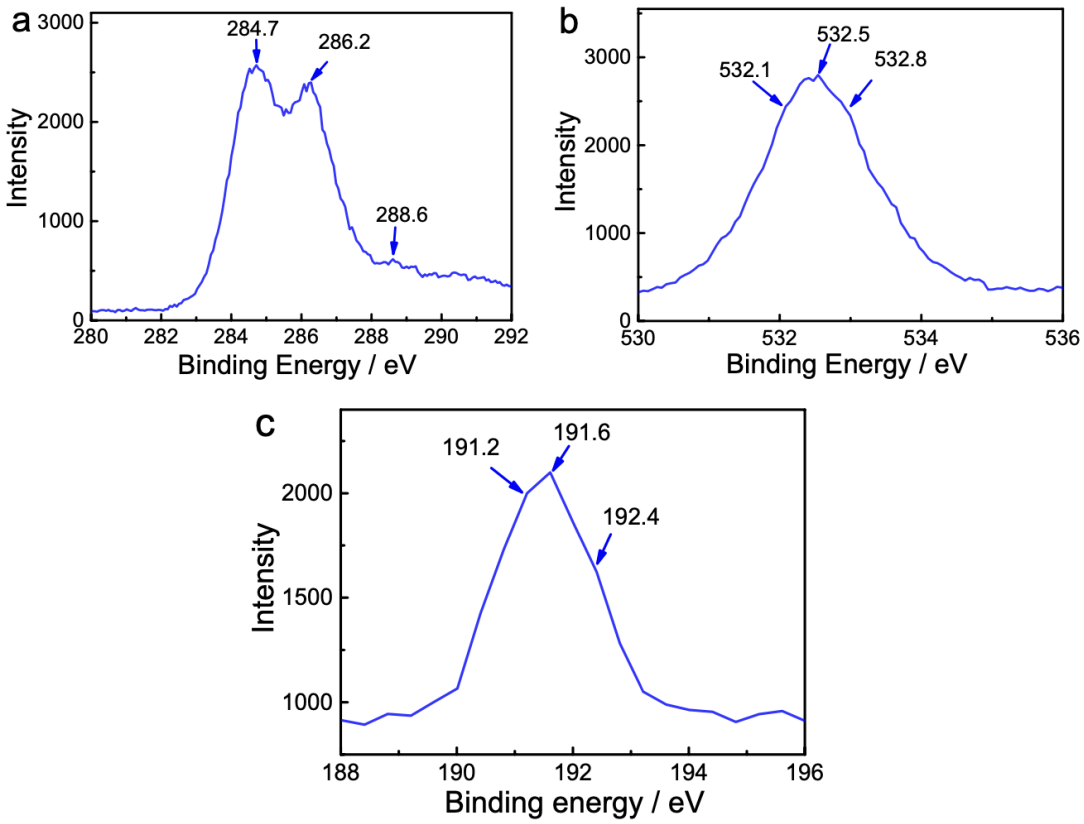

Figure B.4: Surface properties of SL-BGQDs determined by XPS. (a) C 1s, (b) O 1s, and (c) B 1s spectra. The C 1s peaks at 284.7, 286.2, and 288.6 eV are assigned to carbon in forms of C−C (sp^3)/C=C (sp^2), C−O (sp^3), and O−C=O (sp^2), respectively.[173] The O 1s peaks at 532.1, 532.5, and 532.8 eV are associated with C=O quinone-type groups, C−OH phenol groups, and C−O−C ether groups, respectively.[174] The B 1s peaks at 191.2 and 191.6 eV are attributed to sp^2 C=B bonds.[175,176] In addition, the B 1s peak at 192.4 eV is associated with B−O bonds.[177] The peaks at 191.2 and 191.6 eV provide evidence of boron doping in SL-BGQDs.

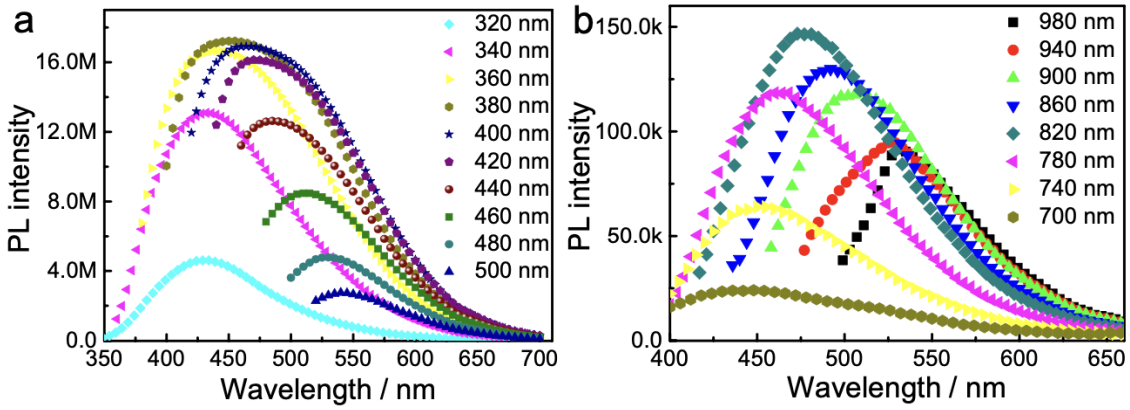

Figure B.5: Photoluminescent properties of SL-BGQDs. (a) PL spectra and (b) upconverted PL spectra of SL-BGQDs under different excitation wavelengths from 320 nm to 980 nm.

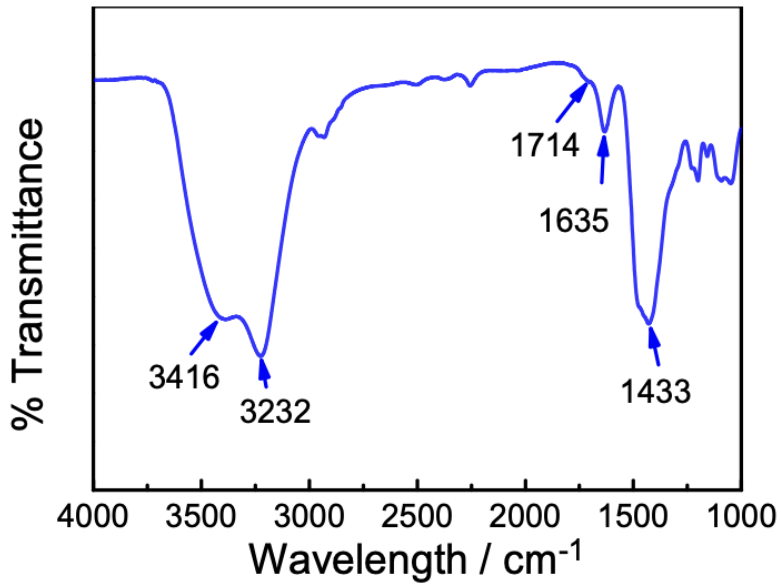

Figure B.6: FTIR spectrum of SL-BGQDs. Absorption peaks of the O−H stretching mode at 3416 cm^{-1} and 3232 cm^{-1} and the C=O stretching mode at 1714 cm^{-1} correspond to carboxylic acid groups conjugated with condensed aromatic carbons. A weak peak at 1383 cm^{-1} is attributed to the C−O vibration of a carboxylic acid group, and the C=C vibration of sp^2-hybridized carbon atoms was detected at 1600 cm^{-1}.

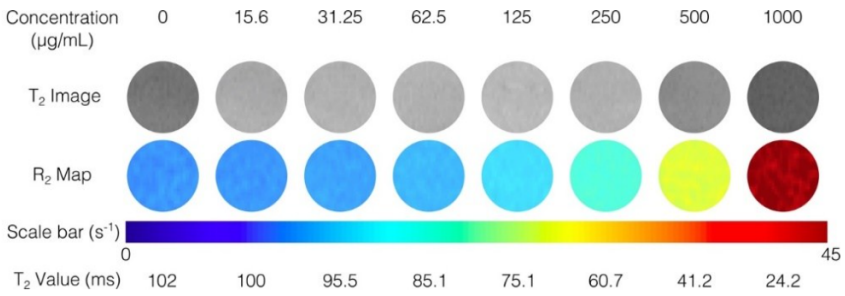

Figure B.7: T2-weighted MR images and R2 maps of SL-BGQDs at different concentrations.

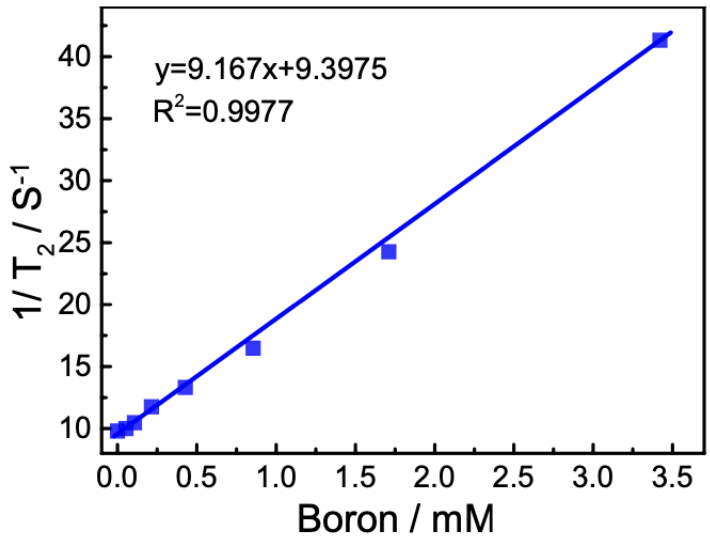

Figure B.8: Plot of $1/r2$ as a function of the boron concentration in SL-BGQDs. The slope of the curve is defined as the transverse relaxivity, r_2 ($= 9.2\ \mathrm{mM}^{-1}\ \mathrm{s}^{-1}$).

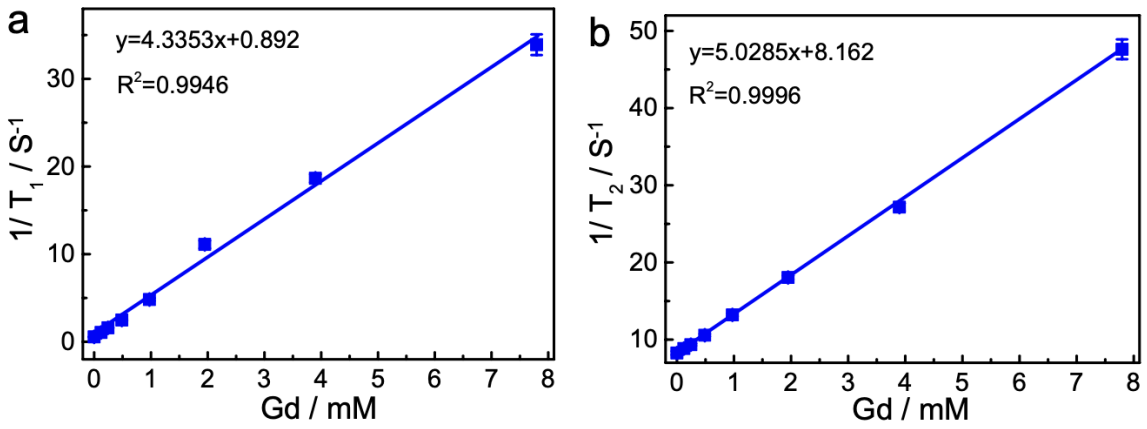

Figure B.9: Relaxivity values of Gd-DTPA measured at a magnetic field strength of 14 T. Plot of (a) $^1/_{T1}$ and (b) $^1/_{T2}$ as a function of Gd-DTPA concentration. The slopes of the plots in (a) and (b) are defined as the longitudinal relaxivity, r_1 ($= 4.3$ mM^{-1} s^{-1}), and the transverse relaxivity, r_2 ($= 5.03$ mM^{-1} s^{-1}), respectively.

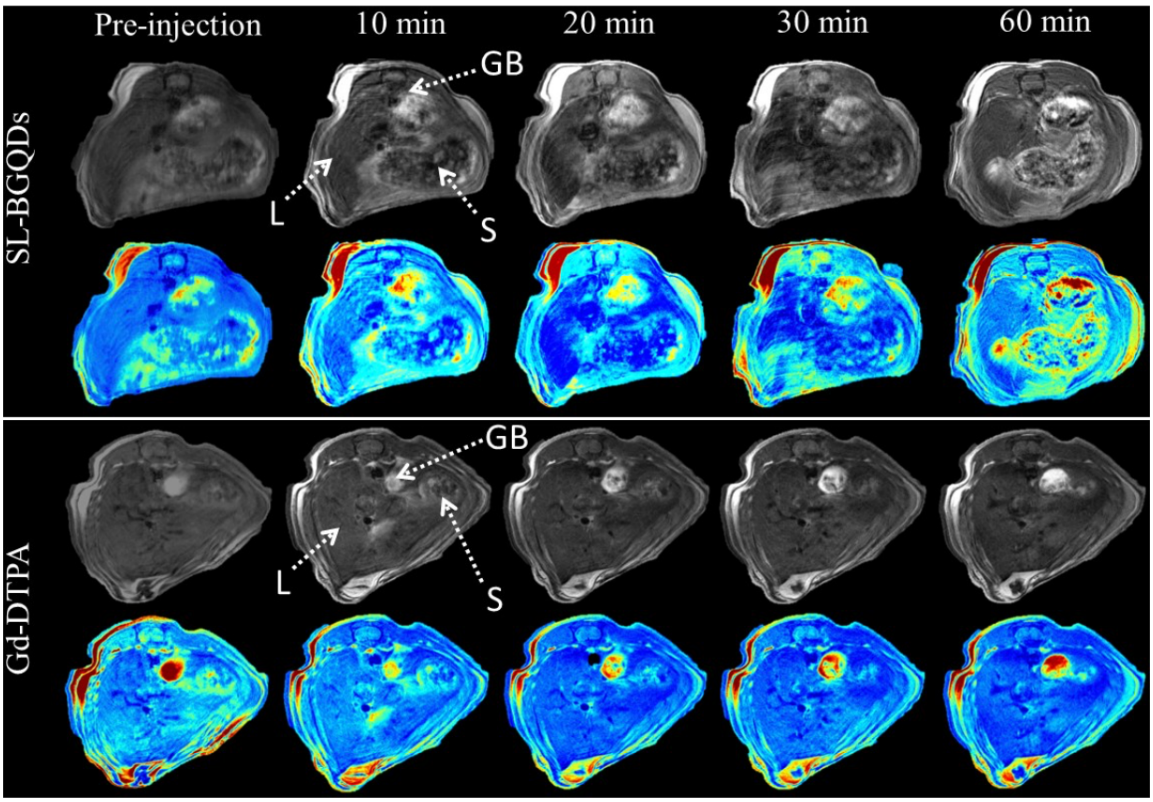

Figure B.10: In vivo abdominal MR imaging. T1-weighted MR images of the cross-sections of mice receiving SL-BGQDs (top panel) and Gd-DTPA (bottom panel) treatments with dynamic time-resolved MR imaging acquired before and at various time points after intravenous contrast agent administration. Both grayscale and colorized images are displayed for each experimental group. The arrows denote various organs: liver (L), stomach (S), and gall bladder (GB).

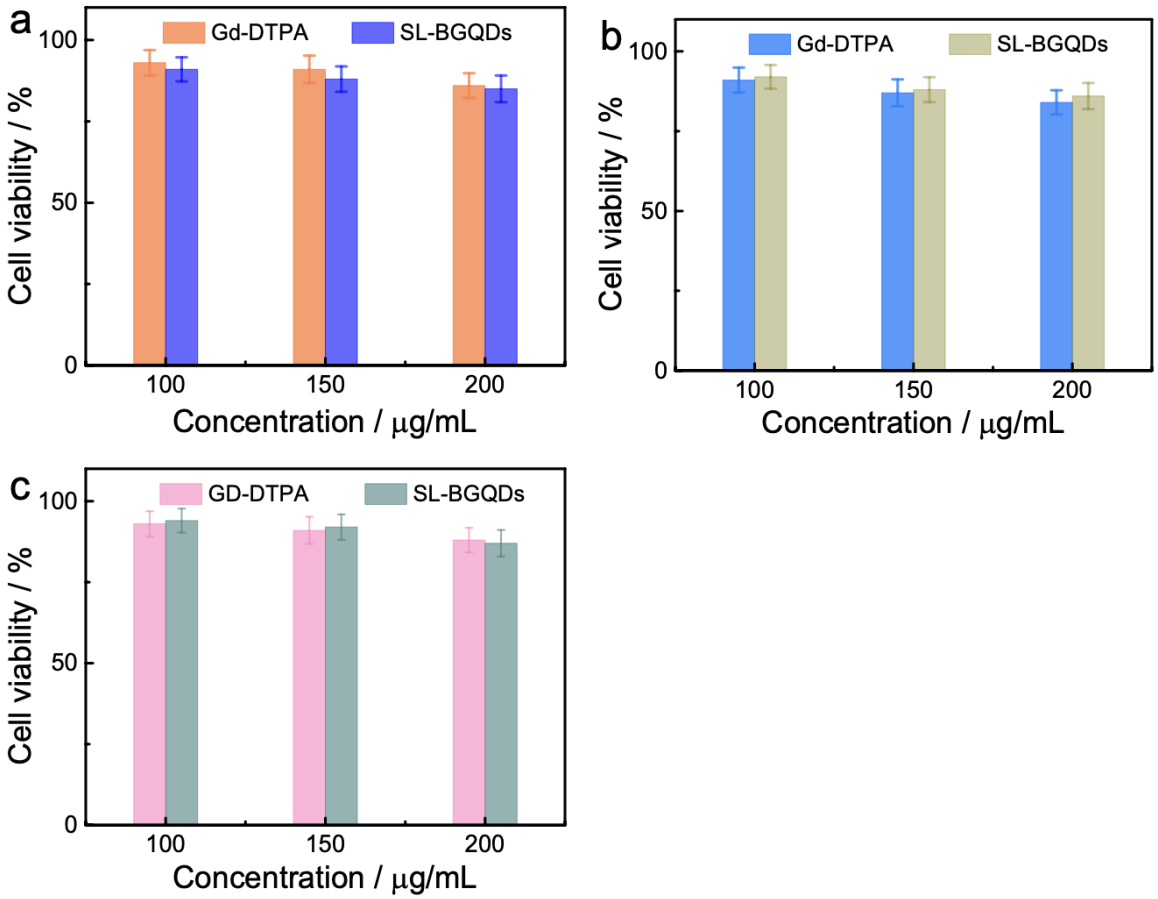

Figure B.11: In vitro cytotoxicity of SL-BGQDs and Gd-DTPA. Cell viability of (a) 4T1, (b) SF763, and (c) B16F10 cells 72 h after treatment with SL-BGQDs or Gd-DTPA.

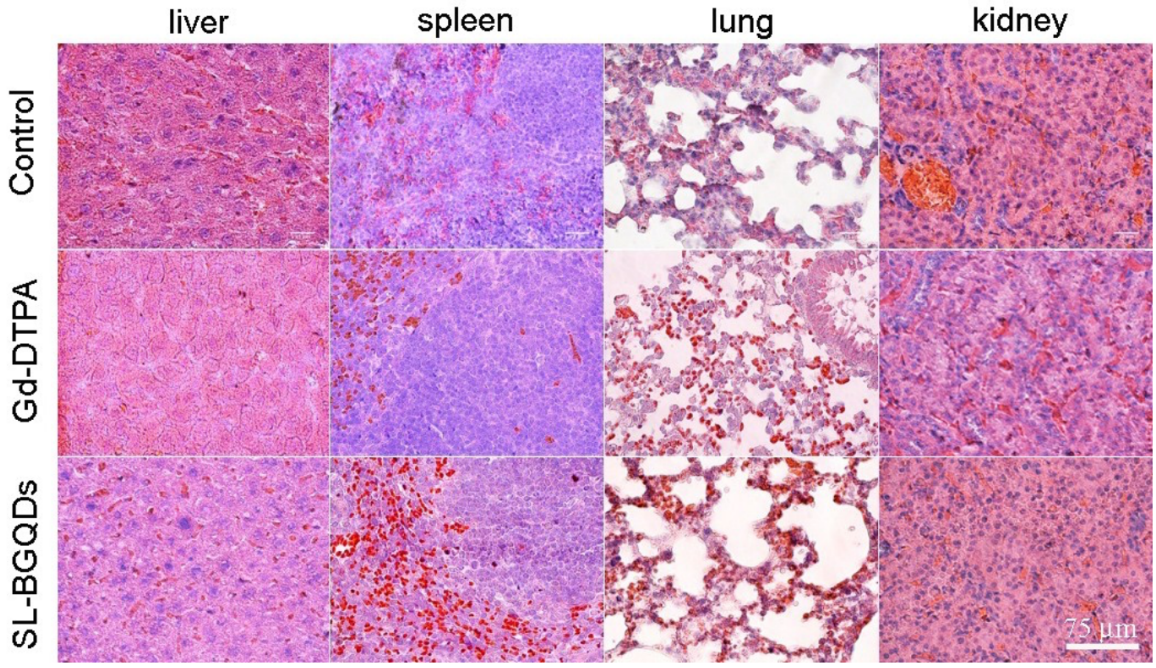

Figure B.12: Tissue toxicity of SL-BGQDs and Gd-DTPA. H&E staining of various organs harvested from PBS- (control), Gd-DTPA-, and SL-BGQD-treated mice. The scale bar is 75 μm.

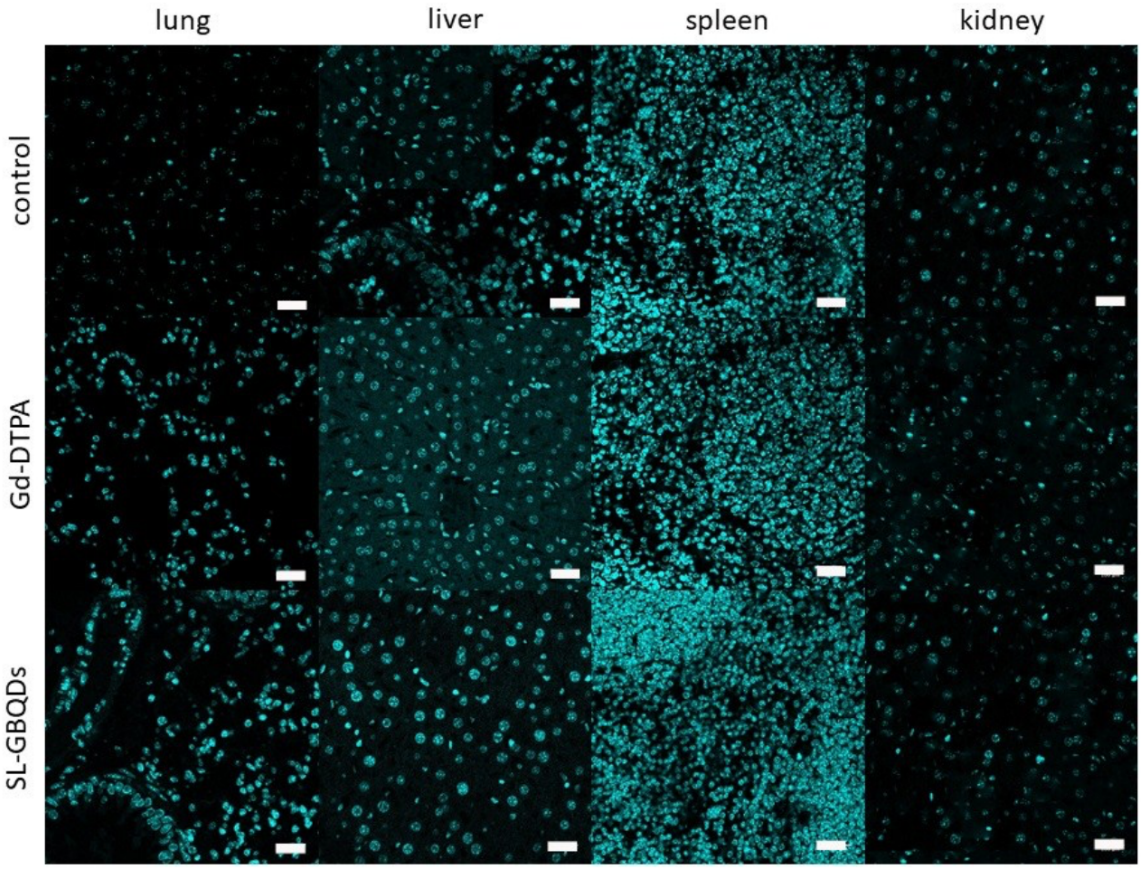

Figure B.13: Cell nuclear morphology of tissues treated with SL-BGQDs. DAPI staining of various organ tissues obtained from mice treated with Gd-DTPA, SL-BGQDs, or PBS (control). The scale bars represent 100 µm.